# Observations of magnetically driven events in astronomical systems.

Thesis

How to cite:

Eves, Benjamin Alistair Curtis (2006). Observations of magnetically driven events in astronomical systems. PhD thesis The Open University.

UNRESTRICTED

Faculty of Science, The Open University

# Observations of Magnetically Driven Events in Astronomical Systems

Benjamin Alistair Curtis Eves M.Phys.

Submitted for the degree of Doctor of Philosophy

10th June 2005

DATE OF SUBMISSION: 10 JUNE 2005
DATE OF AWARD: 19 SEPTEMBER 200

To my Dad, you where there for the start of this journey but you never got to see me finish. This is for you .....

# CONTENTS

# LIST OF FIGURES

# LIST OF TABLES

# Abstract

The interaction of magnetic fields with astrophysical plasmas drives many impressive displays of particle acceleration and impulsive energy release. Within the following work we present a brief overview of magnetic reconnection and energy release mechanisms. We then explore these impulsive energy releases in the form of solar flares (Chapter 2), flaring in the X-ray and optical on other stellar types (Chapter 4), and finally we explore the nature of what could be the brightest microquasar known. The RHESSI spectroscopy of flares in the hard X-ray regime confirms the presence of a deviation from the power law nature of the non-thermal flare spectra. These "knees" allow us to test our current knowledge of particle interactions during a flare. The results of this show that the high resolution spectra do not produce an unphysical result in the underlying accelerated electron spectrum. This gives us greater confindence in our current theoretical understanding of energetic particle interaction. Our observations in both the X-ray (Section 4.1) and the optical (Section 4.2) reveal, as expected, that the flare stars observed were mid M-dwarf stars and cool red dwarfs. Finally we come to the case of 1RXS J 162848.1-415241, possibly the brightest microquasar known to date. As it turns out it is probably not a microquasar at all but more likely is another example of magnetic field interaction, a many spotted RS CVn System. Overall we see magnetically driven events producing some of the most violent energy outburst in the galaxy, and have taken a few steps forward towards a better understanding of the underlying nature of both the events themselves and the objects on which they play out.

# Acknowledgements

The author wishes to thank Carole Haswell for stepping into the breach in my second year and leading me, sometimes forcibly, to the heady heights of a PhD. She was an inspiration and her combination of encouragement, understanding and humour made this a truly enjoyable experience. Thanks also to Andy Norton, who got me over the final hurdle and has been a constant throughout this whole process. Andrew Conway, my original PhD Daddy, who started this whole process with me, he always had time to talk and his enthusiasm for WWII Russian planes was a joyous sight to behold.

My examiners deserve a special mention as without Professors Jones and Collier Cameron this thesis would be, as they put it:

"Like a detective novel were someone has ripped out the last page."

Hopefully now the true nature of the suspects have been revealed.

All of my OU family aided the creation of this beast. My office mates, in order of longest time served, Stephen Justham his dedication to his work was only matched by his excitement at the bizarre. John Barker, you would often find his robots crawling, rolling and axing their way around the office. He also paved the way for moving back to Lancashire and becoming a teacher. Craig Powell the purveyor of coffee and dreams whos inexhaustible IDL knowledge was sorely missed. Stelios Tsangarides, my Cypriot friend, who always provided an excuse for a break but the ideas generated during them always lead to insights in the office. The Girls, who let me invade their office to finish off and sometimes came in to find their desks covered in papers and their computers locked.

All the folk at Coffee Club over the years who kept me sane even if I didn't return the favour. Robin Barnard, the lovable giant with an almost inexhaustible supply of SAS and XMM tips. Geoff Bradshaw, he can fix anything and quite often had to.

He kept things running and always providing last minute panic relief. Lisa Blake for taking me under her wing. Dave ‘this is the fist and this is the fury’ Lott for being a friend and letting me share in his joy. Maria for giving me a place to stay and an open ear. Last but by no means least Chris Brockwell, my Big PhD Brother, for teaching me the art of respecting other peoples privacy and for giving me someone with which to share my Ray Mears obsession.

Thanks to my Mum, Dad, sister Kat, Hal, and Biscuit for all there years of love and support without them this would never have been attempted.

Finally, Lisa, your love has got me through this.

# Chapter 1

# Introduction

Magnetic fields are present at some level in most astronomical objects and on a variety of scales, from planetary magnetospheres to active galactic nuclei. The interaction of these magnetic fields with the surrounding environment can give rise to impressive displays of particle acceleration and impulsive energy release. The main drive of this thesis is to analyse the signatures of magnetic activity, in a number of stellar systems. We shall start with our closest stellar neighbour, the Sun, possibly the best laboratory for the study of magnetically driven events. We shall then proceed to other systems that display flare-like events, the flare stars and microquasars. Before we look at the events themselves, it is necessary to understand the current thinking on how magnetic fields interact with the surrounding plasma in the system to produce such impulsive and energetic displays.

## 1.1 Flare Mechanism

It is widely accepted that the energy released in a flaring event originates from a relaxation of a stressed magnetic field configuration. In order to go from this stressed configuration to a lower energy configuration magnetic reconnection must occur. Figure 1.1 illustrates this process based on the model first demonstrated by Petschek (1964). The first step is getting the magnetic field lines to diffuse through the plasma. Starting from Ohms law for an idealised plasma,

$$\frac{\delta \underline{B}}{\delta t} = \nabla \times (\underline{v} \times \underline{B} + \eta \nabla^2 \underline{B}) \tag{1.1}$$

where $\underline{B}$ is the magnetic field, $\underline{v}$ the velocity and $\eta$ is the magnetic diffusivity, the first term on the right of equation 1.1 is representative of the advection of the field lines, moving with the plasma, and the second term represents the diffusion of the field lines through the plasma. The ratio of these two terms, advection/diffusion, gives us the magnetic Reynolds number $R_{mag}$ expressed more simply as

$$R_{mag} \approx \frac{vL}{\eta} \tag{1.2}$$

$v$ is a velocity term and $L$ is a length scale. For an astrophysical plasma $L$ is large and $\eta$ is small in the low resistivity plasma, and so the advection term dominates. This means then that the magnetic field lines are "frozen-in" to the plasma. The only way to get the field lines to diffuse and therefore reconnect is to decrease the length scale. This is achieved by having two sets of oppositely directed fields in close proximity thus $R_{mag}$ decreases and the diffusion term becomes dominant.

As indicated in Figure 1.1(b) at the reconnection site a current sheet is formed that accelerates the particles in the plasma. These very high energy particles, hundreds of keV for electrons in a solar flare, are accelerated through the plasma and so give up their energy through Coulomb collisions or through bremsstrahlung radiation. The bremsstrahlung radiation arises from the perturbation of the fast moving particle by an oppositely charged particle in its vicinity, the resulting bremsstrahlung photon spectrum can be derived quite simply as follows.

Figure 1.1: Idealised view of two-dimensional magnetic reconnection.

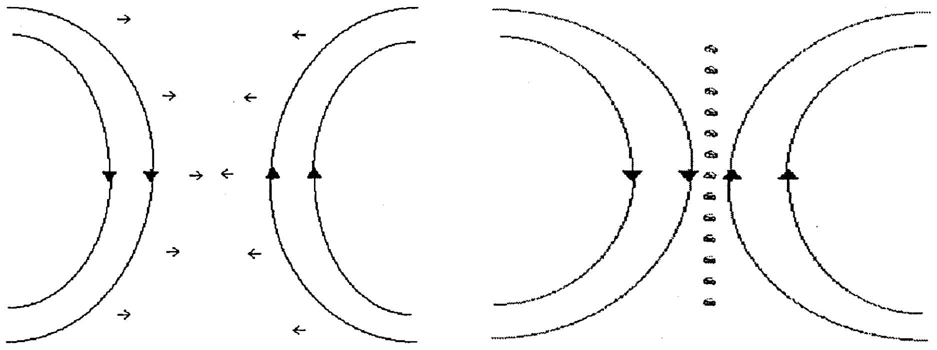

(a) Magnetic fields of opposite sense diffuse toward each other, or become twisted together.

(b) As they near each other, in accordance with Lenz's law, a current sheet is formed parallel to the field lines, but directed perpendicular to them (into the page in the diagram), and the electrons in this region are accelerated. Current is into the paper.

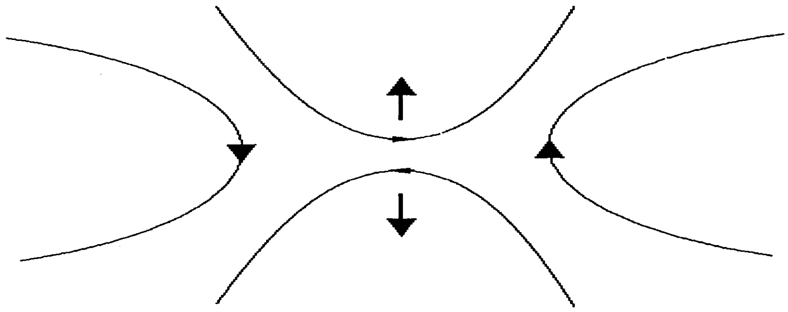

(c) The magnetic fields come together and reconnect to the new geometry shown. The solid arrows show the direction of motion of the newly formed field lines as the tension in the magnetic field is released. This is an attempt to form a lower energy configuration.

### 1.1.1 Non-thermal Bremsstrahlung

If we have a non-thermal electron energy distribution, f(E), defined as:

$$f(E) = f_o E^{-\alpha} \tag{1.3}$$

and we know that the number of photons $J_1(\epsilon)$ emitted per unit time, per unit energy, $\epsilon$, per unit volume, by one electron of energy E, is given by:

$$J_1(\epsilon) = \sigma(E,\epsilon)nV(E) \tag{1.4}$$

where $\sigma(E,\epsilon)$ is the intersaction cross-section for electron of energy E, n is the number density of ions in the region, and V(E) is the velocity of the electron then we can obtain the hard X-ray spectrum as follows. Take the interaction cross-section to be of Kramer‘s form,

$$\sigma(E,\epsilon) = \frac{\sigma_o}{E\epsilon} \tag{1.5}$$

for $E > \epsilon$ and 0 if $E < \epsilon$ and assume the kinetic energy of the electron is constant, i.e. the energy lost to the photons is negligible, then

$$E = \frac{1}{2}m_e V^2$$

Therefore

$$V(E) = \sqrt{\frac{2E}{m_e}} \tag{1.6}$$

So for a single electron of energy E, substitute equations 1.5 and 1.6 into equation 1.4:

$$J_1(\epsilon) = \frac{\sigma_o}{E\epsilon}n\sqrt{\frac{2E}{m_e}} \tag{1.7}$$

For a distribution of electrons in the range $E$ to $E + dE$ multiply f(E)dE (equation 1.3) into equation 1.7, to give:

$$J_1(\epsilon)dE = \frac{\sigma_o}{E\epsilon}n\sqrt{\frac{2E}{m_e}}f(E)dE \tag{1.8}$$

Integrating this equation between $\epsilon$ and $\infty$, we obtain the following equation for $\alpha > \frac{1}{2}$:

$$\int_\epsilon^\infty J_1(\epsilon)dE = J(\epsilon) = \sigma_o n\sqrt{\frac{2}{m_e}}f_o\frac{1}{(\alpha-\frac{1}{2})}\epsilon^{-(\alpha+\frac{1}{2})} \tag{1.9}$$

Therefore the non-thermal hard X-ray spectrum follows a power law.

$$J(\epsilon) = J_o\epsilon^{-\gamma} \tag{1.10}$$

Where

$$J_o = \sigma_o n \sqrt{\frac{2}{m_e}} f_o \frac{1}{(\alpha - \frac{1}{2})} \tag{1.11}$$

$$\gamma = \alpha + \frac{1}{2} \tag{1.12}$$

This was for the simplified case using Kramer's Cross section.

Not making this approximation, we solve for both thick and thin targets to get the following results:

$$\gamma = \alpha + 1 \quad \text{(thin target)} \tag{1.13}$$

$$\gamma = \alpha - 1 \quad \text{(thick target)} \tag{1.14}$$

The thin target means that the injected electrons are not thermalized, whilst the thick target means the injected electrons are completely thermalized, due to Coulomb collisions with the ambient electrons. For instance, the thin regime is appropriate for travelling in corona and transition region, and the thick regime is appropriate when injected electrons hit the chromo/photospheres.

### 1.1.2 Thermal Bremsstrahlung

For the thermal case we have a similar derivation but use a Maxwellian distribution of electron energies of the form:

$$f(E) = \frac{1}{Ae^{-\frac{E}{kT}}} \quad \text{(electrons)} \tag{1.15}$$

This gives the simplified result (Cranell et al. 1978), for the produced photon spectrum of:

$$J(E) = 1.3 \times 10^3 \frac{n_e^2 V e^{-\frac{E}{T}}}{E^{1.4} T^{0.1}} \quad \text{(photons)} \tag{1.16}$$

showing that the thermal bremsstrahlung spectrum is dominated by the exponential term and so is exponential in nature. We shall see this is clearly the case in Section 2.3.1

## 1.2 Flaring on The Sun

Due to its proximity to us the Sun is the brightest X-ray source in the sky, and since it is so close it provides the ideal opportunity to study magnetically driven events in a stellar environment at unprecedented temporal and spatial resolution. Since the first solar flare was observed by Carrington (1859) in the optical most data on these events was obtained photographically using narrow wavelengths predominately of hydrogen lines, in particular H$\alpha$ and some helium lines. With the advent of space borne X-ray telescopes we began to form a fuller picture of these impulsive and highly energetic events.

Flares on the Sun are always associated with sunspots, regions of emerging magnetic flux, which themselves are the footprints of active region loops containing trapped coronal plasma, confined by the field loop structure. The trigger event for a flare is believed to be reconnection of the field lines above top of the loop structure. Until fairly recently evidence for this reconnection event had never been observed. Not until *YOHKOH* did observational evidence emerge of a loop top source of hard X-rays. Masuda et al 1994 presented *YOHKOH* `HXT` observations of a clear hard X-ray loop-top source, associated with a soft X-ray extended loop and two hard X-ray footpoints at the base of the loop structure. The reconnection site is higher in the corona than the loop top source. From the reconnection site the accelerated particles ( in the case of electrons they can be accelerated up to hundreds of keVs) impact in to the denser plasma at the top of the loop producing a hard X-ray bright point. These then stream down the loop in both directions before giving up the remainder of their energy as they slam into the denser plasma of the chromosphere, producing the hard X-ray footpoints seen.

The flaring event itself comes in three distinct phases as shown in Figure 1.2

- The Preflare stage (P.F. on Figure 1.2), in which we see a gradual increase in the

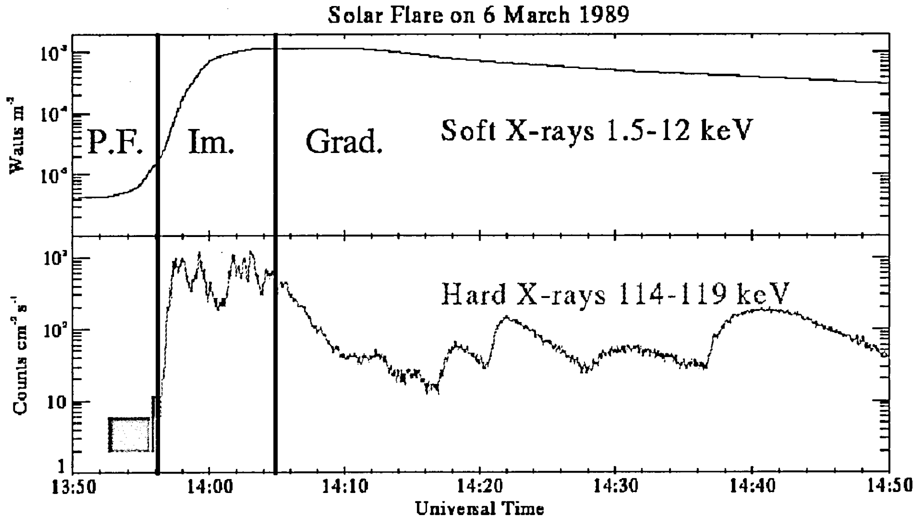

Figure 1.2: Soft and hard X-ray, and gamma ray spectra of the 6th March 1989 flare. The Preflare (P.F.), Impulsive (Im.) and Gradual (Grad.) phases of the flare are indicated. Taken from http://hesperia.gsfc.nasa.gov/hessi/images/diagrams.gif

soft X-ray but little or no hard X-ray emission.

- The Impulsive Phase (Im. on Figure 1.2), where the hard X-ray emission rises impulsively, often in short intense spikes lasting a few to tens of seconds, and the soft X-ray emission continues to rise but more rapidly.

- The Gradual phase (Grad. on Figure 1.2), the hard X-ray emission starts to decay exponentially on a time scale of minutes, the soft X-ray flux continues to rise to a peak and then exponentially decays but over a longer time, possibly several hours.

### 1.2.1 X-ray Spectrum of a Flare

The X-ray spectrum of a flare is a very powerful tool for understanding the particle acceleration and transport properties during a flaring event. As seen in Section 1.1 the photon spectrum is an integral of the electron spectrum, multiplied by the cross-section for the bremsstrahlung collisions. Brown (1971) first recognised that there was an analytical way to invert the spectrum, i.e. go from photon spectrum to electron spectrum. This means that starting from a given photon spectrum, we can recreate the injected electron spectrum and hence obtain details about the initial population of the injected electrons. Early hard X-ray spectra of flares indicated that the hard X-ray spectrum was dominated by a power-law drop off with some evidence for a break to a steeper power law above 60-100keV (Kane and Anderson 1970) although some still believed the best interpretation was that of a purely thermal component to the spectra. Not until Lin and Schwartz (1987) did the true nature of the spectrum become apparent. They observed a flaring event on the 27th of June 1980 using a balloon based array of germanium detectors, and could clearly demonstrate that the spectrum above 30keV showed a double power law with a break energy around 25-40keV, see Figure 1.3

It was also noted by the authors that the break is a narrow feature. The narrowness of the feature is vital to our understanding of the nature of the electron population in the flare. Since the photon spectrum is an integral of the electron spectrum any feature in the electron spectrum is smoothed out in the associated photon spectrum. This means that a narrow feature in the spectrum indicates a dramatic feature in the underlying electron spectrum. In order to get a broken power law in the photon spectrum the electron energy distribution must also follow two power laws of different indices above and below the energy of the break. The structure around the break in the electron spectrum could be far more complicated than a sudden change in index, but any complexity is smoothed out in the photon spectrum, resulting in a sharp 'knee' at the break energy. Following from the results in section 1.1.1 the indices of the electron spectrum above and below the knee in, for example, the thin target regime would be softer (one less) than those observed in the photon spectrum, and harder in the thick target regime. The shape of the electron spectrum is a clue to the acceleration mechanism in the flare and also a test bed for our

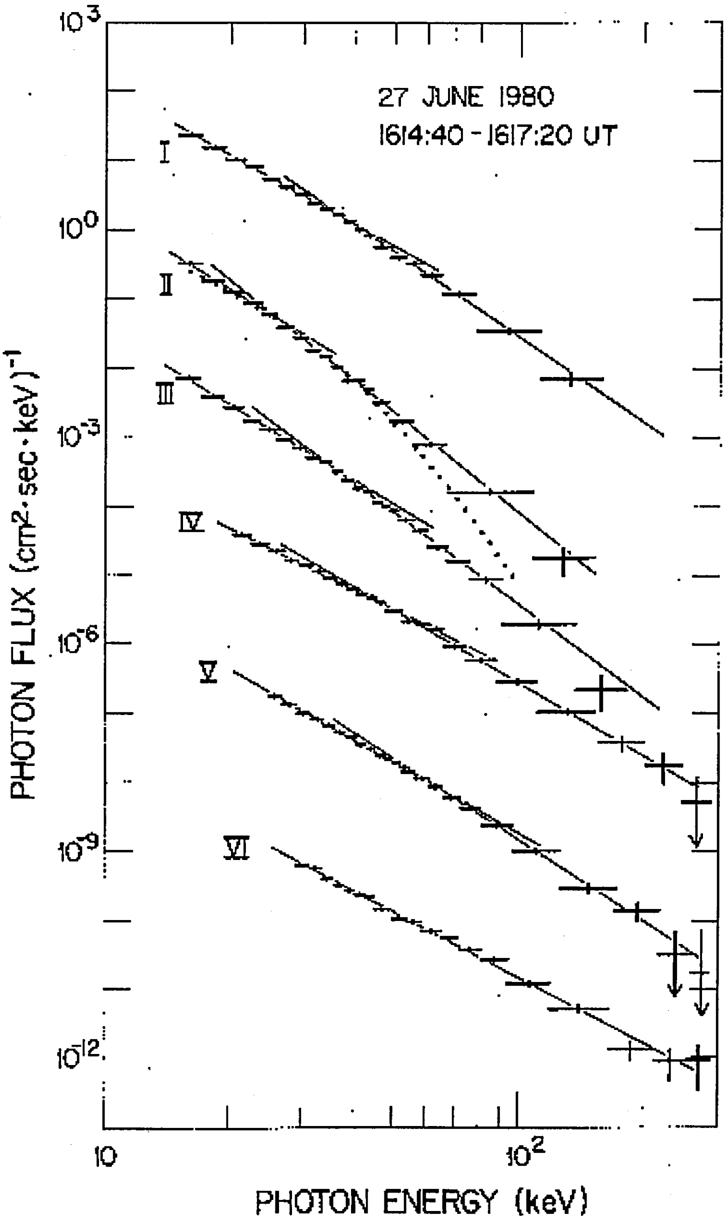

Figure 1.3: The hard X-ray spectra of the 27th June 1980 flare (Lin and Schwartz (1987)) showing the best fit power laws ( solid lines) and for comparison the best fit isothermal model (dotted) is shown in spectrum II. All six spectra were obtained during the impulsive phase of the flare.

hard X-ray production theory, in particular the form of the cross section used to derive the photon spectrum from the electron spectrum. The RHESSI spectra shown in Section

2.3 demonstrate just how sharp a feature this ‘knee’ is.

## 1.3 Flare Stars

We have discussed the occurrence of flares on the Sun but our Sun is not unique. Many other stars display flaring events, characterised by an impulsive brightening across the electromagnetic spectrum and a gradual decay back to quiescence. The majority of so called flare stars are red dwarfs i.e. late K and M spectral types in the MK spectral classification (Giampapa 2005). In Chapter 4 we shall see that this seems to hold true for our observed flaring stars. The reason we mostly see flares on these older cooler stars is just that: they are cool stars, with typical effective temperatures of 3000K for M and 4500K for K type, and so the transient brightening of a flare stands out in contrast to the darker underlying stellar photosphere. Other earlier spectral types have also been seen to flare (Schmitt 1994) and of course our Sun is a G2V and we know that it flares. Studies of flare stars have found that all exhibit emission, to some extent, in H$\alpha$ ,Ca II H and K lines indicative of chromospheric activity (Agrawal et al 1986). This leads to the conclusion that magnetic reconnection is responsible for the transient events seen on these stars. A good example of these flaring events in the X-ray is the one which Silverman et. al . (2001) serendipitously observed whilst carrying out a survey of the RS CVn system AR Lac. This observation, Figure 1.4, clearly shows the impulsive rise to peak and the exponential decay. This is a long duration event at 1-1.5 days but clearly illustrates the X-ray profile of a flare. A shorter duration event was also observed at 4.6 hours but the temporal resolution allowed only four points to be obtained.

In the optical, Figure 1.5, we see an almost identical profile produced by a different system AT Microscopii observed by Garcia-Alvarez et. al. (2002) and at ~4000 seconds is closer to our WAVS observations which we present in Section 4.2.

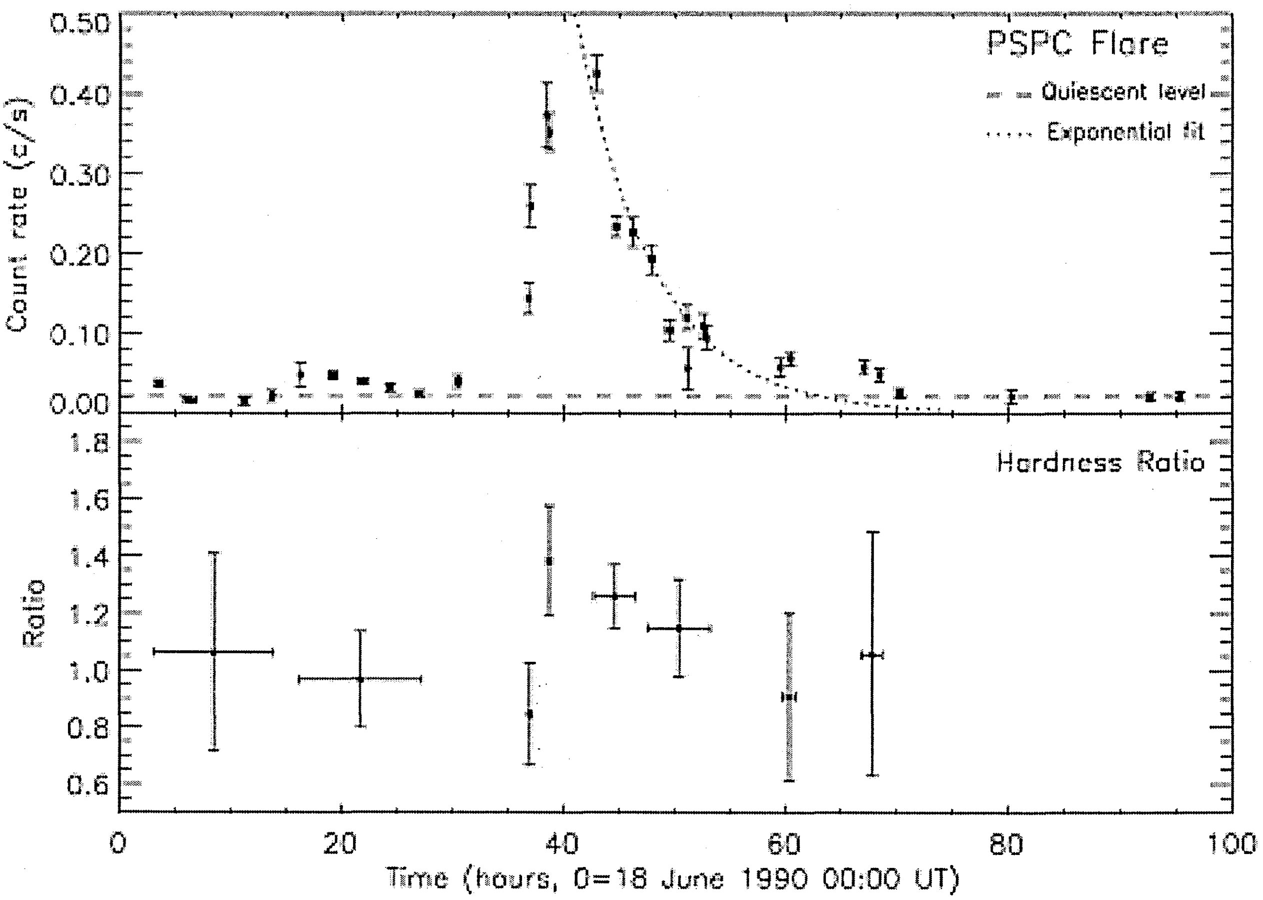

Figure 1.4: *ROSAT* PSPC observation of an M3 flare star by Silverman et. al. (2003)

## 1.4 Microquasars - Disk Flaring

Microquasars are X-ray binary systems containing a black hole or neutron star primary, an accretion disc and relativistic jets (Wu 2002). It is believed that the particles in the jets are accelerated to relativistic speeds and collimated by magnetic fields frozen into the disc. Haswell et al (1987) showed that the frozen-in field lines would be wound up by the differential rotation of the accretion disc resulting in magnetic field complexity and hence we can assume reconnection. A further link to magnetic activity in other systems is well illustrated by observations of XTEJ1118+480 where we see rapid variability in the accretion disk brightness coincident in both the optical and the X-rays (Hynes et al

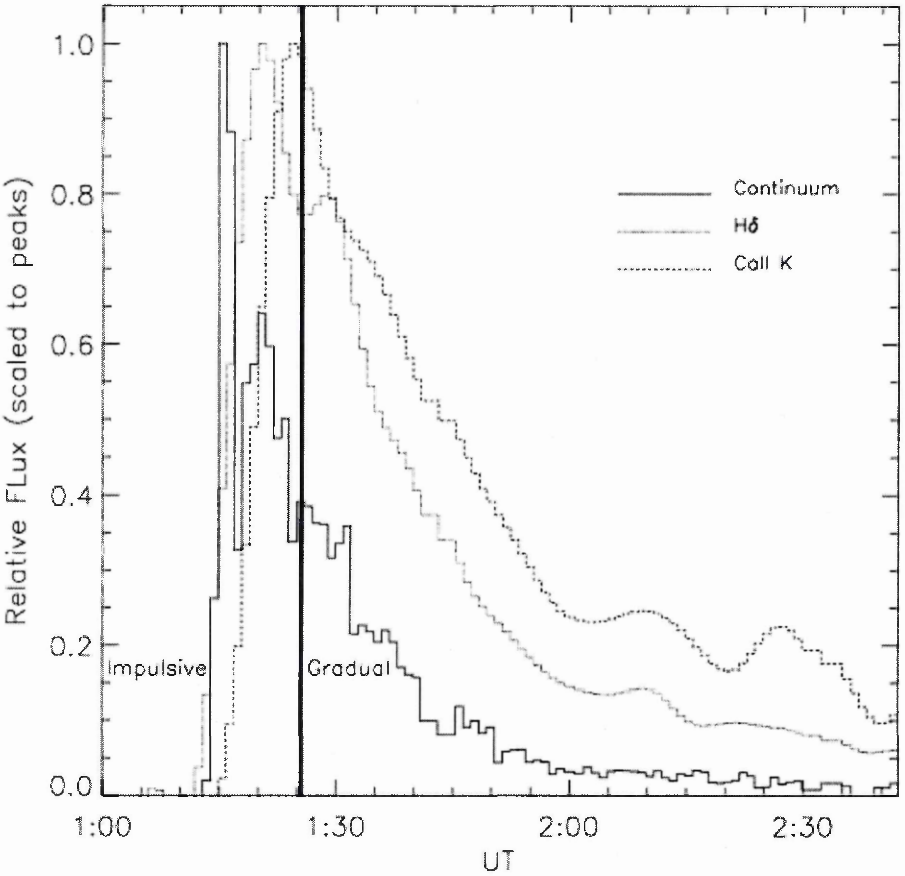

Figure 1.5: Large optical flare observed on AT Microscopii from Garcia-Alvarez et al (2002)

2003) Figure 1.6 illustrates this, also shown is the variability in the near-infrared (bottom panel). The rapid variability in the lightcurve is very reminiscent of the hard X-ray emission during the impulsive phase of a solar flare. Additionally Chaty et al (2003) tells us that the spectral energy distribution of this system is dominated by non-thermal power law emission again suggesting that the X-ray emission we see is from accelerated particles undergoing bremsstrahlung interactions.

## 1.5 Summary

We have shown that X-ray flaring occurs on a range of temporal and spatial scales and across a broad range of astrophysical environments. In the following chapters we shall present analysis of specific systems observed during thuis project.

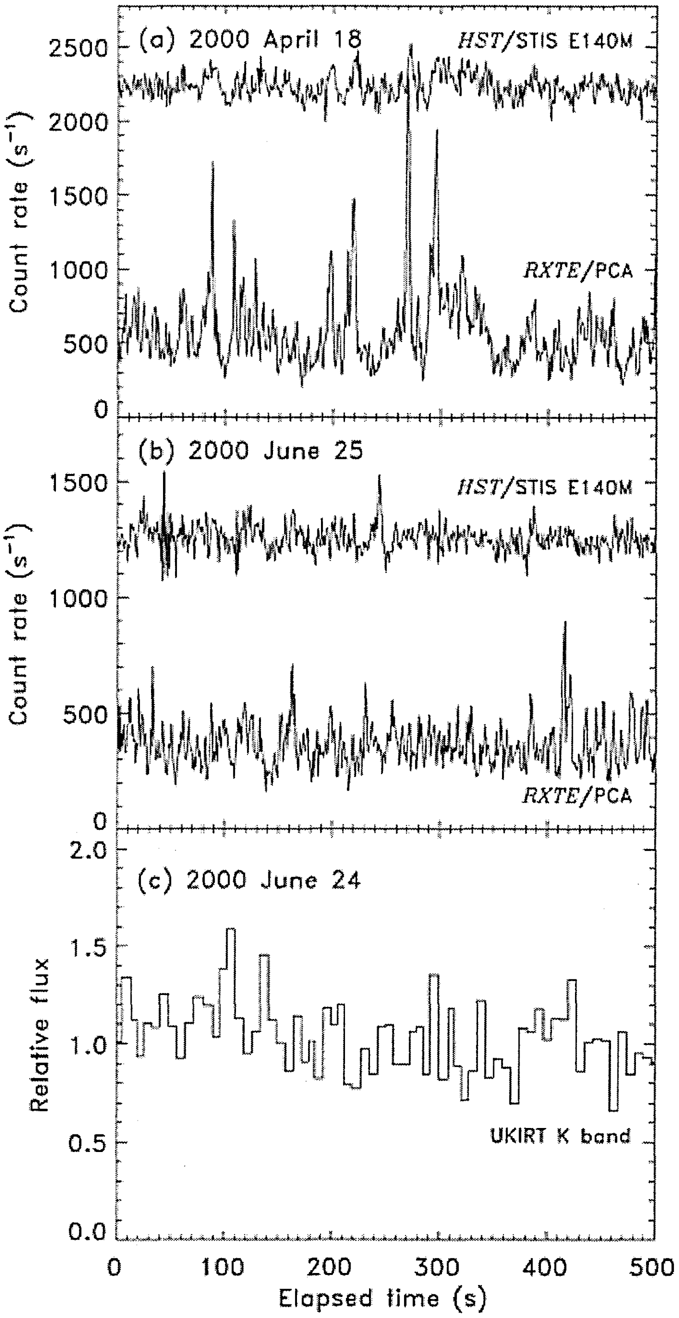

Figure 1.6: *RXTE* , *HST* and *UKIRT* observations of XTEJ1118+480 from Hynes et al 2003

# Chapter 2

# RHESSI And MEM Test

The following chapter will introduce the Reuvan Ramaty High Energy Solar Spectroscopic Imager, giving an outline of the driving science behind it, the spacecraft itself and how it 'sees' the hard X-rays emitted during a flare. Then follows a series of tests of the imaging software, done before launch, to aid in the reconstruction of images. Finally we shall present four flares that showed the characteristic 'knee' outlined in Section 1.2.1 observed in the first six months after RHESSI's launch.

## 2.1 RHESSI mission

RHESSI or the Reuven Ramaty High Energy Solar Spectroscopic Imager was launched after eighteen months of delays on the 5th February 2002. The mission consists of a single spin-stabilised spacecraft in a low Earth orbit pointing at or near to (within 0.2 degrees) Sun centre.

The RHESSI spacecraft is designed to image solar flares at very high energies, ranging from 3keV to 17MeV (Lin et. al. 2002). At these energies conventional grazing incidence optics are useless. To achieve an image we must use a different technique, collimator based, Fourier Transform imaging, Schnopper et. al. (1968).

RHESSI consists of nine Rotational Modulation Collimator's (RMC). Each RMC is made up of two grids separated by 1.5 metres in front of a hyperpure germanium crystal detector as illustrated in Figure 2.1. The grids are made of X-ray absorbing materials. The eight coarsest are made from tungsten, with the finest grid being made of molybdenum. This means that incoming X-rays are blocked by the slats of the grid or transmitted through the slits. As the grids rotate with the spacecraft, the transmission of X-rays from a point source on the Sun is modulated from 0 to 50% for sources off the spin axis. Since all nine grid pairs are of different slit widths, this gives a rudimetary Fourier transform. From an observed modulation, an image of an extended source can be reconstructed. This method can achieve a spatial resolution of better than 2.3 arcseconds and a temporal resolution of approximately 2 seconds or better, thus making RHESSI a powerful tool for studying the structural evolution of solar flares.

RHESSI can also provide spectroscopic data. The germanium detectors were chosen for their high energy resolution. This feature provides us with very high spectral resolution. In an X-ray astronomy context ΔE, the photon energy resolution, is 1 to 10keV FWHM over the full X-ray energy range. Due to this we can produce high signal to noise spectra at 1keV energy resolution up to approximately 100keV. Below 10keV we are limited by the detector response function, but this can be accounted for during analysis at the lower energy end of the spectrum. This ability to achieve such high spectral resolution can reveal some very important features in solar flare spectra.

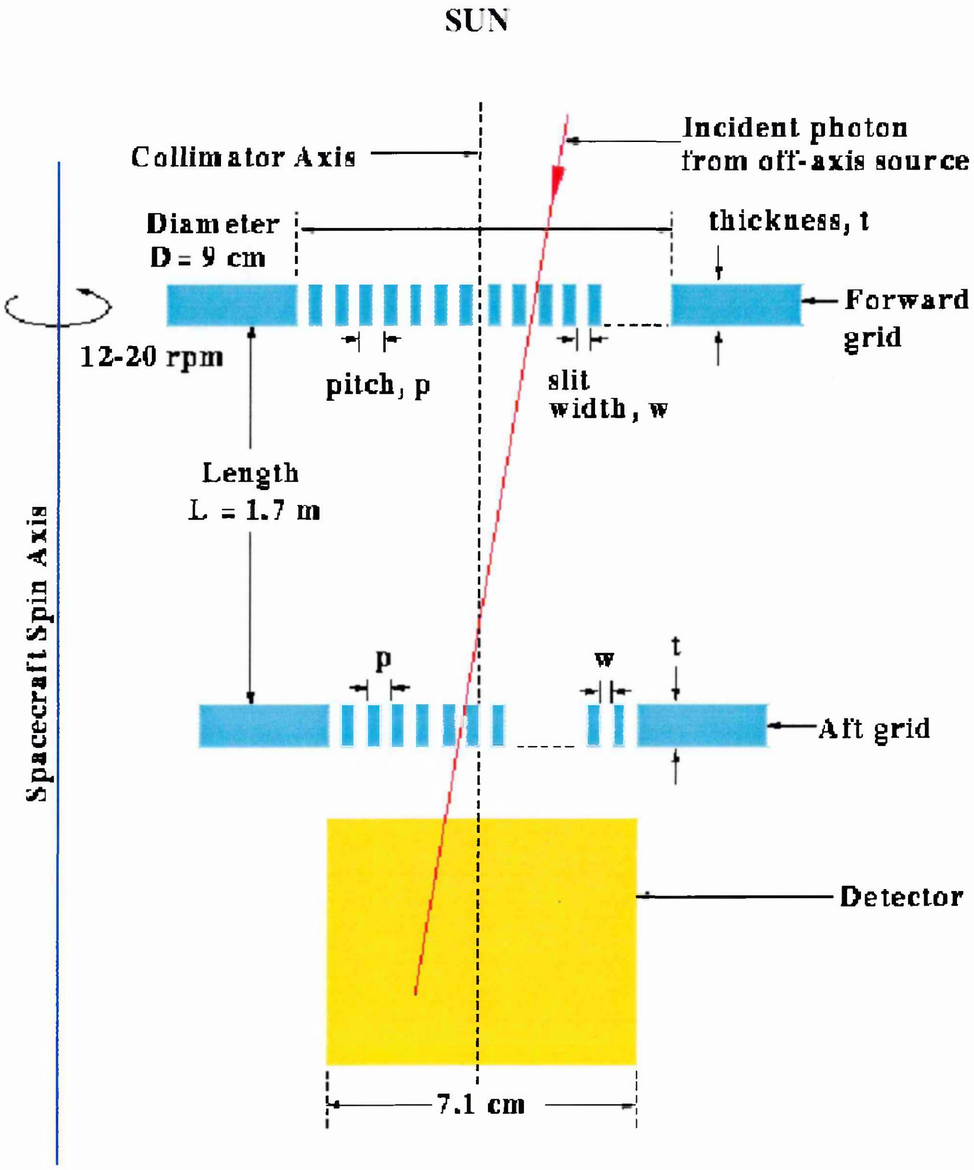

Figure 2.1: Illustration of grid pairs taken from http://hesperia.gsfc.nasa.gov/hessi courtesy of Dr Brian Dennis

### 2.1.1 RHESSI Science Objectives

High resolution hard X-ray spectroscopy is essential to understanding of the energy release and transportation within solar flares. The hard X-ray spectrum can be directly inverted to obtain the underlying electron spectrum, Section 1.2.1. RHESSI is designed to provide high spectral, spatial and temporal resolution. This allows reconstruction of the photon spectrum to be obtained for separate spatial elements within a given flare and further for a given time range during the flaring event. This gives us the ability to monitor the evolution of the bremsstrahlung emitting electrons from the acceleration site to the footpoints of the flare loop structure. The spectral resolution of the detectors on RHESSI is such that the very steep thermal spectrum can be resolved and the transition from thermally to non-thermally dominated spectrum can be observed, critical to our understanding of fast electron energy content. The spectral range needs to cover, at the lowest end, the thermal/non-thermal boundary ($\approx$20keV) and as high as possible to probe the full range of the acceleration mechanism. The dynamic range is such that small scale flares and the very large eruptions seen around solar maximum can both be observed without saturating the detectors. It isn't just the acceleration of electrons that needs to be studied to understand the nature of a flare. During the event ions are accelerated to high energies as well, producing both broad and narrow features in the gamma ray spectrum of a flare. RHESSI was designed with this in mind and the energy range of the detectors allows high resolution spectroscopy to be performed on these gamma ray features for the first time. This will allow us, for the first time, to see how the location of the high energy ions compares to that of the accelerated electrons.

Although a solar oriented mission RHESSI has the potential to to act as a high resolution monitor of the whole high energy X-ray/gamma ray sky. The lack of shielding in the rear of the space craft allows extra solar high energy events to be detected. The twice orbital occultion by the earth can provide positional information on such events. RHESSI has also been used to image the Crab nebula, possible once a year as it comes within 1.6 degrees of the Sun, with unprecedented energy resolution.

### 2.1.2 RHESSI Imaging

In order to process the raw data into the final image a variety of techniques have been developed. Here we give a brief overview (Hurford et. al. (2002)).

- Back Projection: creates a 'dirty' map by combining the counts in a given time bin with the corresponding modulation pattern (2D map of collimator responses). This preferentially populates pixels in the map that corresponding to the real sources on the Sun's disk, as in Figure 2.2a. Back projection is mainly used as a starting point for the other algorithms, and as a means to locate flares on the Sun's disk.
- CLEAN: Adapted from use in radio astronomy, at the basic level this algorithm searches for maxima in the dirty map (from Back Projection), as in Figure 2.2b.
- Maximum Entropy Method: The premise of MEM is to maximise the smoothness, of an image, whilst fitting the data to within estimated uncertainties. This is very useful in RHESSI's case as it only samples a fraction of Fourier space, the counts are the cosine fourier component of the image, see section 2.2.3 for definition of counts, and so smoothing the image 'fills in' these regions of missing data. MEM maximises the smoothness by maximising Q, given by

  $$Q = -\Sigma B_{ij} ln B_{ij} - \frac{\lambda}{2}\frac{1}{N}\Sigma\frac{(C_n - \epsilon_n)^2}{\sigma_n^2} \tag{2.1}$$

  where $B_{ij}$ is the brightness of pixel $ij$, $\lambda$ is the initial entropy multiplier (the smoothing constraint), $N$ is the number of time bins, $C_n$ is the observed counts in time bin $n$, $\epsilon_n$ is the expected counts in time bin $n$, both for pixel $ij$, from the initial guess or the subsequent reconstructed image, and $\sigma_n$ is the error in $C_n$.

Both MEM_SATO and MEM_VIS work in this way, but whilst MEM_SATO (Figure 2.2c) uses counts, MEM_VIS (Figure 2.2d) uses visibilities (complex Fourier component of the image (Conway 2000)) which for an image $B$ are defined as,

$$V(k) = \int B(\underline{r}) e^{i\underline{k}\cdot\underline{r}} dr \tag{2.2}$$

where $V(k)$ is the visibilities, $\underline{r}$ is a position vector on the Sun, and $\underline{k}$ is a vector whose magnitude depends on the grid spacing and whose direction depends on the spacecraft orientation.

- Forward Fitting: We select the number and approximate shape of the source(s) and try to modify the distribution and spatial characteristics to reproduce the observed modulation in the data. All the sources selected are either spherical, elliptical or curved gaussians. The most commonly used form is the iterative 'pixelized' method where maps of superimposed gaussians are produced for each iteration until the best fitting image is found, as shown in Figure 2.2e
- PIXON: Another MEM algorithm, although less used as it is very CPU intensive, taking hours instead of minutes to get an image, takes the global smoothing idea of MEM but applies it locally. The PIXON algorithm is also multiresolutional and so areas of high data content are displayed at higher spatial resolution i.e. smaller pixels, than less data rich regions. PIXON is best used to generate a final image map, using information gained from the other algorithms, as shown in Figure 2.2f.

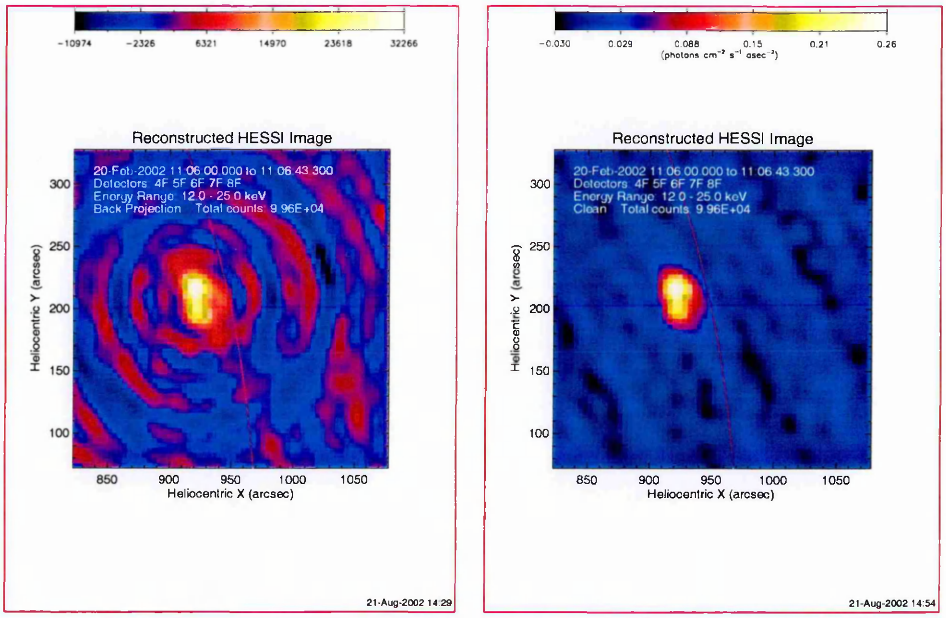

(a) BACK PROJECTION

(b) CLEAN

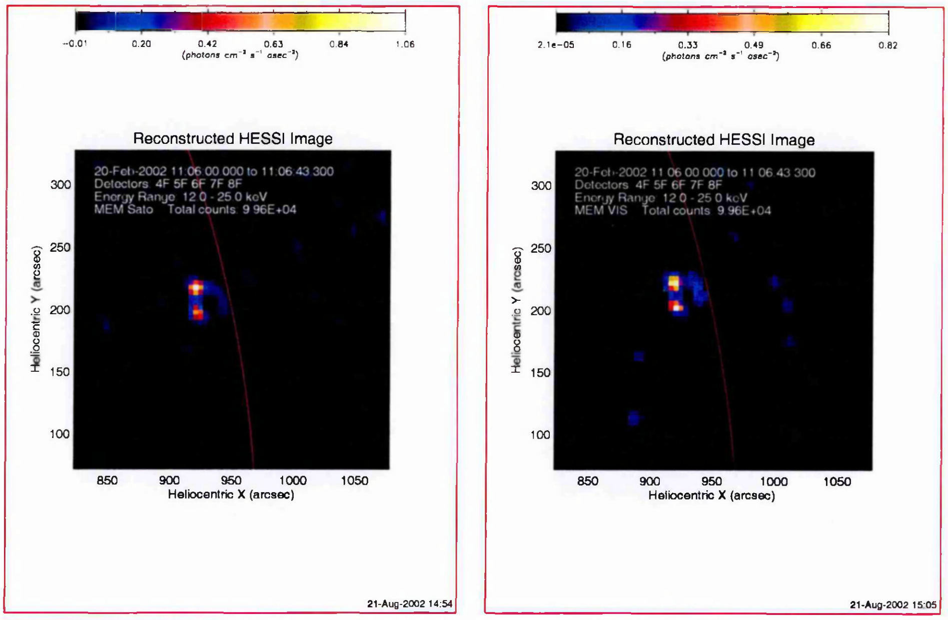

(c) MEM_SATO (d) MEM_VIS

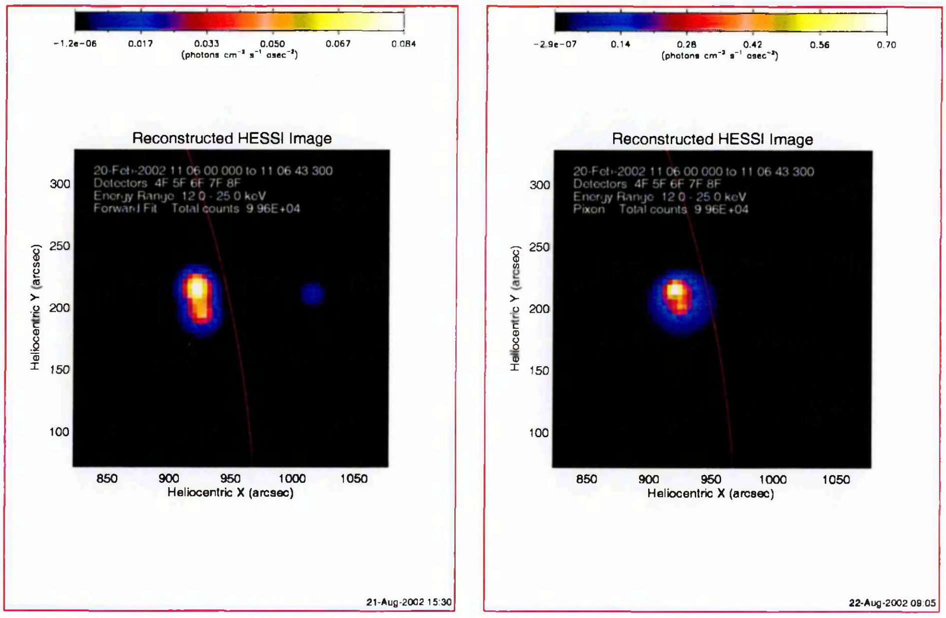

(e) FORWARD FITTING (f) PIXON

Figure 2.2: Reconstructions of the 20th February 2002 11:06UT flare with the six imaging algorithms. Using a 12 - 25 keV energy band, over a time interval of 43.3 seconds (10 rotations of RHESSI), with default detectors 4,5,6,7, and 8.

## 2.2 Tests of maximum entropy reconstruction on simulated RHESSI data

### 2.2.1 Introduction

Maximum Entropy Methods (MEMs) provide a solid method of image reconstruction for limited data such as the RHESSI modulation profiles, where the data are limited in the sense that some of the information from the object is absent. This is due to the grids used to obtain the profile having less than 100% transmission of photons. The question remains as to how representative these reconstructions are of the original flare, as very different images can be obtained from the same modulation profile. To this end I have run numerous reconstructions of three test cases, for both MEM_SATO and MEM_VIS, to assess the effect the initial entropy multiplier has on reconstructions of sources with various brightness and compactness.

### 2.2.2 Method

The initial entropy multiplier `lnorm` or $\lambda$ in equation 2.1 governs the initial smoothness constraint. The lower the value of $\lambda$ the more smooth an image has to be. For small values, entropy is a strong constraint to the detriment of a good fit to the data. Conversely, for large `lnorm` values entropy is a weaker constraint and leads to a good fit to data. In the case of the MEM algorithms, a reduced $\chi^2$ statistic is used to measure the goodness of fit, but can lead to the breaking up of smooth, extended sources. Due to this we attempted to find the best values for `lnorm` in both MEM_SATO and MEM_VIS for three different types of source at varying brightnesses, in order to reconstruct the most realistic image. The three test sources are a point source, a $10'' \times 20''$ Gaussian and a $20'' \times 40''$ Gaussian of the same total brightness. The simulations were generated through the hsi_image object, defining three Gaussians, one with `xysigma` set to default (0.001, 0.001), one of `xysigma`=[10.,20.], and one of `xysigma`=[20.,40.]. This produces three Gaussian sources where the brightness of the source falls off for the given 1$\sigma$ value in each direction. To make the test equal for both algorithms CHI_LIMIT was set to MEM_SATO's default of 1.03 for both and LAMBDA_MAX (the maximum number of iterations) was set to 150. This was necessary to prevent the software from being caught in an infinite loop. Thus the reconstruction ends if number of iterations reaches 150 or if a $\chi^2$ of 1.03 is reached. MEM_SATO also stops if $\Delta\chi^2$ between two reconstructed images is not large enough.

With these constraints we then ran image reconstructions of all three sources for the following combinations of `lnorm` and SIM_PHOTONS_PER_COLL (number of photons per collimator per second).

SIM_PHOTONS_PER_COLL = 7500, 37500, 75000, 375000.

MEM_SATO `lnorm` = 1, 0.5, 0.1, 5e-2, 1e-2.

MEM_VIS `lnorm` = 1e-3, 5e-3, 1e-4, 5e-5, 1e-5.

NB. The default `lnorm` for MEM_SATO is 0.1 and for MEM_VIS 1e-5.

After each reconstruction the reconstructed image was saved along with the parameters `btot`, final $\chi^2$ and number of iterations. The parameter `btot` is the total image brightness used in the reconstruction algorithm. Since the energy range is set to 6keV to 100keV `btot` should be somewhat less than the value of SIM_PHOTONS_PER_COLL since `btot` is per unit area and we only use some of the subcollimators.

### 2.2.3 Results

Both algorithms could reconstruct the point source with little difficulty so we only present the reconstructed images of the extended sources for certain arbitrary input parameters.

Figures 2.3 (page 29) and 2.5 (page 33) show that changes to SATO_LNORM have little effect over our range and MEM_SATO has difficulty in identifying that the source is a single large source rather than a collection of points. MEM_SATO performs better at higher counts and for the 20″×40″ sources in Figure 2.3 and the 10″×20″ source, in Figure 2.5 at 375000 SIM_PHOTONS_PER_COLL we see a definite single extended source with little spurious structure. For the 20″× 40″ source at high counts we see the extended source as a cluster of point sources plus some faint tendril like structure. At low counts the central source is indistinguishable from the background of spurious point sources.

Figures 2.4 (page 30) and 2.6 (page 34)show that with a small `lnorm` MEM_VIS reconstructs a diffuse source but shows much structure where there is none. For higher `lnorm` the image resembles a collection of point sources, this is true for both extended sources, although the 10″×20″ source shows less internal structure than the 20″×40″ source. At high counts even at `lnorm`=1e-4 we see a collection of point sources for both test simulations.

For MEM_SATO, at high counts the image is relatively less fragmented at the same `lnorm` than for lower counts. For MEM_VIS the opposite is seen as less internal structure is present for increasing counts for `lnorm`=1e-5.

The fragmentation could be caused by the systematic errors that MEM_VIS incurs when it converts counts to visibilities, as they become more important at higher counts as shown below. The counts are defined as the cosine fourier component of the image given by,

$$C(k) = \int B(\underline{r})\cos(\underline{k}.\underline{r} + \phi)\mathrm{dr} \tag{2.3}$$

where $\underline{k}$ and $\underline{r}$ are as defined in equation 2.3 and $\phi$ is the phase introduced because the spin axis wanders over the Sun during a rotation, and so is time dependent. Converting from counts to visibilities involves correcting for $\phi$ and constructing the imaginary parts of the visibilities. It is during this process that the systematic errors are introduced. The form of the errors is such that the variance of the visibilities can be expressed as ${\sigma_P}^2 + {\sigma_S}^2$, where $\sigma_P$ represents the poisson noise and is proportional to counts and $\sigma_S$ represents the systematic errors introduced and is proportional to the square of the counts. So for low counts ${\sigma_S}^2$ is smaller than ${\sigma_P}^2$ and so systematic errors are not important, at higher counts the ${\sigma_S}^2$ term dominates and the systematic errors become important. Therefore at higher counts a $\chi^2$ of 1 is a fit to the systematic errors rather than a fit to the relevant data.

Another cause of spurious structure could be the fact that both MEM_SATO and MEM_VIS use the modulations from all detectors given as default (i.e. 4, 5, 6, 7, and 8 of the 9 detectors), where 1 is the finest and 9 is the coarsest detector, even if they contain no relevant modulation. This give spurious structure since for a large extended source the modulation of the fine grids would be negligible.

To test this hypothesis a further reconstruction run was performed using only detectors 5, 6, and 7, with a SATO_LNORM of 0.1, and 1e-2, VIS_LNORM of 1e-4, and 1e-5.

Table 2.1: MEM_SATO output for 20″×40″ Gaussian source

| Source | Photons/$s^{-1}$ coll.$^{-1}$ | `lnorm` | Final $\chi^2$ | No. of Lambda iterations | `btot` |
|---|---|---|---|---|---|
| 20″×40″ | 7500 | 1 | 1.03 | 1 | 920 |
| 20″×40″ | 7500 | 0.5 | 1.03 | 2 | 922 |
| 20″×40″ | 7500 | 0.1 | 1.03 | 10 | 922 |
| 20″×40″ | 7500 | 5e-2 | 1.03 | 20 | 922 |
| 20″×40″ | 7500 | 1e-2 | 1.03 | 101 | 922 |
| 20″×40″ | 37500 | 1 | 0.998 | 2 | 4530 |
| 20″×40″ | 37500 | 0.5 | 0.9987 | 4 | 4530 |
| 20″×40″ | 37500 | 0.1 | 1.02 | 17 | 4540 |
| 20″×40″ | 37500 | 5e-2 | 1.03 | 32 | 4540 |
| 20″×40″ | 37500 | 1e-2 | 1.04 | 144 | 4540 |
| 20″×40″ | 75000 | 1 | 1.02 | 3 | 8980 |
| 20″×40″ | 75000 | 0.5 | 1.02 | 6 | 8990 |
| 20″×40″ | 75000 | 0.1 | 1.03 | 29 | 8990 |
| 20″×40″ | 75000 | 5e-2 | 1.03 | 59 | 8990 |
| 20″×40″ | 75000 | 1e-2 | 1.14 | 144 | 9010 |
| 20″×40″ | 375000 | 1 | 1.42 | 2 | 44200 |
| 20″×40″ | 375000 | 0.5 | 1.02 | 6 | 44100 |
| 20″×40″ | 375000 | 0.1 | 1.02 | 29 | 44200 |
| 20″×40″ | 375000 | 5e-2 | 1.02 | 59 | 44200 |
| 20″×40″ | 375000 | 1e-2 | 1.23 | 144 | 44300 |

Table 2.2: MEM_VIS output for 20″×40″ Gaussian source

| Source | Photons/$s^{-1}$ /coll. | `lnorm` | Final $\chi^2$ | No. of Lambda iterations | `btot` |
|---|---|---|---|---|---|
| 20″×40″ | 7500 | 1e-3 | 0.990 | 1 | 893 |
| 20″×40″ | 7500 | 5e-3 | 1.02 | 4 | 893 |
| 20″×40″ | 7500 | 1e-4 | 1.03 | 4 | 893 |
| 20″×40″ | 7500 | 5e-5 | 1.01 | 7 | 893 |
| 20″×40″ | 7500 | 1e-5 | 1.03 | 32 | 893 |
| 20″×40″ | 37500 | 1e-3 | 1.02 | 30 | 4580 |
| 20″×40″ | 37500 | 5e-3 | 1.02 | 46 | 4580 |
| 20″×40″ | 37500 | 1e-4 | 0.987 | 5 | 4580 |
| 20″×40″ | 37500 | 5e-4 | 1.02 | 8 | 4580 |
| 20″×40″ | 37500 | 5e-5 | 1.02 | 40 | 4580 |
| 20″×40″ | 75000 | 1e-3 | 1.01 | 117 | 9190 |
| 20″×40″ | 75000 | 5e-3 | 1.06 | 157 | 9190 |
| 20″×40″ | 75000 | 1e-4 | 1.02 | 49 | 9190 |
| 20″×40″ | 75000 | 5e-5 | 0.994 | 11 | 9190 |
| 20″×40″ | 75000 | 1e-5 | 1.03 | 46 | 9190 |
| 20″×40″ | 375000 | 1e-3 | 2.44 | 156 | 45100 |
| 20″×40″ | 375000 | 5e-3 | 1.66 | 163 | 45100 |
| 20″×40″ | 375000 | 1e-4 | 1.96 | 160 | 45100 |
| 20″×40″ | 375000 | 5e-5 | 2.19 | 164 | 45100 |
| 20″×40″ | 375000 | 1e-5 | 0.929 | 56 | 45100 |

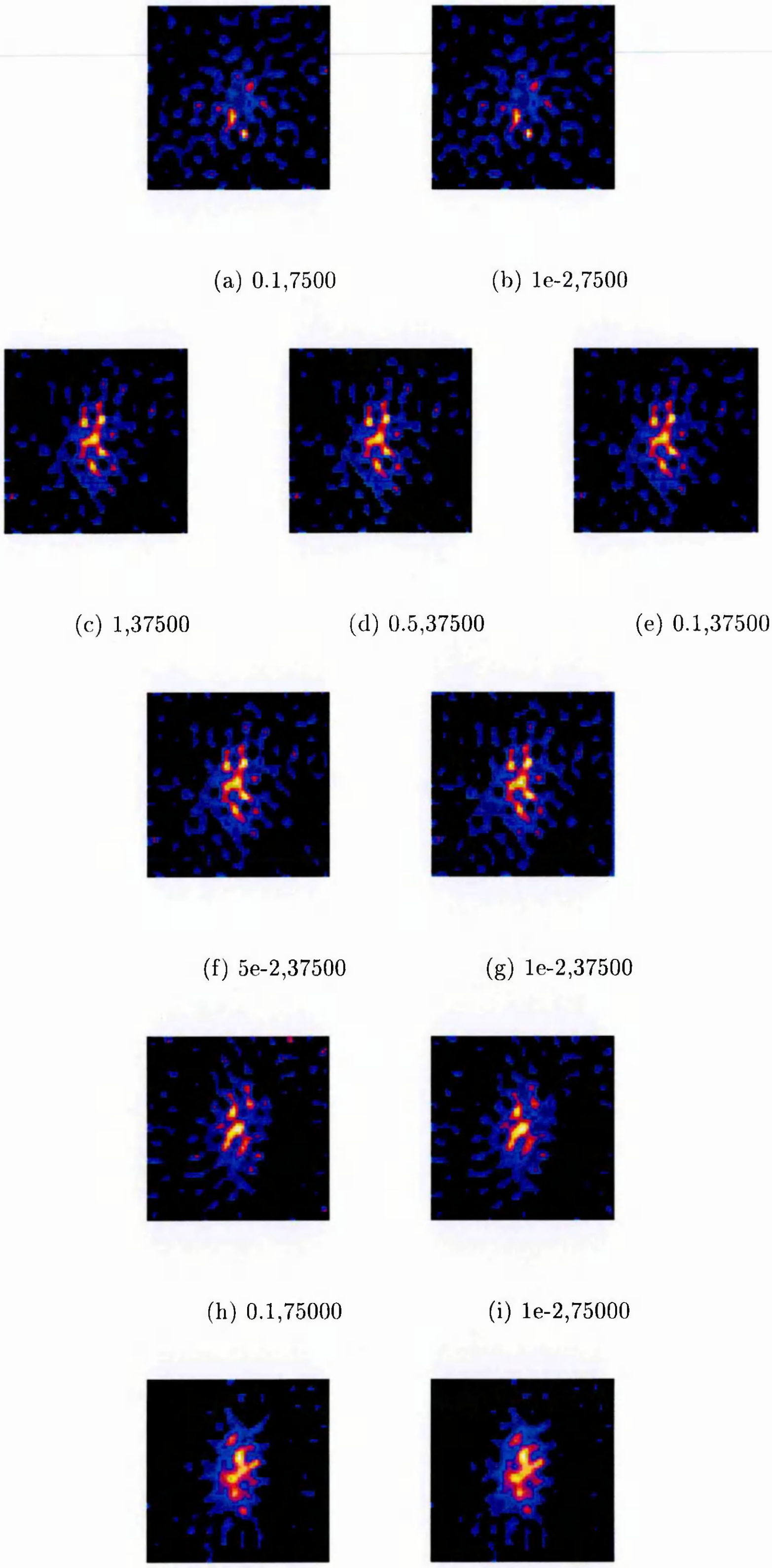

(a) 0.1,7500 (b) 1e-2,7500

(c) 1,37500 (d) 0.5,37500 (e) 0.1,37500

(f) 5e-2,37500 (g) 1e-2,37500

(h) 0.1,75000 (i) 1e-2,75000

(j) 0.1,375000 (k) 1e-2,375000

Figure 2.3: Reconstructed images for a 20″ by 40″ Gaussian Source with MEM_SATO. Each image has its associated `lnorm` and SIM_PHOTONS_PER_COLL value printed below it. All figures in this section are 64 x 64 pixel images with 4″ x4″ pixels, giving 256″ by 256″ images.

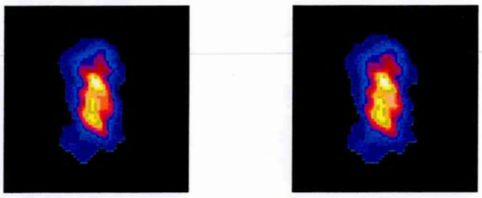

(a) 1e-4,7500 (b) 1e-5,7500

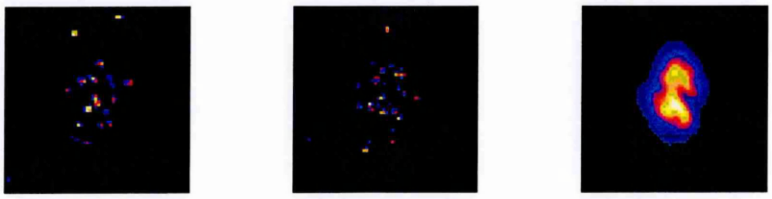

(c) 1e-3,37500 (d) 5e-3,37500 (e) 1e-4,37500

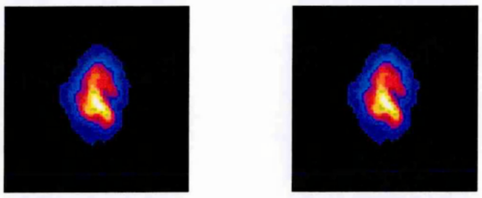

(f) 5e-5,37500 (g) 1e-5,37500

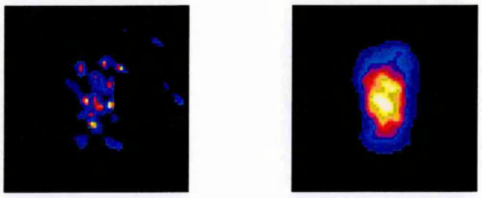

(h) 1e-4,75000 (i) 1e-5,75000

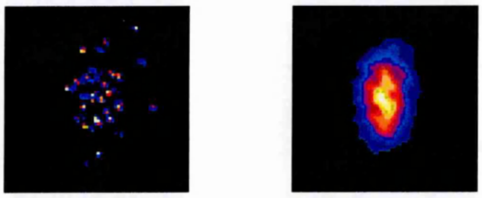

(j) 1e-4,375000 (k) 1e-5,375000

Figure 2.4: Reconstructed images for a 20″ by 40″ Gaussian Source with MEM_VIS. Each image has its associated `lnorm` and SIM_PHOTONS_PER_COLL value printed below it. All figures in this section are 64 x 64 pixel images with 4″ x4″ pixels, giving 256″ by 256″ images.

Table 2.3: MEM_SATO output for 10″×20″ Gaussian source

| Source | Photons/$s^{-1}$ /coll. | `lnorm` | Final $\chi^2$ | No. of Lambda iterations | `btot` |
|---|---|---|---|---|---|
| 10″×20″ | 7500 | 1 | 1.03 | 4 | 915 |
| 10″×20″ | 7500 | 0.5 | 1.03 | 8 | 915 |
| 10″×20″ | 7500 | 0.1 | 1.03 | 39 | 915 |
| 10″×20″ | 7500 | 5e-2 | 1.19 | 17 | 928 |
| 10″×20″ | 7500 | 1e-2 | 1.10 | 144 | 922 |
| 10″×20″ | 37500 | 1 | 1.03 | 3 | 4490 |
| 10″×20″ | 37500 | 0.5 | 1.03 | 6 | 4500 |
| 10″×20″ | 37500 | 0.1 | 1.03 | 29 | 4500 |
| 10″×20″ | 37500 | 5e-2 | 1.03 | 59 | 4500 |
| 10″×20″ | 37500 | 1e-2 | 1.15 | 144 | 4520 |
| 10″×20″ | 75000 | 1 | 1.01 | 3 | 9000 |
| 10″×20″ | 75000 | 0.5 | 1.01 | 6 | 9000 |
| 10″×20″ | 75000 | 0.1 | 1.03 | 26 | 9020 |
| 10″×20″ | 75000 | 5e-2 | 1.02 | 55 | 9020 |
| 10″×20″ | 75000 | 1e-2 | 1.18 | 144 | 9050 |
| 10″×20″ | 375000 | 1 | 1.78 | 2 | 43400 |
| 10″×20″ | 375000 | 0.5 | 1.20 | 6 | 44100 |
| 10″×20″ | 375000 | 0.1 | 1.03 | 43 | 44100 |
| 10″×20″ | 375000 | 5e-2 | 1.03 | 86 | 44100 |
| 10″×20″ | 375000 | 1e-2 | 1.39 | 144 | 44300 |

Table 2.4: MEM_VIS output for 10″×20″ Gaussian source

| Source | Photons/$s^{-1}$ /coll. | `lnorm` | Final $\chi^2$ | No. of Lambda iterations | `btot` |
|---|---|---|---|---|---|
| 10″×20″ | 7500 | 1e-3 | 1.02 | 1 | 903 |
| 10″×20″ | 7500 | 5e-3 | 1.00 | 2 | 903 |
| 10″×20″ | 7500 | 1e-4 | 1.03 | 4 | 903 |
| 10″×20″ | 7500 | 5e-5 | 1.03 | 8 | 903 |
| 10″×20″ | 7500 | 1e-5 | 1.03 | 41 | 903 |
| 10″×20″ | 37500 | 1e-3 | 0.873 | 14 | 4630 |
| 10″×20″ | 37500 | 5e-3 | 0.978 | 8 | 4630 |
| 10″×20″ | 37500 | 1e-4 | 0.939 | 4 | 4630 |
| 10″×20″ | 37500 | 5e-5 | 1.01 | 7 | 4630 |
| 10″×20″ | 37500 | 1e-5 | 1.01 | 35 | 4630 |
| 10″×20″ | 75000 | 1e-3 | 1.02 | 56 | 9320 |
| 10″×20″ | 75000 | 5e-3 | 1.02 | 38 | 9320 |
| 10″×20″ | 75000 | 1e-4 | 0.962 | 11 | 9320 |
| 10″×20″ | 75000 | 5e-5 | 0.986 | 16 | 9320 |
| 10″×20″ | 75000 | 1e-5 | 1.02 | 60 | 9320 |
| 10″×20″ | 375000 | 1e-3 | 2.13 | 158 | 45500 |
| 10″×20″ | 375000 | 5e-4 | 2.20 | 162 | 45500 |
| 10″×20″ | 375000 | 1e-4 | 2.85 | 156 | 45500 |
| 10″×20″ | 375000 | 5e-5 | 2.17 | 155 | 45500 |
| 10″×20″ | 375000 | 1e-5 | 1.34 | 160 | 45500 |

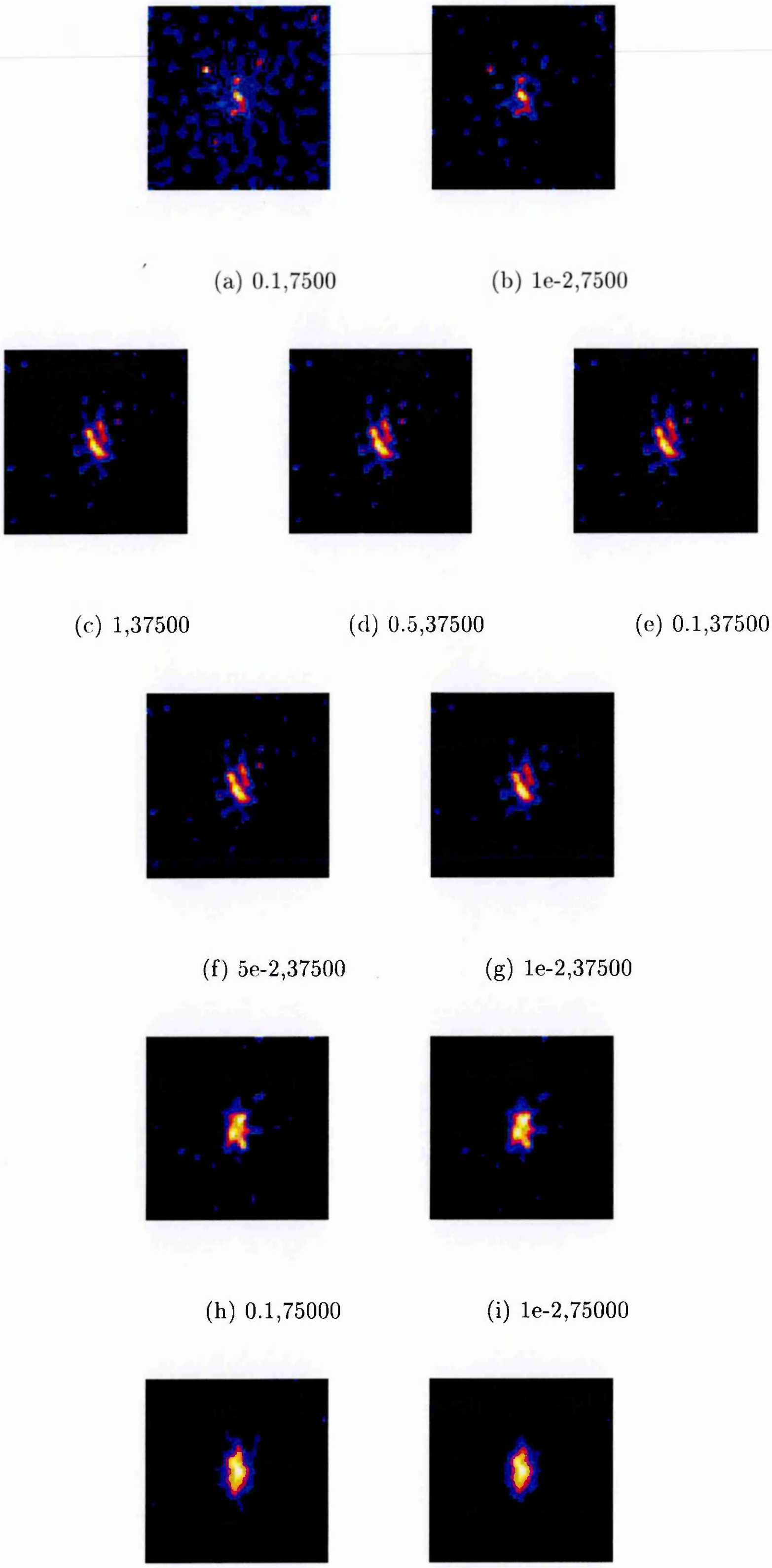

(a) 0.1,7500
(b) 1e-2,7500
(c) 1,37500
(d) 0.5,37500
(e) 0.1,37500
(f) 5e-2,37500
(g) 1e-2,37500
(h) 0.1,75000
(i) 1e-2,75000
(j) 0.1,375000
(k) 1e-2,375000

Figure 2.5: Reconstructed images for a 10″by 20″ Gaussian Source with MEM_SATO. Each image has its associated `lnorm` and SIM_PHOTONS_PER_COLL value printed below it. All figures in this section are 64 x 64 pixel images with 4″ x4″ pixels, giving 256″ by 256″ images.

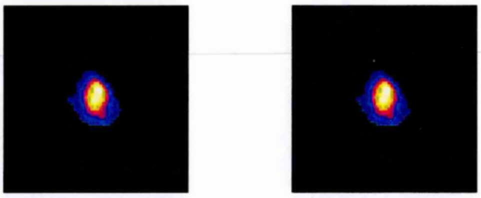

(a) 1e-4,7500 (b) 1e-5,7500

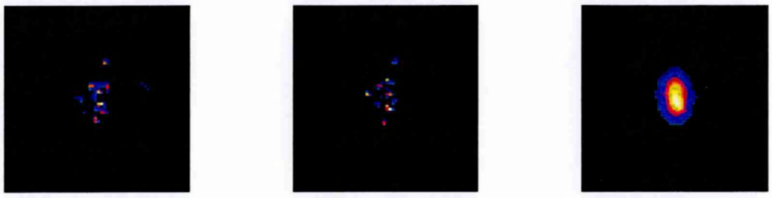

(c) 1e-3,37500 (d) 5e-3,37500 (e) 1e-4,37500

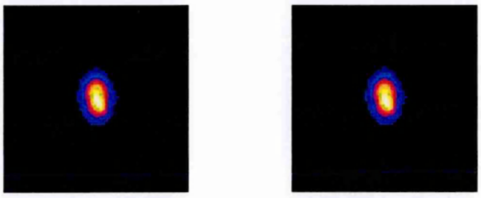

(f) 5e-5,37500 (g) 1e-5,37500

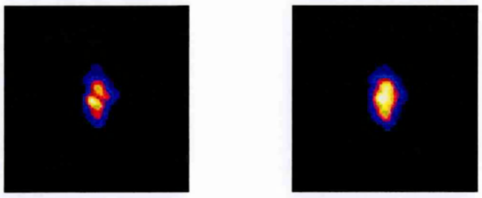

(h) 1e-4,75000 (i) 1e-5,75000

(j) 1e-4,375000 (k) 1e-5,375000

Figure 2.6: Reconstructed images for a $10''$ by $20''$ Gaussian Source with MEM_VIS. Each image has its associated `lnorm` and SIM_PHOTONS_PER_COLL value printed below it. All figures in this section are 64 x 64 pixel images with $4''$ x$4''$ pixels, giving $256''$ by $256''$ images.

*Results: Reconstructions with only detectors 5, 6, and 7.*

---

We can see from Figure 2.7 (page 37)that although MEM_SATO still produces images with spurious structure at the lower counts there is no breaking up of the image into point sources and there is a definite large central source. At the higher counts we get a good representation of the 20″ × 40″ source. The same can be said for the 10″ × 20″ source in Figure 2.9 (page 41), although at the lower counts we do see less spurious structure than for the more diffuse larger source.

MEM_VIS (Figure 2.8 (page 39)) also shows less internal structure than previously but still displays fragmentation at high counts, and for `lnorm`=1e-5, SIM_PHOTONS_PER_COLL = 375000 the image is even more fragmented than the default detectors run. A similar occurrence can be seen in Figure 2.10 (page 43) for the 10″×20″ source. Note that the final run in Figure 2.10 was performed with a different realisation of the simulated model to the others, due to software problems, this is also why the final `btot` is relatively lower than the other SIM_PHOTONS_PER_COLL = 375000 run compared to the lower count runs.

### 2.2.4 Conclusions

Both MEM_VIS and MEM_SATO performed well on the point sources, with little change between `lnorm`'s. For low counts MEM_VIS performs much better than MEM_SATO for the 20″ × 40″ Gaussian source, but for the 10″ × 20″ Gaussian source it returns a more accurately reconstructed image for only the lowest counts and MEM_SATO produces more consistent reconstructions for increasing counts. We must bear in mind that, unlike MEM_VIS, MEM_SATO does not have any systematic errors, when used in simulation, and so at high counts where they would dominate we see no evidence of this and so see no image break up in Figure 2.3 at high counts.

In terms of the increasing of the initial entropy multiplier `lnorm` we see very little effect on the MEM_SATO reconstructions over the range 1 to 1e-2 and it would appear that counts are the dominant factor. In MEM_VIS high counts cause image break up due to fitting of the systematic errors, but for low to medium counts (7500 to 75000) the effect of increasing the value of `lnorm` from it's default of 1e-5 is extremely noticeable and causes a great deal of fragmentation.

MEM_SATO is robust to the point of being insensitive to changes in `lnorm`, but this could be due to the entropy constraint being effectively turned off at `lnorm` $\geq 0.1$ and so increasing `lnorm` is effectively useless. MEM_SATO also performed better for the smaller sources than the large diffuse source and this is worth bearing in mind for future work. It would be interesting to see if image fragmentation increased with increasing counts if the systematic errors were present in the simulation.

MEM_VIS is very sensitive to increases in `lnorm`, but at its default (1e-5) performs well for counts $< 375000$ in this test, before systematic errors dominate. It outperforms MEM_SATO for the $20'' \times 40''$ source in both detector regimes apart from at higher counts.

In conclusion, MEM_SATO as it is now is very good for smaller sources at high counts, MEM_VIS is better at low `lnorm` and low counts, and for larger diffuse sources.

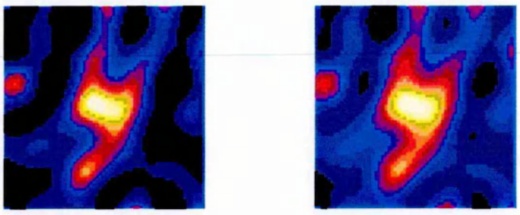

(a) 0.1,7500 (b) 1e-2,7500

(c) 0.1,37500 (d) 1e-2,37500

(e) 0.1,75000 (f) 1e-2,75000

(g) 0.1,375000 (h) 1e-2,375000

Figure 2.7: MEM_SATO reconstructions for a $20'' \times 40''$ Gaussian source using detectors 5, 6 and 7. Each image has its associated `lnorm` and SIM_PHOTONS_PER_COLL value printed below it. All figures in this section are 64 x 64 pixel images with $4''$ x$4''$ pixels, giving $256''$ by $256''$ images.

Table 2.5: MEM_SATO output for 20″×40″ Gaussian source using detectors 5, 6 and 7.

| Source | Photons/$s^{-1}$ /coll. | `lnorm` | Final $\chi^2$ | No. of Lambda iterations | `btot` |
|---|---|---|---|---|---|
| 20″×40″ | 7500 | 0.1 | 1.02 | 29 | 917 |
| 20″×40″ | 7500 | 1e-2 | 1.11 | 144 | 922 |
| 20″×40″ | 37500 | 0.1 | 1.06 | 144 | 4520 |
| 20″×40″ | 37500 | 1e-2 | 1.64 | 144 | 4570 |
| 20″×40″ | 75000 | 0.1 | 1.03 | 39 | 8990 |
| 20″×40″ | 75000 | 1e-2 | 1.56 | 144 | 9040 |
| 20″×40″ | 375000 | 0.1 | 1.02 | 59 | 44000 |
| 20″×40″ | 375000 | 1e-2 | 2.24 | 144 | 44300 |

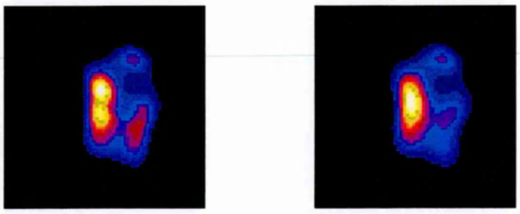

(a) 1e-4,7500 (b) 1e-5,7500

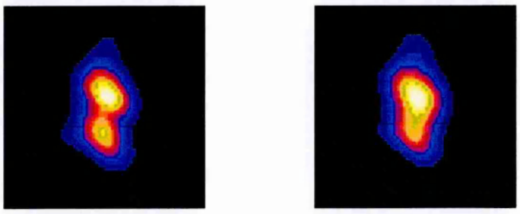

(c) 1e-4,37500 (d) 1e-5,37500

(e) 1e-4,75000 (f) 1e-5,75000

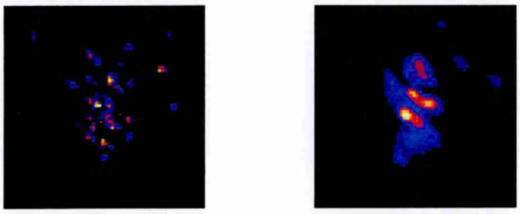

(g) 1e-4,375000 (h) 1e-5,375000

Figure 2.8: MEM_VIS reconstructions for a $20'' \times 40''$ Gaussian source using detectors 5, 6 and 7. Each image has its associated `lnorm` and SIM_PHOTONS_PER_COLL value printed below it. All figures in this section are 64 x 64 pixel images with $4''$ x$4''$ pixels, giving $256''$ by $256''$ images.

Table 2.6: MEM_VIS output for 20″×40″ Gaussian source using detectors 5, 6 and 7.

| Source | Photons/$s^{-1}$ /coll. | `lnorm` | Final $\chi^2$ | No. of Lambda iterations | `btot` |
|---|---|---|---|---|---|
| 20″×40″ | 7500 | 1e-4 | 1.02 | 14 | 918 |
| 20″×40″ | 7500 | 1e-5 | 1.03 | 86 | 918 |
| 20″×40″ | 37500 | 1e-4 | 0.947 | 2 | 4640 |
| 20″×40″ | 37500 | 1e-5 | 1.02 | 24 | 4640 |
| 20″×40″ | 75000 | 1e-4 | 0.992 | 103 | 9280 |
| 20″×40″ | 75000 | 1e-5 | 1.03 | 39 | 9280 |
| 20″×40″ | 375000 | 1e-4 | 2.25 | 154 | 46000 |
| 20″×40″ | 375000 | 1e-5 | 1.80 | 159 | 46000 |

(a) 0.1,7500 (b) 1e-2,7500

(c) 0.1,37500 (d) 1e-2,37500

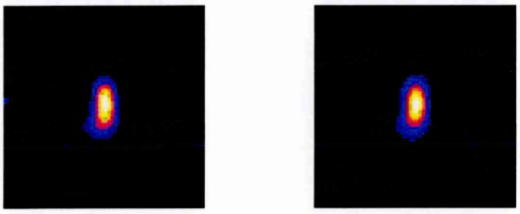

(e) 0.1,75000 (f) 1e-2,75000

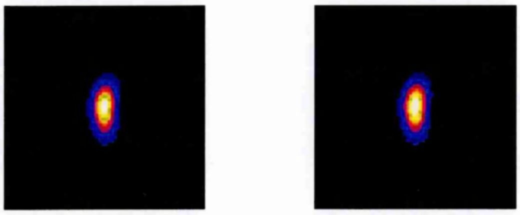

(g) 0.1,375000 (h) 1e-2,375000

Figure 2.9: MEM_SATO reconstructions for a $10'' \times 20''$ Gaussian source using detectors 5, 6 and 7. Each image has its associated `lnorm` and SIM_PHOTONS_PER_COLL value printed below it. All figures in this section are 64 x 64 pixel images with $4''$ x$4''$ pixels, giving $256''$ by $256''$ images.

Table 2.7: MEM_SATO output for 10″×20″ Gaussian source using detectors 5, 6 and 7.

| Source | Photons/$s^{-1}$ /coll. | `lnorm` | Final $\chi^2$ | No. of Lambda iterations | `btot` |
|---|---|---|---|---|---|
| 10″×20″ | 375000 | 0.1 | 1.00 | 6 | 911 |
| 10″×20″ | 375000 | 1e-2 | 1.02 | 51 | 911 |
| 10″×20″ | 375000 | 0.1 | 1.03 | 32 | 4570 |
| 10″×20″ | 375000 | 1e-2 | 1.06 | 144 | 4590 |
| 10″×20″ | 375000 | 0.1 | 1.05 | 47 | 8960 |
| 10″×20″ | 375000 | 1e-2 | 1.09 | 144 | 9030 |
| 10″×20″ | 375000 | 0.1 | 1.06 | 17 | 43800 |
| 10″×20″ | 375000 | 1e-2 | 1.06 | 144 | 43900 |

Table 2.8: MEM_VIS output for 10″×20″ Gaussian source using detectors 5, 6 and 7.

| Source | Photons/$s^{-1}$ /coll. | `lnorm` | Final $\chi^2$ | No. of Lambda iterations | `btot` |
|---|---|---|---|---|---|
| 10″×20″ | 7500 | 1e-4 | 1.01 | 16 | 938 |
| 10″×20″ | 7500 | 1e-5 | 1.03 | 89 | 938 |
| 10″×20″ | 37500 | 1e-4 | 0.942 | 5 | 4790 |
| 10″×20″ | 37500 | 1e-5 | 1.02 | 39 | 4790 |
| 10″×20″ | 75000 | 1e-4 | 0.975 | 93 | 9570 |
| 10″×20″ | 75000 | 1e-5 | 1.01 | 57 | 9570 |
| 10″×20″ | 375000 | 1e-4 | 3.58 | 157 | 46900 |
| 10″×20″ | 375000 | 1e-5 | 2.17 | 159 | 46900 |

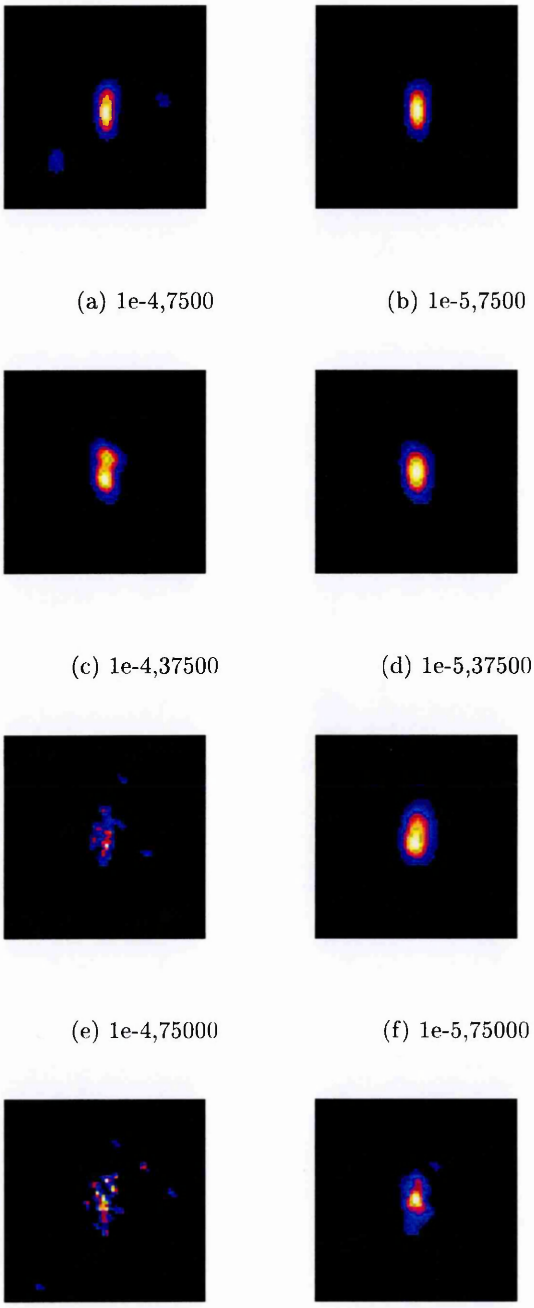

(a) 1e-4,7500

(b) 1e-5,7500

(c) 1e-4,37500

(d) 1e-5,37500

(e) 1e-4,75000

(f) 1e-5,75000

(g) 1e-4,375000

(h) 1e-5,375000

Figure 2.10: MEM_VIS reconstructions for a 10″ by 20″ Gaussian source using detectors 5, 6 and 7. Each image has its associated `lnorm` and SIM_PHOTONS_PER_COLL value printed below it. All figures in this section are 64 x 64 pixel images with 4″ x4″ pixels, giving 256″ by 256″ images.

## 2.3 RHESSI flare spectroscopy

The superb energy resolution (1keV FWHM up to 100keV) allows highly detailed study of narrow spectral features of the flares observed with RHESSI. One such feature of great interest is a break in the non-thermal bremsstrahlung power law around 50keV observed in some flares: a so called hard X-ray 'knee'. These features allow us to probe the underlying electron energy distribution in the flare as the electron spectrum is a direct inversion of the photon spectrum (Brown 1971). The sharp feature in the photon spectrum corresponds to a sharp feature in the electron spectrum and so RHESSI's high energy resolution, $\Delta E = 1$keV in the observered range, can reveal just how wide these knee features are.

### 2.3.1 RHESSI Observations

The photon spectra of four flares observed by RHESSI are presented to illustrate this 'knee' phenomenon. Each exhibits a deviation from a single power law in the chosen energy range 10-100 keV, so chosen to allow maximum energy resolution of 1 keV FWHM to investigate the width of the region or 'knee' where this break occurs. To avoid any modulation of the spectra from the imaging grids the time interval for the spectrum over the flare peak was chosen to be 10 full rotations of the RHESSI spacecraft as given at the time of each observation. All spectra were obtained using the SSWIDL suite of software, used for RHESSI and other solar observatories. All spectra were background subtracted and processed using the SPEX package in the RHESSI suite. This included the fitting of the spectra. Each spectrum was fitted using a thermal bremsstrahlung fit for the lower energy portion below 20keV and a broken power-law fit to the remaining portion of the spectrum. The fitting parameters for all the flares are shown in Table 2.3.1, along with the date and time of the event and the flares GOES class. This classification is based on flares peak flux in the range 0.1-0.8nm, soft (< a few keV) X-rays, as shown in Table 2.9

The letter is followed by a number which represents the actual peak flux, for example an X7 flare is a flare with flux peaking at $7 \times 10^{-4}\text{Wm}^{-2}$.

Table 2.9: GOES X-ray Flare Classification

| Classification | Peak Flux in the range 0.1nm - 0.8nm ($\text{Wm}^{-2}$) |
|---|---|
| B | $10^{-7}$ |
| C | $10^{-6}$ |
| M | $10^{-5}$ |
| X | $10^{-4}$ |

The emission measure and plasma temperature are from the thermal bremsstrahlung component of the fit. The emission measure is the number of emitting electrons per $\text{cm}^{-3}$. These two parameters describe the distribution of photon energy. The higher the plasma temperature the higher the mean energy of the emitting electrons, this leads to an increase in the energy of the emitted spectrum, shifting the thermal bremsstrahlung emission to higher energies. An increase in the emission measure leads to an increase in the intensity of emitted photons at a given energy, the photon spectrum would be shifted up if the emission measure increased. The $\gamma$ parameters are the power law indices above ($\gamma_1$) and below ($\gamma_2$) the 'knee' and the difference between the two $\gamma$ coefficients. Also included is the energy at the break and its width and the energy at which the background photon flux is at half and a tenth of the flare photon flux.

Figures 2.11 to 2.14 show the fitted spectra for the four flares in Table 2.3.1

| | 20/02/2002 | 20/02/2002 | 17/03/2002 | 06/08/2002 |
|---|---|---|---|---|
| Time Interval (UT) | 0957:33<br>0958:21 | 1105:56<br>1106:35 | 1928:08<br>1928:57 | 1256:24<br>1257:40 |
| GOES CLASS | M4.3 | C7.5 | M4.0 | C7.9 |
| Emission Measure $10^{49}\mathrm{cm}^{-3}$ | N/A | 0.1159 | 0.57 | 0.031 |
| Plasma Temperature (keV) | N/A | 1.568 | 1.45 | 1.56 |
| Knee Photon flux $\mathrm{s}^{-1}\mathrm{cm}^{-2}\mathrm{keV}^{-1}$ | 0.52 | 0.48 | 2.7 | 0.83 |
| $\gamma_1$ | 7.4 | 3.5 | 3.5 | 3.6 |
| Knee Energy (keV) | 37 | 49 | 44 | 36 |
| $\gamma_2$ | 3.9 | 4.2 | 4.3 | 4.3 |
| $\Delta\gamma$ | -3.5 | 0.7 | 0.8 | 0.7 |
| $\Delta\epsilon$ (keV) | 3 | 4 | 1.8 | 12 |
| Flare= Background/2 (keV) | 57 | 79 | $> 100$ | 66 |
| Flare= Background/10 (keV) | 45 | 52 | 81 | 47 |

Table 2.10: Fitting Parameters and measurements for flares displaying knees.

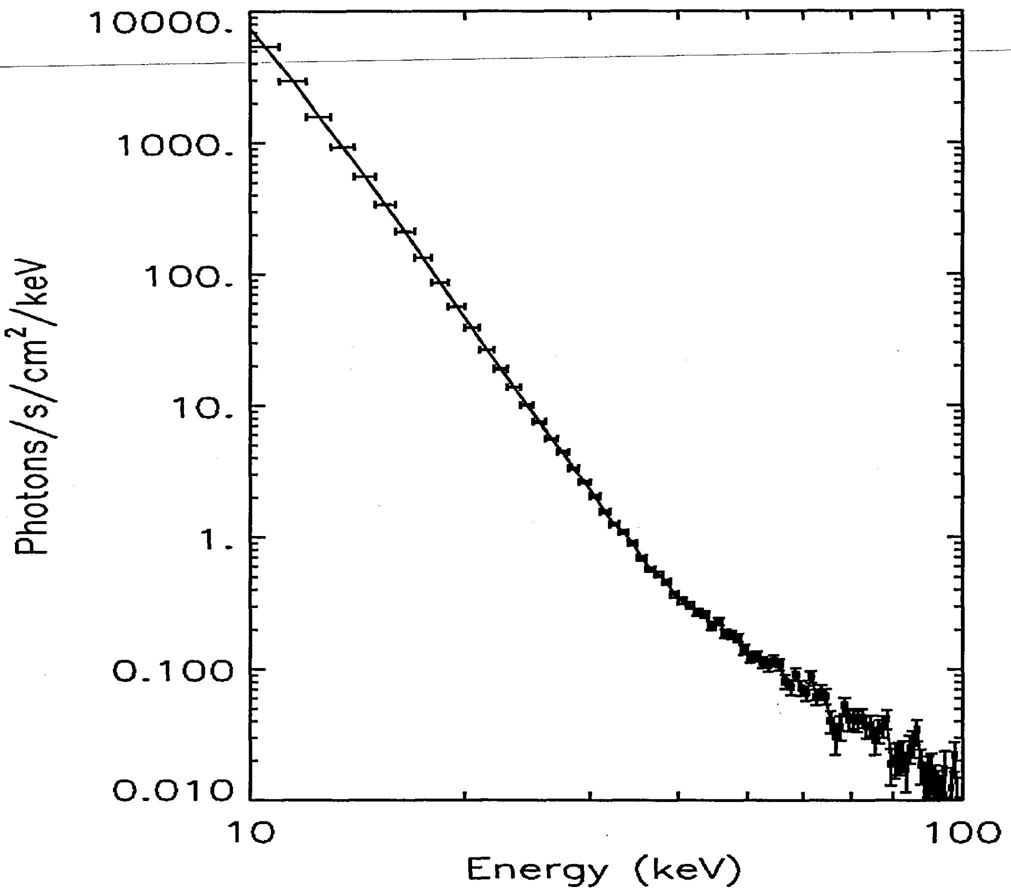

Figure 2.11: Photon spectrum of the 20th February 2002 0958UT M4.3 flare

*M4.3 Flare on 20th February 2002, 0958UT*

This flare's spectrum is unique in the sample: not only is there no thermal component above 10keV but $\gamma_1$ is the steepest observed at 7.4. The other surprise with this flare is that the spectrum actually hardens above the knee energy. It has a negative $\Delta\gamma$. This hardening could be due to under subtraction of the background since the initial steepness of the lower energy power law means that although it is the largest of the flares and has the highest in initial flux, the background becomes appreciably significant at higher energies (see table 2.3.1 the background flux is equal to half the flare flux at 57 keV) compared to the other flares. The background was found to have a $\gamma$ of around 4.2, harder than the $\gamma_2$ of 3.9 in the fit to the spectrum. Additionally the flaring event itself allowed very good intervals for background sampling both before and after the event itself, leaving us confident that a correct and accurate background subtraction had been performed. A further test was performed to verify that the knee was not an artifact of background subtraction. The background was multiplied by a constant factor and subtracted from the observed photon spectrum. The test revealed that if we kept the variation at higher energies to within the noise, the variation that looks like absorption features is actually an artifact in the background. The greater background subtraction could not remove the knee. Another possibility that was ruled out was that pulse pile up may have resulted in this upward knee. This is where two low energy photons arrive at the same time and are mistaken for a single photon with higher energy, this is not the case for this flare (Conway 2002), since when the pulse pile-up correction was applied to the data no discernable difference could be found for the fit parameters. The knee is a real property of the flare.

*C7.5 Flare on 20th February 2002, 1106UT*

The fitting parameters of this flare show that the emission is dominated by a thermal bremsstrahlung component (plasma temperature of approximately 20MK) softening to a powerlaw of $\gamma_1$=3.5 at approximately 20keV before softening further above the knee at 49keV to 4.2. This flare caused some problems with background subtraction since the RHESSI spacecraft brushed the South Atlantic Anomaly before the event. The SAA is a geocoronal anomaly that increases the flux at higher energies (above approximately 30keV). This has to be accounted for in the background subtraction as it seemed to give a decreasing background at the peak of the flare. The pre-event interval for background subtraction was chosen to include this brush so that the interpolation between pre and post event intervals could correct for this. Tests of background subtraction similar to those used for the 0958 flare were performed and the subtraction was found to be accurate.

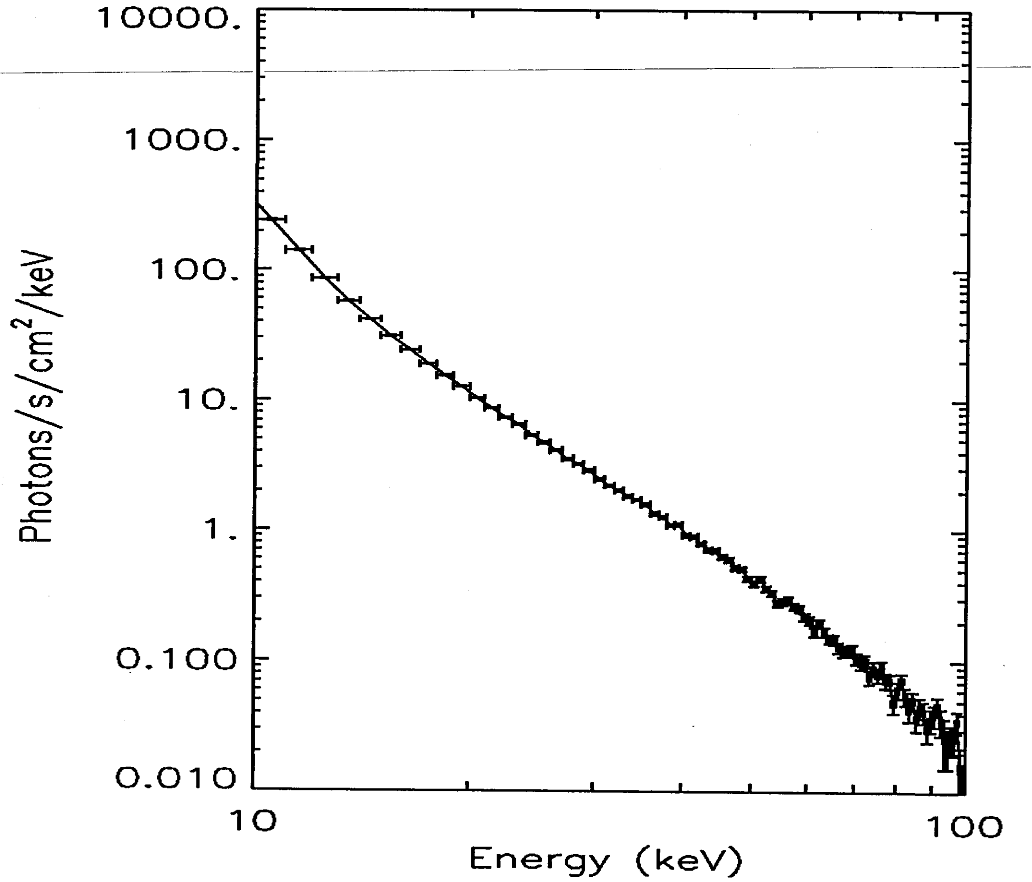

Figure 2.12: Photon spectrum of the 20th February 2002 1106UT C7.5 flare

*M4.0 Flare on 17th March 2002, 1928UT*

Similar in GOES class to the 20th February 0958 flare, this flare exhibits a higher hard X-ray flux since it has a harder $\gamma_1$ of 3.5, softening to 4.3 at a higher knee energy of 44 keV. The flare is thermally dominated below 20keV with a plasma temperature of 17MK. The flare spectrum has more similarities to the 20th February 1106 flare in terms of fit parameters even though it is a larger flare, suggesting that GOES class cannot be used to find flares with broken powerlaw spectra in the energy range covered in this study.

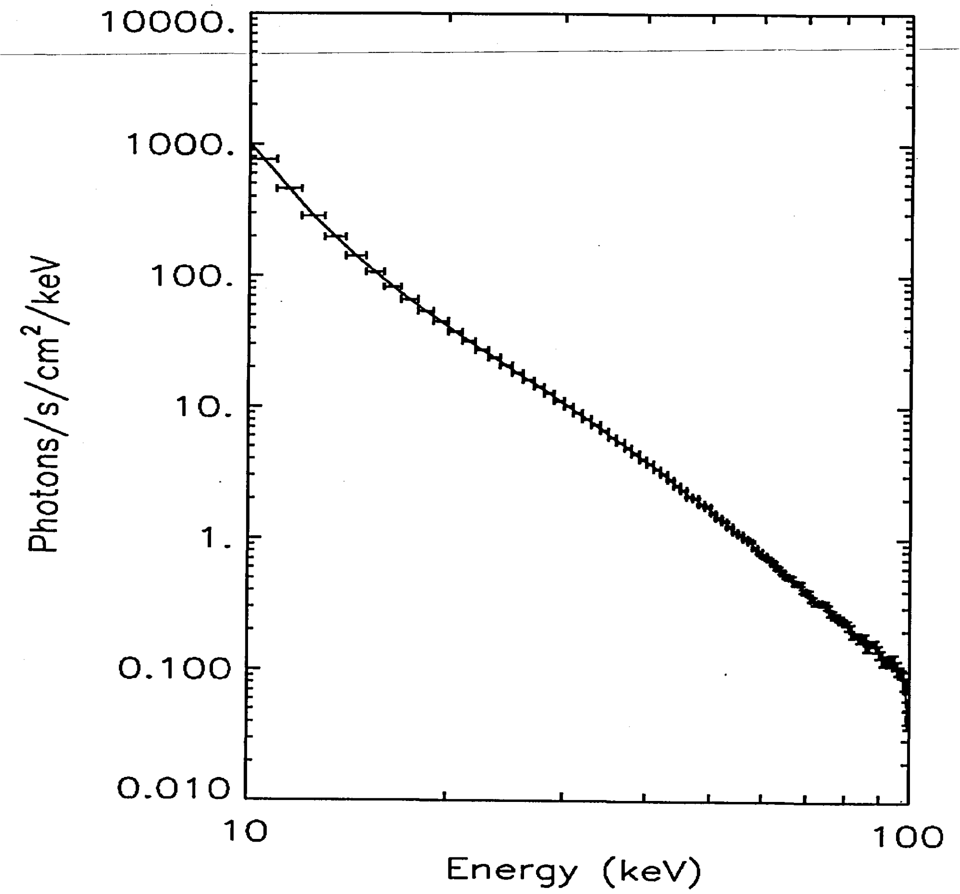

Figure 2.13: Photon spectrum of the 17th March 2002, 1928UT M4.0 flare

*C7.9 Flare on 6th August 2002, 1256UT*

The final flare again is thermally dominated below approximately 20keV with a plasma temperature of 20MK, softening to a $\gamma_1$ of 3.6 below the knee at 36keV, softening again to 4.3 above the knee.

### 2.3.2 Discussion of flare properties

Aside from the first flare in this sample, all the other flares showed several common features: each was thermally dominated below approximately 20keV with a fit corresponding to a plasma temperature of around 1.5 keV or 20MK. The knee energies all fell in a narrow range 30-50keV, the values of $\gamma_1$ and $\gamma_2$ are approximately 3.5 and 4 respectively in each

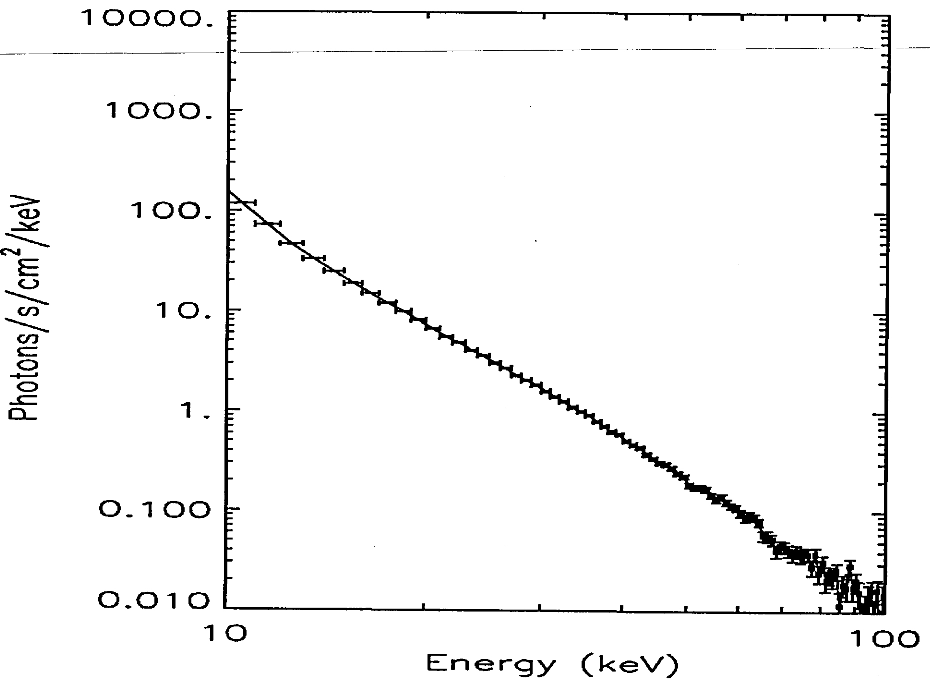

Figure 2.14: Photon spectrum of the 6th August 2002, 1256UT C7.9 flare

case. All these similarities point to similar electron energy distributions existing in the injected electrons in each flaring event.

*The electron spectrum*

So far the chapter has concentrated on form of the photon spectrum. Since the photon spectrum is the integral of the electron spectrum, Section 1.1.1, we can reconstruct the electron spectrum simply by differencing the photon spectrum to reveal the underlying nature of the source electron distribution. Figures 2.15, 2.16, 2.17, and 2.18 show that at higher energies the differenced electron spectrum is noise dominated masking any structure at around the 'knee' energy, although at lower energies the power law distribution is clear. In order to probe the detailed structure of the electron spectrum, we use a MEM algorithm to find the smoothest electron spectrum which can recreate the observed photon spectrum. Assuming Kramer's cross-section (section 1.1.1) we can derive the equations for the electron distribution in the thin and thick target regimes, (Conway et. al. 2003) assuming a generalised photon spectrum, $h(\epsilon)$ of the form,

$$h(\epsilon) = h_* \left(\frac{\epsilon}{\epsilon_*}\right)^{-\gamma(\epsilon)} \tag{2.4}$$

where $\epsilon$ is the photon energy, $\epsilon_*$ is the knee energy. $\gamma(\epsilon)$ is not the same as the spectral index $\gamma_s$ in a log-log plot but is related to it as follows,

$$\gamma = \gamma_s - \frac{\mathrm{d}\gamma}{\mathrm{d}\epsilon} ln \frac{\epsilon}{\epsilon_*} \tag{2.5}$$

For the thin and thick target regimes the energy electron distribution is given as,

$$\frac{\bar{F}(E)}{E} = h(E)\gamma(E)\left[1 + \ln\left(\frac{\epsilon}{\epsilon_*}\right)\frac{d\ln\gamma}{d\ln\epsilon}\right]_{\epsilon=E} \quad \text{(thin target)} \tag{2.6}$$

where $\bar{F}(E)$ is the electron flux spectrum (electrons cm$^{-2}$keV$^{-1}$) over the whole emitting volume, and,

$$F_o(E_o) = \frac{K\bar{n}_p V}{A} H(\epsilon_*) g(E_o) \quad \text{(thick target)} \tag{2.7}$$

where

$$g(E_o) = \left[\frac{\gamma(\gamma+1)}{\epsilon^2} + \frac{2}{\epsilon}\left(\gamma ln\frac{\epsilon}{\epsilon_*} - 1\right)\frac{\mathrm{d}\gamma}{\mathrm{d}\epsilon} + \left(ln\frac{\epsilon}{\epsilon_*}\right)^2 \left(\frac{\mathrm{d}\gamma}{\mathrm{d}\epsilon}\right)^2 - \left(ln\frac{\epsilon}{\epsilon_*}\right)\frac{\mathrm{d}^2\gamma}{\mathrm{d}\epsilon^2}\right]_{\epsilon=E_o},$$

$F_o(E_o)$ is the injected electron spectrum that gives rise to $\bar{F}(E)$, $K = 2\pi e^4\Lambda$ where $\Lambda$ is the coulomb logarithm, $\bar{n_p}$ is the average plasma density in volume $V$ and the electrons are injected over an area $A$.

Numerically solving equations 2.6 and 2.7 to achieve the smoothest electron spectrum for the observed photon spectrum shows that even when smoothed the electron spectrum still has a more complex structure than just a simple broken power law, as suggested in section 1.1.1. The results of this analysis and the simple differencing approach are shown in Figures 2.15, 2.16, 2.17, and 2.18.

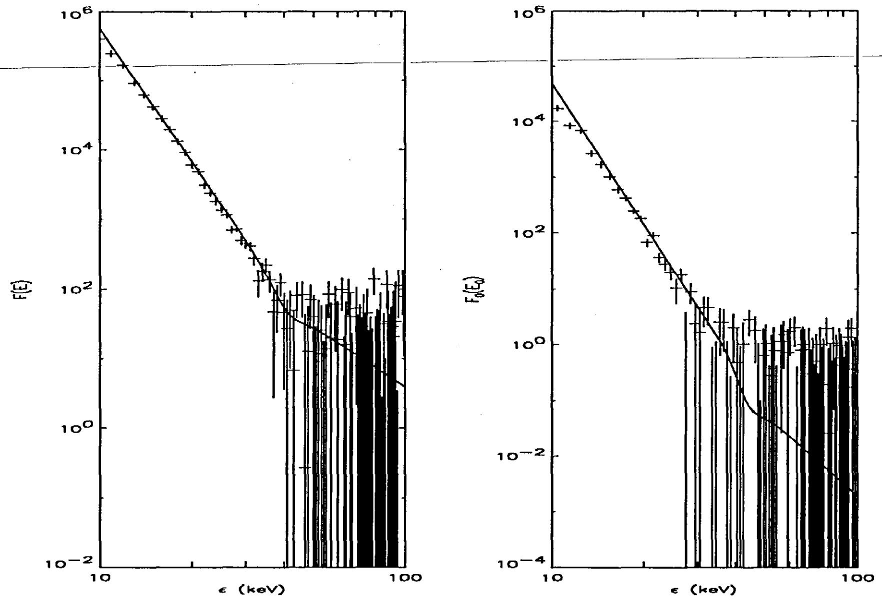

Figure 2.15: Thin target (left) and thick target (right) electron spectra of the 20th February 2002, 0958UT M3.4 flare. The points are the direct derivative of the photon spectrum, the solid line is the smoothest electron spectrum to recreate the observed photon spectrum.

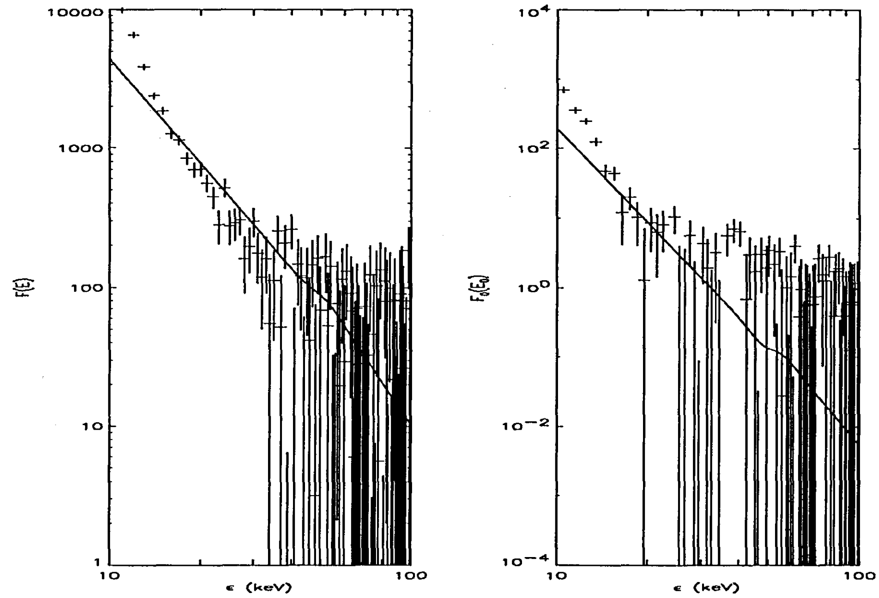

Figure 2.16: Thin target (left) and thick target (right) electron spectra of the 20th February 2002,1106UT C7.5 flare. The points are the direct derivative of the photon spectrum, the solid line is the smoothest electron spectrum to recreate the observed photon spectrum.

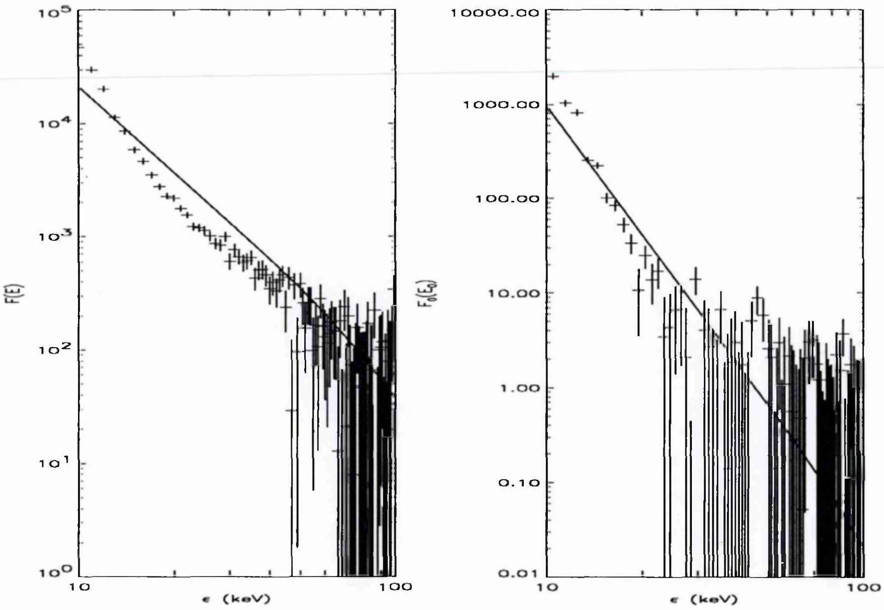

Figure 2.17: Thin target (left) and thick target (right) electron spectra of the 17th March 2002, 1928UT M4.0 flare. The points are the direct derivative of the photon spectrum, the solid line is the smoothest electron spectrum to recreate the observed photon spectrum.

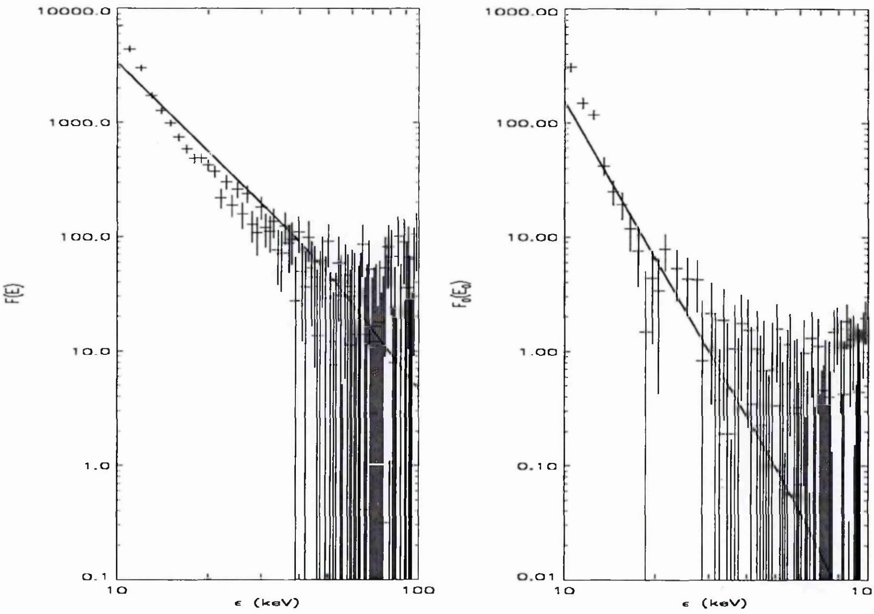

Figure 2.18: Thin target (left) and thick target (right) electron spectra of the 6th August 2002, 1256UT C7.9 flare. The points are the direct derivative of the photon spectrum, the solid line is the smoothest electron spectrum to recreate the observed photon spectrum.

As we can see the electron spectra does follow a broken power law. This is to be expected as its shape is dependent on our theoretical understanding of how the photon spectrum arises. It is also obvious, especially from Figures 2.15, 2.16, that the structure of the electron spectrum around the knee energy is more complex than in the photon spectrum, the curve shows an upward bump before the knee in the first case and a downward bump before the knee in the second. Even with this more complex structure there is no evidence for unphysical behaviour in the electron spectrum for these flares, i.e. no negetivity.

Using this data set Massone et al. (Massone et al. 2003) looking at the inversion problem of flare spectrum to obtain the underlying electron spectra for each flare, and testing the inversion for different collisional cross-sections. They found that the 'knees' did not conflict with our theory for the transportation of electrons during the flaring event, i.e. the knees did not produce any unphysical results, negative values, in the inverted electron spectrum at the knee energies. One point to consider is that a knee feature can be produced even if the injected electron spectrum is a single power law. This is due to emission reflected from lower, denser layers of the atmosphere. The solar albedo can be as high as 40% of the hard X-ray emission depending on the source position and the $\gamma$ of the spectrum. Typically this can produce deviations from the powerlaw at around 30-60keV (Alexander and Brown 2002).

A further use for the observations of 'knee' spectra is as a test of the spectrometer itself, as pointed out in Section 2.3.1. Pulse pile up, although ruled out in this case, can cause deviation from a powerlaw. This means that if a knee is seen, particularly in larger, brighter flares we can begin to analyse the effect of pulse pile up in the spectrograph (Kontar et al 2003).

## 2.4 Summary

We have seen just how potent a tool RHESSI is for studying solar flares, and the dangers to be aware of when interpreting the images the analysis software produces. The work presented in Section 2.3 shows that the mission is successful in increasing our detailed understanding of electron transport in flares and reveals the underlying nature of the initial electron population. From the results in Section 2.3.2 and those of Massone, we can be confident in our current understanding of cross-section as a stable platform from which to build our understanding.

# Chapter 3

# Optical Spectroscopy: Reduction of SAAO and WHT spectra

In the following Chapters, 4 and 5, we present optical spectroscopy of flare star candidates and a possible microquasar. In this chapter we will outline the general techniques used to reduce spectroscopic data and to present it in such a way as to be appropriate to the tasks performed on the data.

## 3.1 Calibration Frames

In addition to obtaining spectroscopy of a target object when at a telescope, calibration frames are required for the reduction of the data. The frames needed are as follows:

- Bias frames - zero exposure time exposures of the unilluminated CCD, necessary to account for the bias level across the chip which is introduced to prevent noise variations from causing a negative value in any pixel.
- Dome Flats - exposures of a white lamp uniformly illuminating a section of the telescope dome. Taken at the start or end of each night, these exposures are necessary to account for any pixel to pixel variation in the wavelength response over the CCD.

- Sky Flats - exposures of the twilight sky. Taken each night just after sunset, these are needed to remove any large scale illumination variation, from the slit, along the spatial axis (perpendicular to the dispersion axis) of the CCD from the image. The slit field-of-view for SAAO 1.9m was approximately 3′ along the spatial axis, measured from images with two stellar spectra of known angular separation. This was not possible with the WHT spectra. Over the two sets of observations both the dome and the sky appear uniform, i.e. no large scale variation along the spatial axis in either. Therefore it is not necessary to use one to correct the other. Only the variation due to pixel-to-pixel changes and illumination of the CCD are present in the respective calibration frames. The sky flats were still used to correct for the illumination of the CCD.

- Darks - a combination of short and long exposures taken with no illumination of the CCD. These are needed to remove dark currents, ie. charge that accumulates on the CCD due to the trapping of thermal electrons.

- Arc spectra - exposures of CuAr lamp for wavelength calibration. These are taken at the start and finish of each set of exposures, or every 10 to 20 minutes which ever is shortest, and for each object change. This frequency of observation is necessary to account for any movement or flexure in the telescope assembly which could cause the dispersion coefficient to change throughout the night and so varying the wavelength calibration.

All reduction of SAAO and WHT spectroscopy was performed using standard IRAF routines. The WHT spectra were obtained in service mode unlike the SAAO spectra, but the same calibration frames were present in each case.

## 3.2 Bias Subtraction

The first step in the reduction of CCD data, be it spectroscopic or photometric, is to establish two things, the region on the CCD that contains useful data, and the underlying noise or 'bias' of the CCD. The bias arises from the small voltage that is applied over the CCD, at all times, to prevent negative signal on readout. Upon close inspection, the overscan region at the edge of the CCD shows a sharp cut off between bias level and data, there was no evidence of charge leakage in the SAAO dome flats. Figure 3.1 shows a typical dome flat from the SAAO run; the trim and overscan sections are displayed. The trim section, is chosen at the time of reduction to contain only meaningful data. The overscan region is user defined for the purpose of frame-by-frame bias subtraction from the science frames.

The same was not the case in the WHT spectra, Figure 3.2, where the cut-off was at pixel 88, but the drop off in data below pixel 487 and above pixel 4615 was so close to the bias level that it was discarded.

The first run through IRAF's CCDPROC was performed with the TRIMSEC and BIASSEC parameters turned on and set to [50:1773,40:114] and [1:22,1:133] respectively in the SAAO images. At this stage we have accounted for any exposure-to-exposure or temporal variation in the mean bias level. Although the dome flat contains information below column 50, the data in the object spectrum drops off steeply below column 50 and so this was trimmed off in all images from the SAAO run.

For the WHT spectra the parameters TRIMSEC and BIASSEC were set to [487:3138,1:151] and [1:88,1:151], the full width (columns) of the CCD was used since there was no sudden drop off of data at the edges.

This produced a trimmed image that has the mean bias level from the overscan region subtracted. This first-order bias correction was done for all images, including other

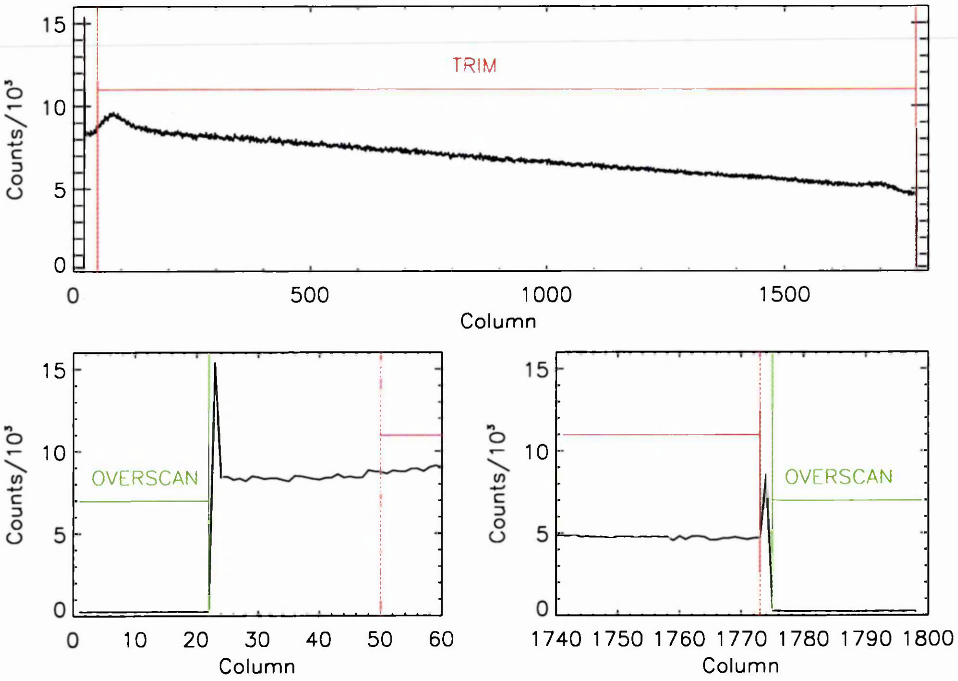

Figure 3.1: Top panel shows a slice along the dispersion axis for an example dome flat from SAAO, the lower two panels are close ups of either end of the flat showing trim sections and the overscan region.

calibration frames. For the SITe CCD (SAAO) this level was found to be of the order 250 counts/pixel. For the MARCONI CCD used on ISIS (WHT) the mean bias level was found to be 600 counts/pixel.

Any spatial variation in the bias level is next removed using the bias exposures (zero exposure time images, so only signal due to the small voltage is read out). All the bias frames from the run were combined and averaged to form a master zero flat, this correction was then applied to all images through CCDPROC.

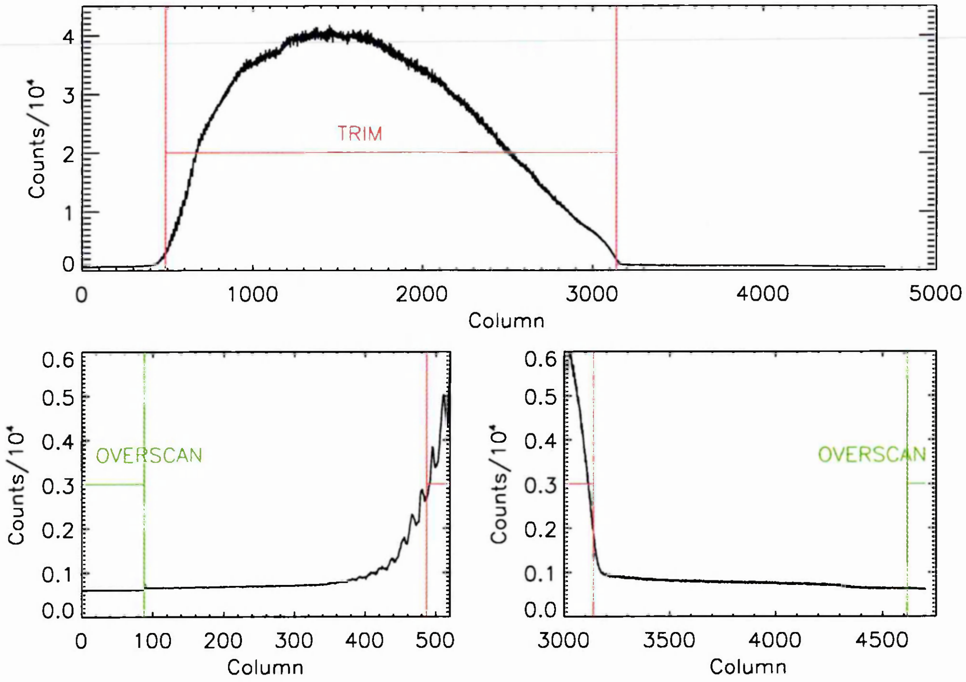

Figure 3.2: Top panel shows a slice along the dispersion axis for an example dome flat from WHT, the lower two panels are close ups of either end of the flat showing trim sections and the overscan region.

## 3.3 Flat Field Correction

The images also need to be corrected for additional instrumental effects such as unequal illumination of the CCD by the optics and pixel-to-pixel variation in sensitivity. As can be seen in Figure 3.1 and especially in Figure 3.2 the response across the CCD is not constant. To correct for this, the images needed to be flat-fielded. There are two steps to this process.

### 3.3.1 Pixel-to-Pixel Variation

Firstly the Dome Flats were combined to produce a high signal flat to correct for the pixel to pixel variation across the CCD. At this stage the dome flats from night 3 (19th/20th

June) of the SAAO run were discarded as an additional illumination source had been present, changing the structure seen in all the other dome flats. It was noted that the structure in the trimmed Dome flat at the start and end is not present in the Twilight Flats or the target exposures, so this structure had to be removed before applying the master flat to the data. This was done by fitting the master flat with a third order cubic spline, along the dispersion axis, in the IRAF procedure RESPONSE which output an image that was the ratio of the fit to the flat. CCDPROC was then run again, but this time using the normalised flat.

### 3.3.2 Illumination Correction

The final task in the image reduction was to check the flattened twilight flats for variations in the illumination of the chip. Taking cuts along the spatial axis (perpendicular to the dispersion axis), in the SAAO data there was a gradient of 3% from the bottom of the chip to the top, due to non-uniform illumination of the CCD. In the case of the WHT data the gradient was 4% To correct for this, a master twilight flat was produced, using the same method as for the master Dome flat. The combined flat was then fitted with a function along the spatial axis, for several intervals along the dispersion axis, using the ILLUM routine. The final run through CCDPROC caused the inclusion of the illumination correction to the images.

## 3.4 Extraction of Spectra

After the images had been trimmed, flattened and illumination corrected, the spectrum itself must be extracted from the CCD image. This extraction was performed using the APALL routine, in IRAF. The APALL routine is an all in one spectral extraction routine, it locates the object spectra or spectrum, if more than one, on the image and smoothly traces its position across the image. Performs an optimal extraction (optional) of the spectra and in doing so also removes the sky background and cosmic ray hits on the object. More detail of this follows. Firstly the position of the aperture on the image needs to be established. This was done by taking a cross section in the spatial axis from an object exposure. The aperture position and background regions are shown in Figure 3.3 for the SAAO data, the WHT data has a very similar profile. The spectrum will not necessarily be parallel to the long axis of the CCD and so the aperture must be traced along the CCD, and fitted with a function for extraction, this is done interactively where the position of the apertures, along the image, found by APALL is fitted with a smooth polynomial. The spectrum was then extracted along this fit, at each point of the fit the total counts in the aperture window (± approximately 5 pixels from center of aperture) have the sky/background subtracted ( mean of -20:-6 and 6:20 pixels from the centre of aperture window) and the extracted spectrum was then output to a file. The same was true for both the SAAO and WHT data sets, although the best fit to the aperture trace was a third order cubic spline for the SAAO data and a third order Legendre function for the WHT data. The extraction of the spectra was performed using inverse variance weighted fitting of the spatial profile, this is based on the algorithm outlined by Horne (1986). This weighting means that the edges of the spatial profile, where there is little signal, are given relatively little weight. Using this method, we can simultaneously remove cosmic ray hits and bad pixels from the object spectra and see an increase in the signal-to-noise ratio of the data since the extraction is performed such that the variance on the extracted spectra is minimised.

## 3.5 Wavelength Calibration

In spectroscopy it is necessary to know the wavelength corresponding to each feature in our spectrum. To calibrate the spectra to a wavelength scale, arc exposures were taken

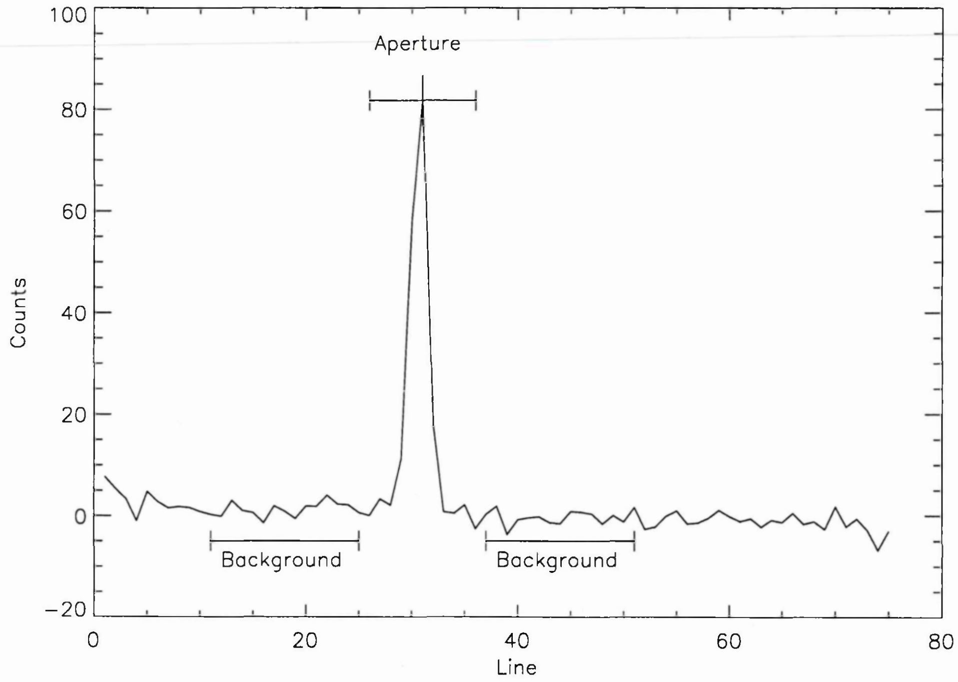

Figure 3.3: Sample cross section across the CCD, perpendicular to the dispersion axis, of a single object exposure from the SAAO run, mean of columns 857-886 for the purpose of aperture and background region identification.

of a CuAr lamp for SAAO and a combination CuAr+CuNe lamps for the WHT. For the arcs the spectral features were identified from reference spectra of the CuAr lamp and the CuAr+CuNe lamp, this then gave the wavelength range and the dispersion of the spectrum. The next step was to extract the arc spectra using the same aperture trace as the object spectra it is associated with, using APALL and using the aperture obtained for the object spectra. Since each arc is associated with multiple object exposures, taken both before and after, this was repeated for each object exposure for both 'before' and 'after' arc exposures. Using the REIDENTIFY routine the features in the remaining arc spectra were matched to the features in the reference arc spectrum, then each arc spectrum has a starting wavelength and a dispersion coefficient (Å per pixel). The extracted 'before' and 'after' arcs were assigned to the object spectra and weighted on the basis of observation time. The routine DISPCOR was used to dispersion correct the object spectra to the wavelength scale.

## 3.6 Normalisation of Object Spectra

One useful method to employ in the data reduction is to normalise the spectra. This was simply achieved by fitting a function to the continuum of the source spectra and dividing by the fit to produce a spectrum normalised to one. In the case of 1RXS J 162848.1-415241 observed in the SAAO run, a third order cubic spline fit was sufficient to fit the broad features of the continuum. This allows non-flux calibrated spectra to be compared directly. With the WHT data it was not necessary to normalise the spectra since flux calibration could be performed on all target spectra. Additionally the nature of the target objects, M-type stars, meant that the spectra were dominated by broad absorption features and fitting the continuum would have been non-trivial for very little return.

## 3.7 Flux Calibration

Flux calibrating the spectra requires observations of a well observed spectro-photometric standard star, normally of early spectral type or a white dwarf, due to the lack of absorption lines in their spectra. The observed standard is compared to a flux calibrated spectrum of itself, yielding a wavelength dependant sensitivity function for the CCD. This function is then applied to the target observations to provide flux data on the object. In the case of 1RXS J 162848.1-415241 the standard used was the G0 star CD-44 12736. Since it was only observed on one night of the run the sensitivity function is not valid for the whole run as the wavelength response of the CCD changed over time, as well as 1RXS J 162848.1-415241 moving off the slit giving red or blue excesses. This was not an issue as the normalised spectra, see section 3.6, were used exclusively in the analysis of 1RXS J 162848.1-415241. The WHT spectra on the other hand was successfully flux normalised using the standard O5 star HD217086.

# Chapter 4

# Identification of X-ray and Optical Flaring Events

In the following Sections 4.1 and 4.2 we shall look at the detection of flaring events in the X-ray and the optical. In Section 4.1 we shall present a study of a serendipitously observed flare during a survey of M31, and deduce the spectral type of the object and the luminosities of its flares. In Section 4.2 we find three objects observed during a V-band photometric survey looking for variability, and through follow up spectroscopy deduce the nature of two of the objects as typical M dwarf flare stars with thw third object being of earlier spectral type K.

## 4.1 Serendipitous X-ray Observations of a Flare Star with *XMM*

Whilst performing a survey (Barnard et al 2003) of the nearby Andromeda galaxy, M31, the ESA X-ray telescope *XMM-Newton* detected faint X-ray emission from a source at RA=00 42 36.5, $\delta$=41 13 50 near the centre of Andromeda's core. This object showed flaring in two of the four observations currently available. In earlier *Chandra* observations of the central region of M31 (Kong et. al. 2002.) this object was identified with a foreground star Ha94(238126) and was not associated with M31. It will now be referred to by its X-ray designation J004236.5+411350.

### 4.1.1 *XMM* Results

Of the four observations of the core of M31 (Barnard et al 2003) given in Table 4.1, J004236.5+411350 was only detected in observation 2 (27 December 2000) and observation 3 (29 June 2001). This is due to the source only being above the detection limit if it flares during the observation. Lightcurves were extracted for both these observations from all three EPIC instruments on board XMM; MOS1, MOS2, and PN CCD detectors. All three detectors lie at the base of individual grazing incidence X-ray telescopes. The MOS cameras are made up of 22 Metal Oxide Semi-conductor CCDs and are identical to each other. These lie behind the grating for the Reflection Grating Spectrometers, RGS, and as such receive only 44% of the incident X-rays each. The PN camera is made up of 12 pn-CCD's, its telescope has an uninterrupted beam. The extraction region for each detector in each observation was 20″, which gives us 70% of the photons from the source, and due to the density of the sources in the field this is the largest region we can use. All backgrounds for the lightcurves were extracted from a 20″ region in an area of the same chip that was free from point sources (see Figure 4.1 where the source region is shown in green, and the background region is shown in cyan). Since, for photometric observations the information from each of the detectors can be summed, this was done to improve the signal-to-noise ratio of the data. The data were binned into 100s bins and the resulting summed lightcurves are shown in Figure 4.2.

In each of the lightcurves we see a fast rise to the peak with a longer decay time, typical of stellar flares (of the order hours) and reminiscent of solar flares (of the order seconds to minutes).

Table 4.1: *XMM* Observations of the Core of M31

| Observation | Date | Duration |
|---|---|---|
| 1 | 25 July 2000 | 34ks |
| 2 | 27 December 2000 | 13ks |
| 3 | 29 June 2001 | 56ks |
| 4 | 6 January 2002 | 61ks |

We obtained X-ray spectra for each of the flares for PN, and both MOS 1 and 2. The extraction regions are shown in green in Figure 4.1. In both observations a region of 40″ (white region) was used to extract the background spectra to improve the signal to noise rates. The MOS spectra in each observation were combined to increase the number of counts. The spectra were analysed using the standard software package *XSPEC* (http://heasarc.gsfc.nasa.gov/docs/xanadu/xspec/ also Dorman et. al 2001). In the PN detector we had 365 and 175 source counts in observation 2 and 3 respectively, and for the combined MOS detectors we had 325 and 138 counts. To fit the spectra the energy channels were grouped in the range 0.3 to 10 keV with variable bin sizes such that we had at least 10 counts per bin.

A thermal bremsstrahlung model would be most appropriate for the fitting model but in this low count regime it could not tell us more than a simple power law will. That being the case the binned spectra in the range 0.3 to 10keV were fitted using a simple power law model with photoelectric absorption. This absorption is parametised by the hydrogen column density in the line of sight. The hydrogen itself is not responsible for the absorption of soft X-rays, the column density of hydrogen is directly related to the column density of the heavier elements. These heavy elements are absorbing the X-ray photons in their inner electron shells as outlined in Morrison et al (1983). Without accounting

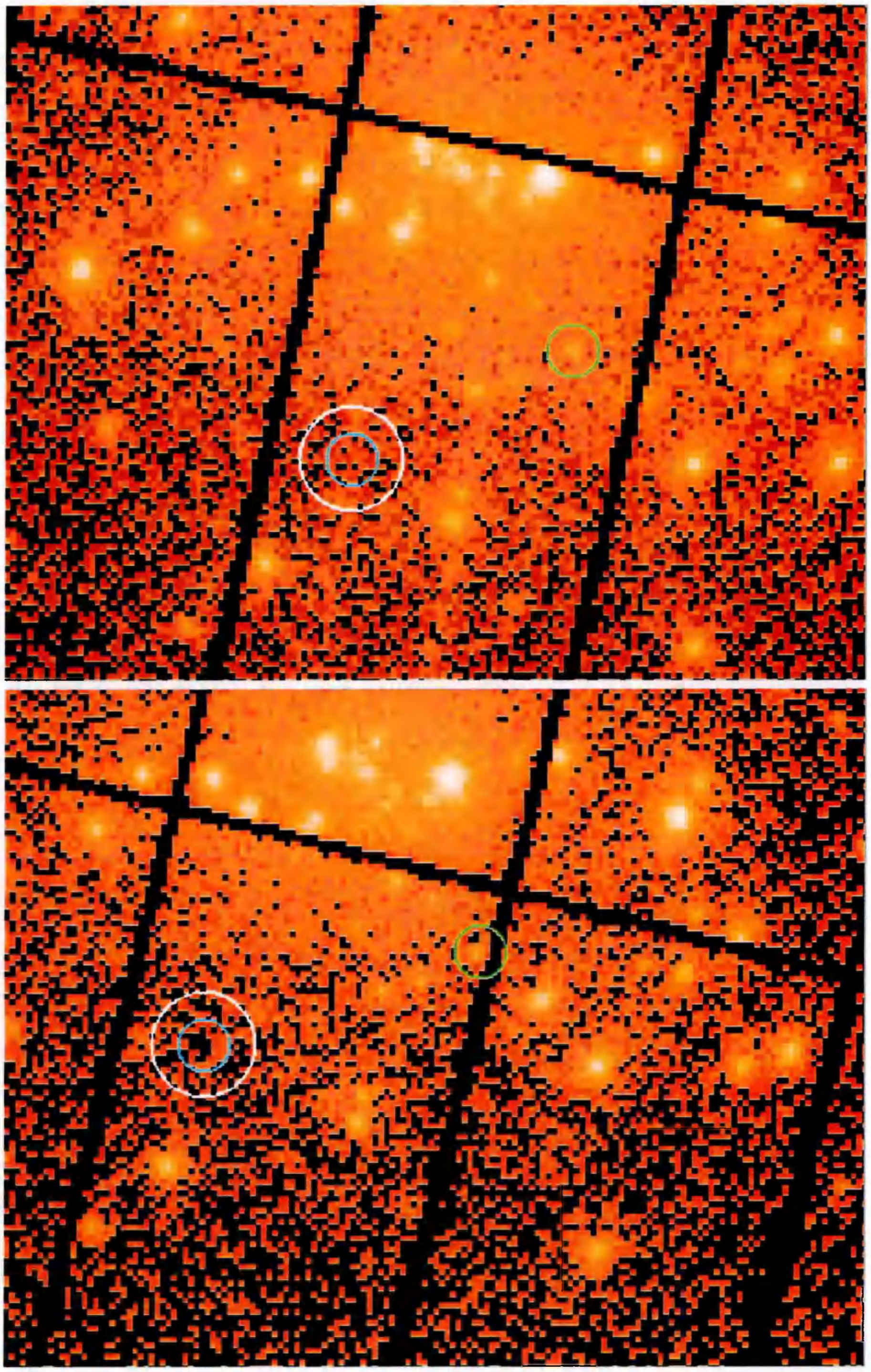

Figure 4.1: PN images for observation 2 (top panel) and observation 3 (bottom panel). The extraction regions are shown, green: source lightcurve and spectrum, cyan: background rate, and white: background spectrum.

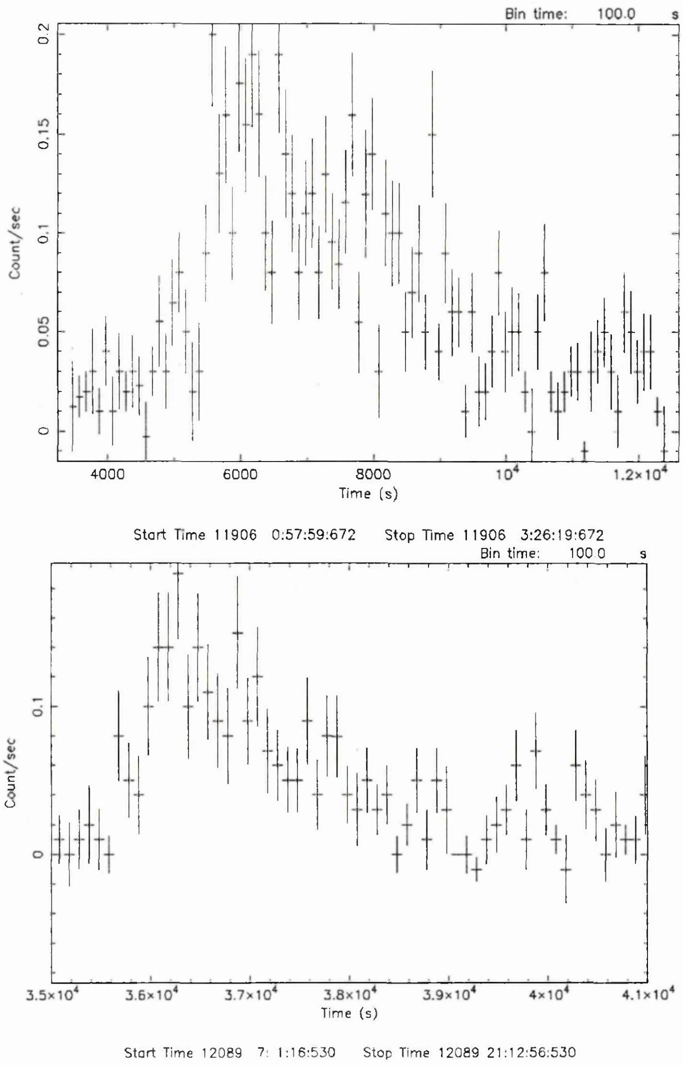

Figure 4.2: Total flare lightcurves from the sum of the outputs from MOS1, MOS2 and PN for observation 2 (top panel) and observation 3 (bottom panel) each binned to 100s. The flare dominates the whole of observation 2 and in observation 3 the flare is seen between 35 and 41ks.

for the absorption the low energy photons from the source would be underestimated in the final fit, as line of sight absorption preferentially affects the lower energy end of the spectrum. The absorption was fixed at the value given in Predehl and Schmitt (1995), nH=$6.4\times10^{20}$cm$^{-2}$ in the direction of M31. This is an upper limit, as it is the total column density to M31, whilst our object is a foreground star, section 4.1.4 . It is used since we cannot obtain an accurate absorption measure from our X-ray data. The fitted source spectra are shown in Figures 4.3 and 4.4 and the fitted parameters are shown in Table 4.2 for both observation 2 and observation 3 with the 90% confidence limits for the parameters. Also in Table 4.2 are the calculated fluxes from the model parameters.

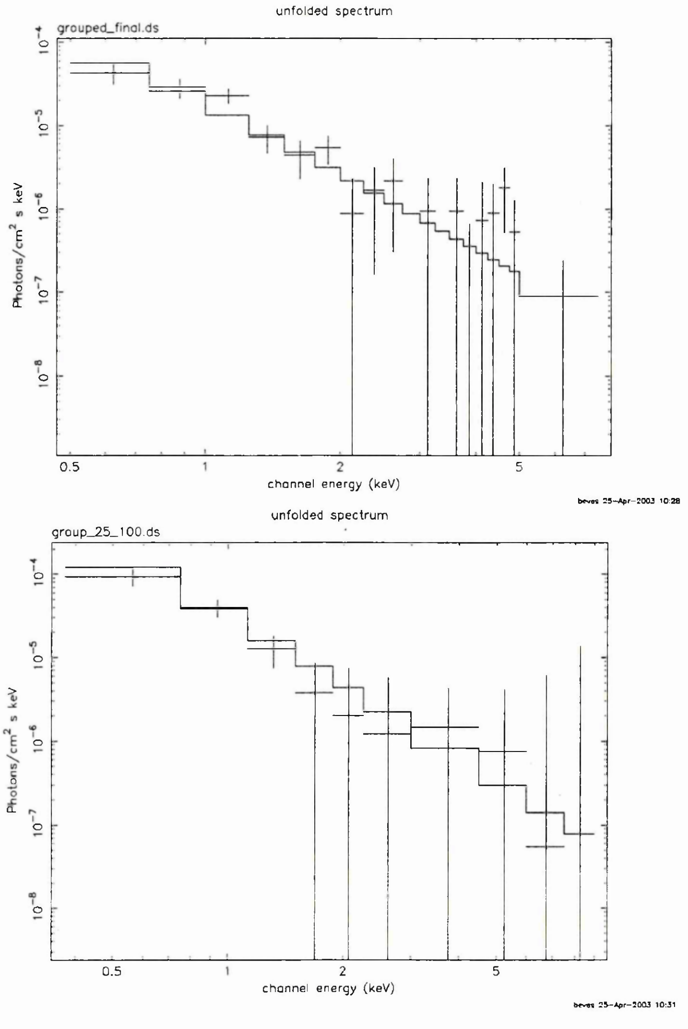

Figure 4.3: Source spectra of the flares from observation 2, PN on top, combined MOS underneath. Note that for observation 2, the full 13ks interval was used.

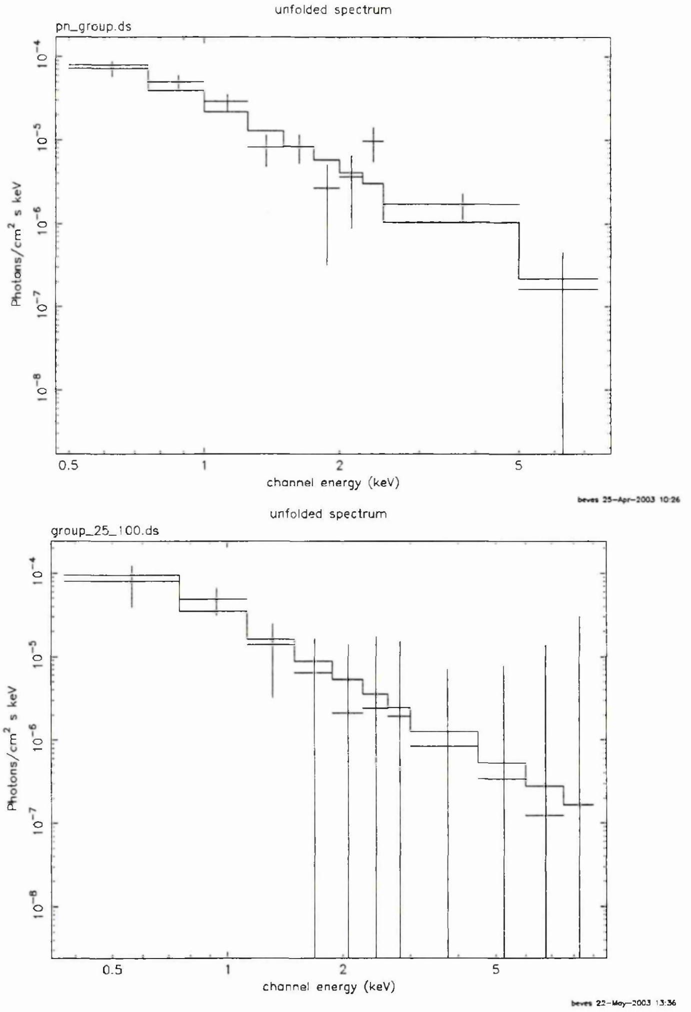

Figure 4.4: Source spectra of the flares, showing the fitted model (solid line), from observation 3, PN on top, combined MOS underneath. Note that for observation 3 only the range 35 to 41 ks after start of observation was used.

*Plasma Temperature and Emission Measure*

Although a simple power law was used to find the flux of J004236.5+411350, a thermal bremsstrahlung model was also fitted to the data to obtain estimates for the emission measure and the plasma temperature of the flares. The values obtained are shown in Table 4.3, the flux obtained from this model was in agreement with that of the simple power law fit, within its errors. Only the PN data was used as this provides the highest

Table 4.2: Fitting parameters for the spectra shown in Figure 1.3 including 90% confidence errors. The normalization and photon index were left free to vary, whilst the value of nH was fixed, see text.

| **Observation 2** | **PN** | **MOS** |
|---|---|---|
| nH ($10^{20}$) | $6.4 \pm 0.1$ | $6.4 \pm 0.1$ |
| Photon Index | $3.0\pm 0.4$ | $2.9 \pm 0.8$ |
| Normalization Photon $\mathrm{keV}^{-1}\mathrm{cm}^{-2}$ at 1keV | $(2.2\pm 0.4)\times10^{-5}$ | $(3.7\pm 1.1)\times10^{-5}$ |
| Flux ($\mathrm{erg\,s}^{-1}\mathrm{cm}^{-2}$) | $(5.8 \pm1.3)\times10^{-14}$ | $(5.6\pm2.3)\times10^{-14}$ |

| **Observation 3** | **PN** | **MOS** |
|---|---|---|
| nH ($10^{20}$) | $6.4 \pm 0.1$ | $6.4 \pm 0.1$ |
| Photon Index | $2.8 \pm 0.40$ | $2.5 \pm 1.2$ |
| Normalization Photon $\mathrm{keV}^{-1}\mathrm{cm}^{-2}$ at 1keV | $(3.4\pm 0.6)\times10^{-5}$ | $(3.4\pm 1.7)\times10^{-5}$ |
| Flux ($\mathrm{erg\,s}^{-1}\mathrm{cm}^{-2}$) | $(9.6 \pm2.2)\times10^{-14}$ | $(5.9 \pm4.1)\times10^{-14}$ |

signal-to-noise spectra.

Table 4.3: Estimates for the emission measure and plasma temperature of the flares on J004236.5+411350. From the PN detector only.

| | **Observation 2** | **Observation 3** |
|---|---|---|
| Emission Measure ($10^{51}$cm$^{-3}$) | 27± 3.5 | 86±3.1 |
| Plasma Temperature (keV) | 0.73±0.26 | 0.77±0.43 |

The fitting parameters were then plotted against existing data for comparison shown in Figure 4.5. The two observed flares appear to lie within the distribution of other stellar flares and the data suggest two distinct populations at lower temperatures. The solar flares have consistently smaller emission measures at a given temperature than that of stellar flares.

### 4.1.2 Optical Counterpart and Extinction

Kong et al (2002), identified J004236.5+411350 with the optical counterpart Ha94(238126) (Haiman et al. 1994) in the extension to Magnier et al. (1993), M31 new OB associations, catalogue. The photometric data for the source were obtained from this catalogue and are shown in Table 4.4.

The colour index B-V indicates an MK spectral type M, as would be expected since the majority of flare stars tend to be late type dwarf red stars of type K and M (Agrawal et. al 1986) although some early type stars exhibit flaring as well (Schmitt 1994).

To further constrain the spectral type we take into account the reddening due to interstellar dust.

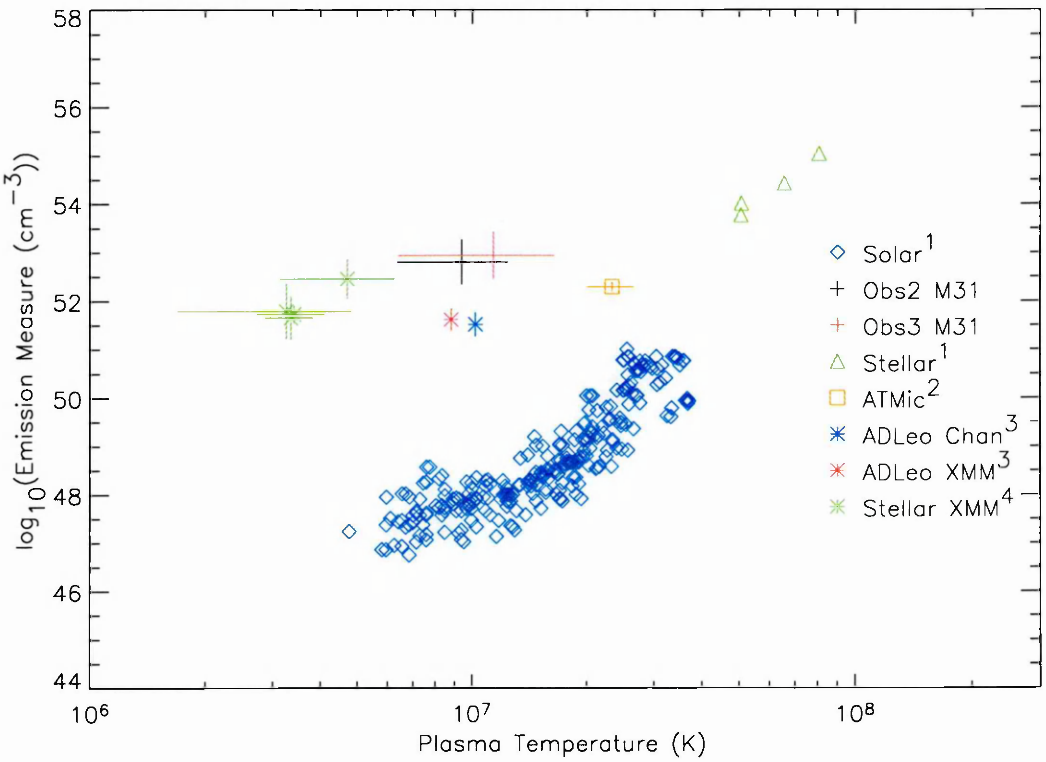

Figure 4.5: Emission measure verses plasma temperature for the two flares observed on J004236.5+411350, Obs2 M31, Obs3 M31, also plotted are data on other flares both solar and stellar as shown in the key. 1. Feldman et al 1995, 2. Raassen et al 2003, 3. van der Besselaar 2003, 4. Robrade et al 2005.

Table 4.4: Optical data for J004236.5+411350 taken from Magnier et al. (1993)

| Band | Magnitude |
|---|---|
| B | 21.395 ±0.243 |
| V | 19.89 ±0.113 |
| R | 18.717 ±0.037 |
| I | 16.828 ±0.102 |

### 4.1.3 Reddening

We used Wegner's (Wegner 1994) value of $R$=3.1±0.1, where $R$ is the reddening, for the ratio of total to selective extinction defined by

$$R = \frac{A_V}{E(B-V)} \tag{4.1}$$

where $A_V$ is the total extinction, in the V band, to source and $E$(B-V) is the colour excess, of the source, defined as;

$$E(B-V) = (B-V)_{obs} - (B-V)_{intrinsic} \tag{4.2}$$

We also used the relation for the interstellar reddening free parameter Q for BVRI magnitudes and Wegner's reddening law as described in Maxwell (2001)

$$Q = (B-V) - 1.25(R-I) \tag{4.3}$$

Using the above, we calculate the observed values of colour excess for constant Q-value and $A_V = 0 - 6$ for spectral types K and M, and luminosity class V, using the intrinsic colour excess values for each spectral type taken from Johnson (1966). The results of this calculation are given in Figure 4.6. The earlier spectral types would lie together at the left of the plot over K0, and were not plotted for the sake of clarity.

The only colours consistent with those of our target imply that our source is a late type MV star with low reddening. Only two points lie within our error ellipse and these correspond to a star of type M6V and total extinction to the source, $A_V$ = 0 and 0.25 respectively.

### 4.1.4 Distance and Luminosity

We now examine the distance to J004236.5+411350 and hence the luminosities of our flares, adopting our preferred spectral type of M6 and the absorption column density nH

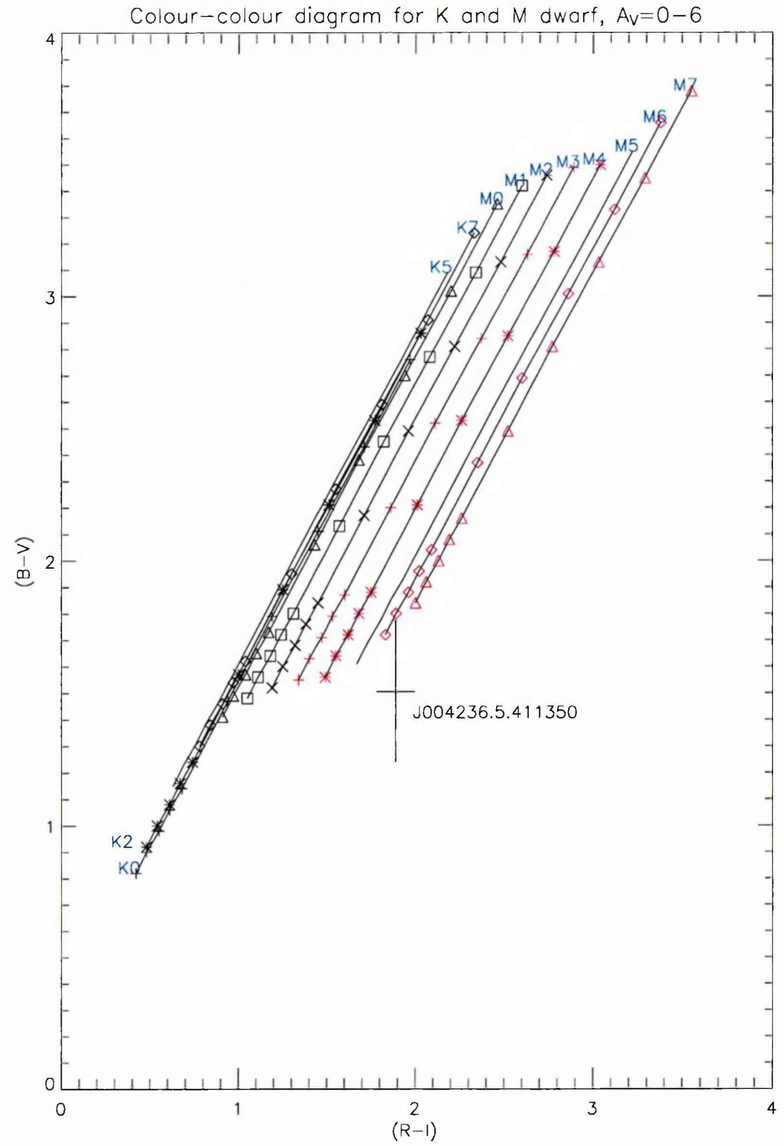

Figure 4.6: Colour-Colour diagram for K and M dwarfs showing the position of J004236.5-411350 with $1\sigma$ error bars shown. Each locus corresponds to $\mathrm{A_V} = 0, 0.25, 0.5, 0.75, 1, 2, 3, 4, 5, 6$ bottom left to top right.

given by Predehl and Schmitt (1995) that we used in our spectral fits. Using the empirical formula for the relation between nH and $A_V$ given by the aforementioned paper,

$$nH(\mathrm{cm}^{-2}) = (1.79 \pm 0.03) \times 10^{21} \mathrm{A_V} \tag{4.4}$$

we have a maximum absorption of $\mathrm{A_V} = 0.36 \pm 0.006$. This may be compared to

McClure and Racine (1969) who obtained $A_V = 0.34$, in the direction of M31. They also go on to state that the absorbing layer extends 200±50pc in this direction. For our source to have $A_V = 0.36$ it would have to lie outside this distance and so we take $A_V = 0.25 \pm 0.11$ as the upper limit on our absorption from Figure 4.6 and Predehl and Schmitt's value. From Carroll and Ostlie (1996), the absolute magnitude of an M6V star is +13.5 and from Table 4.4 we have $m_V$=19.89±0.113. Using the distance modulus,

$$m_V - M_V = 5log_{10}d - 5 + A_V \tag{4.5}$$

the distance to J004236.5+411350 is 170± 50 pc, placing the source within our own galaxy. Hence, using

$$L = 4\pi FD^2 \tag{4.6}$$

where $F$=flux ($\mathrm{ergs\,cm^{-2}s^{-1}}$), the luminosities of our flares are as follows.

Observation 2:

- PN: $L_x = (2.0 \pm 1.2) \times 10^{29}\mathrm{erg\,s^{-1}}$
- MOS: $L_x = (2.0 \pm 1.2) \times 10^{29}\mathrm{erg\,s^{-1}}$

Observation 3:

- PN: $L_x = (3.0 \pm 1.8) \times 10^{29}\mathrm{erg\,s^{-1}}$
- MOS: $L_x = (2.0 \pm 1.2) \times 10^{29}\mathrm{erg\,s^{-1}}$

which lie within the range of luminosity for a flaring star. Tsikoudi et. al. (2000) Table 2, gives X-ray flare luminosities ranging from $10^{27}$ to $10^{30}\mathrm{erg\,s^{-1}}$ with duration of the order $10^3$ seconds, for 31 flares on 14 late-type stars.

### 4.1.5 Misclassification by *ROSAT*

Two deep PSPC surveys of M31 were performed with *ROSAT* and reported by Supper et al. (1997) and Supper et. al. (2001). Each of these observations lasted 200ks, first in 1991 and then follow up observations in 1992/3. We believe that the source designated as *ROSAT* #181 in the first survey and #182 in the second survey is not a bulge source of M31 as classified by Supper et. al. but is J004236.5+411350. In the surveys, a bulge source is classified as a source that is in the bulge of M31 and is not associated with a known foreground object in the Haimen et. al. (1994) catalogue. We know the position of J004236.5+411350 to 20″ and it is the only X-ray source within this circle. The quoted positions of #181, #182 are shown in Table 4.5 and lie within this region (see Figure 4.7).

Table 4.5: Position and maximum count rate in *ROSAT* "B" band (0.1-2.0 keV)

| | #181 | #182 | J004236.5+411350 |
|---|---|---|---|
| R. A. (J2000) | 00 42 35.3 | 00 42 36.7 | 00 42 36.5 |
| Declination (J2000) | +41 13 50 | +41 14 01 | +41 13 50 |
| Count Rate 0.1-2.0keV (cts ks$^{-1}$) | 13.24 | 171.71 | N/A |

A further factor to consider is the maximum observed count rate for this source in the survey, also shown in Table 4.5. The difference in count rate is a factor of 10 between the two surveys which would suggest that during the second observation the star was observed when flaring. However, on analysis of the *ROSAT* lightcurve no flaring could be seen, although the second series of observations did indeed have a higher mean brightness than those taken in 1991. The identity of the source cannot be definitely characterised,

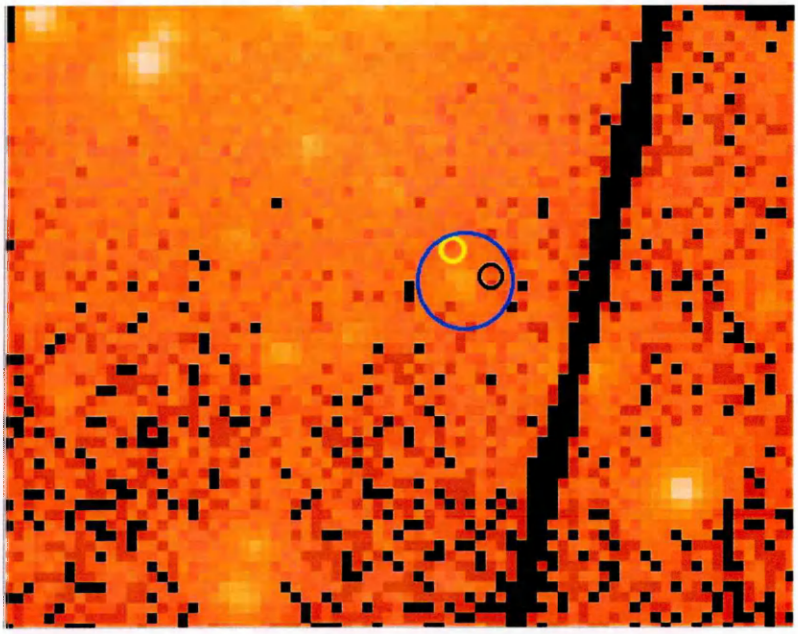

Figure 4.7: Observation 2 PN image showing J004236.5+411350 error circle in blue and the two *ROSAT* positional errors in yellow (#181) and black (#182)

but from Figure 4.7 we can see that there are no other bright sources within $3\sigma$ of the *ROSAT* positions and therefore we suggest *ROSAT* #181/182 to be none other than J004236.5+411350.

### 4.1.6 New Observations of J 004236.5+411350

A series of follow up X-ray observations were taken of the same region of M31 in July 2004. J 004236.5+411350 was detected in two of the four observations, observation 1 and observation 3. Table 4.6 shows all observations obtained from the 2004 run, observation 2 was coincidental with a large solar flare, rendering the observation useless.

Of the two detections, observation 1 and 3, the lightcurves show that only in one observation, observation 1, was a possible flare-like event detected, shown in Figure 4.8. The lightcurve for observation 3 shown only a barely above background constant brightness with no flare-like peaks over the whole observation.

Table 4.6: New *XMM* Observations of the Core of M31 July 2004

| Observation | Date | Duration |
|---|---|---|
| 1 | 16 July 2004 | 18ks |
| 2 | CONTAMINATED | |
| 3 | 19 July 2004 | 22ks |
| 4 | 19 July 2004 | 27ks |

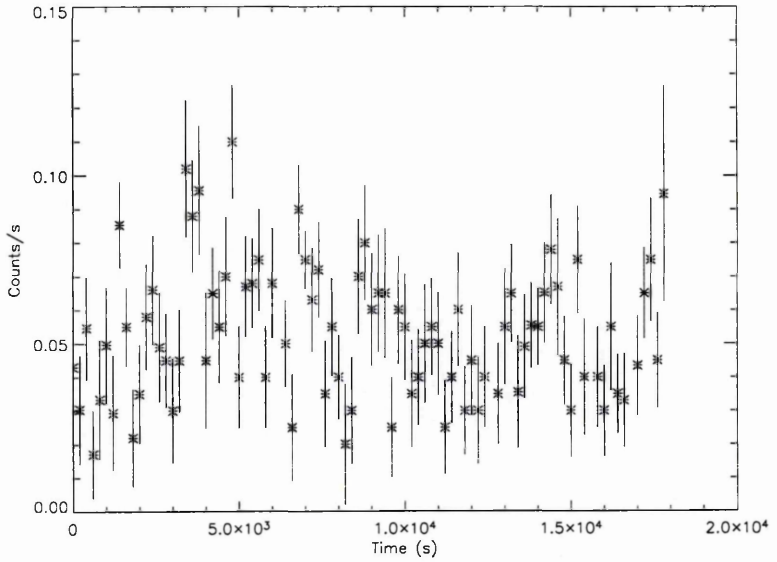

Figure 4.8: Lightcurve of possible flaring event seen in Observation 1 of the 2004 data set, binned to 200s.

When compared to the two previous flaring events for this object, Figure 4.2, this event did not have as clearly defined a peak as the others and so I did not to pursue spectral analysis of this flare.

### 4.1.7 Summary of Findings

We started with a serendipitous observation of two flaring events on an object which was believed to be in the bulge of M31. From the XMM observations we were able to ascertain the flux of these two events. Archival photometric data was used to deduce the spectral type of this object and consequently its distance from us and hence the X-ray luminosity of the flares. The emission measure, plasma temperature and flaring luminosity are consistent with that of a flaring M-dwarf, as shown in sections 4.1.1 and 4.1.4. Additionally an upper limit could be estimated for the quiescent luminosity of J004236.5+411350. Although not flaring in observation 4, the long integration time, 61ks, allowed us to measure the maximum X-ray flux from the region when the source was not flaring. This meant that we could constrain the upper limit for the flux of the source to $\mathrm{F} \leqslant (3.0 \pm 1.0) \times 10^{-14} \mathrm{erg\,s^{-1}cm^{-2}}$ and using our distance estimate and equation 4.6 the quiescent X-ray luminosity, in the 0.3-10 keV range, was $\mathrm{L_X} \leqslant 1.3 \pm 0.86 \times 10^{29} \mathrm{erg\,s^{-1}}$. For an M6V star this give $\mathrm{L_X/L_{bol}} \leqslant 0.006 \pm 0.004$. Most M-dwarfs have quiescent $\mathrm{L_X/L_{bol}} \leqslant 0.002$ (James et. al. 2000), whereas our limit is closer to that of a late K-type dwarf. As pointed out, the value for J004236.5+411350 is an upper limit and as such does not disqualify this object as an M-dwarf, but also constrains the object to later than K-type.

A comparison of the M31 flare star X-ray flare luminosity to that of some of the largest flares ever observed on the Sun (X10) shows that the two flares observed are approximately one hundred times more intense. In the GOES classification, section 2.3.1 they would be of the order X1000 class flares.

The luminosity of a flare, as we have seen, is dependent on the emission measure and the plasma temperature during the flare. Forbes et. al. (1989) showed that the radiative cooling function for a coronal plasma was inversely proportional to the plasma temperature i.e. if the temperature increases the rate of energy loss, in the form of soft X-rays, decreases. This would suggest that just increasing the temperature of a flaring plasma would not cause an increase in the flux. Forbes et. al. also showed that the radiative cooling function was proportional to the square of the electron density. So denser plasmas produce a higher soft X-ray flux than less dense plasmas at the same temperature. The emission measure is related to the electron density by the following equation:

$$EM = \int n_e^2 dV, \tag{4.7}$$

so EM is the integral of the square of the electron density over the flaring volume.

Looking at Figure 4.5 we see that the data suggests that the electron density in our and other flare stars is higher than in the Sun. We have higher emission measures for a given temperature, due to either a more dense plasma in the stellar case, or a larger flaring volume.

We consider these two possibilities in turn. If the higher emission measure in flare stars is due to a larger flaring volume then one possible way to achieve this on a M-dwarf of $0.5R_\odot$ would be to have large regions of the stellar surface flaring. Since stars later than approximately M5V (Güdel 2004) are thought to be fully convective, there is no shear zone between a radiative core and convective region. This mean that the magnetic field of these objects has to be produced by an $\alpha$ or distributive dynamo (Giampapa et. al. 1996). This means that the magnetic field is produced through turbulence in the stellar atmosphere (Durney et. al. 1993). Hence the magnetic field is distributed over the stellar surface and, as described by Pearce et. al. (1990), one flaring event can trigger further events in nearby, on the Sun within 30 degrees, regions of stressed magnetic fields. This phenomenon is called sympathetic flaring. This cascade event could also account for the longer durations of the events observed. The impulsive and decay phases of the flares would be longer due to the flare at first propagating then decaying across the stellar surface.

Alternatively, if the flaring volume on flare stars is similar to that on the Sun ($10^{27}$cm$^3$ Saint-Hilaire et. al. 2005) but the electron density is higher. This would lead to a higher rate of cooling, and also a higher EM. To probe the electron density of the coronae, density sensitive coronal emission lines are used. The ratio of He-triplet like lines can directly measure the density. Ness et. al. (2003) used observations by *XMM* and *Chandra* to measure the ratio of the forbidden (22.10Å) and intercombination (21.80Å) lines of OVII for 20 active stars. They found that for flare stars the electron density scaled with the EM, suggesting that on flare stars the limited available volume means that for increased EM there must be an increase in $n_e$ to account for the energetic flaring events observed. Typical values obtained where in the range $n_e = 2 \times 10^9 - 1 \times 10^{11}$cm$^{-3}$. Observations of AT Mic with *XMM* (Raassen et. al. 2003) using the same method, and the ratio of OVII lines gave values for quiescent and flaring $n_e$ equal to $2 \times 10^{10}$cm$^{-3}$ and $4 \times 10^{10}$cm$^{-3}$ respectively. If, taking a median value, $n_e$ for the two flares on J004236.5+411350 was of the order $5 \times 10^{10}$cm$^{-3}$, then using the approximation $EM = n_e^2 V$ the emitting volumes of the two flares would be $(1.1 \pm 0.14) \times 10^{31}$cm$^3$ and $(3.4 \pm 1.2 \times 10^{31})$cm$^3$ for observation 2 and 3 respectively, comparable to the values obtained for AT Mic.

Both possibilities are viable for J004236.5+411350 but considering the values EM, $n_e$ and volume I favour a combination of a high coronal density and a larger than solar, flaring volume, as the cause of these two X1000 flares.

## 4.2 Flaring Behaviour In The WAVS Survey

In July 1999 an unbiased photometric survey was performed with the Canada-France-Hawaii Telescope on a 0.33 square degree field, to search for variable stars, the so called Wide Angle Variability Survey or WAVS as it will be referred to in this work (Lott et. al. 2002 and Lott 2004). The survey yielded two nights of three minute time resolution V-band photometry of over 52,000 objects down to a limiting V magnitude of 23.5. Of these 52,000 objects, three were noted by Lott to display flarelike events. Figure 4.9 shows the lightcurves of these three objects. None of the three objects appear to have been observed before as part of any other survey and no previous reference could be found to them in any of the catalogues available from CDS.

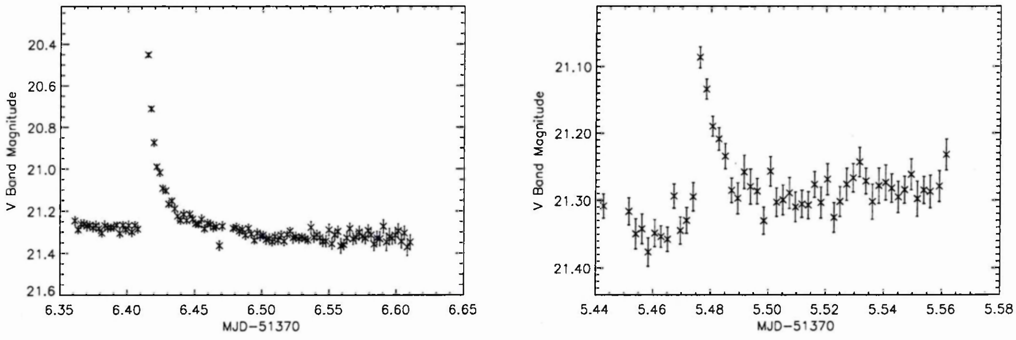

(a) WAVS323426

(b) WAVS912537

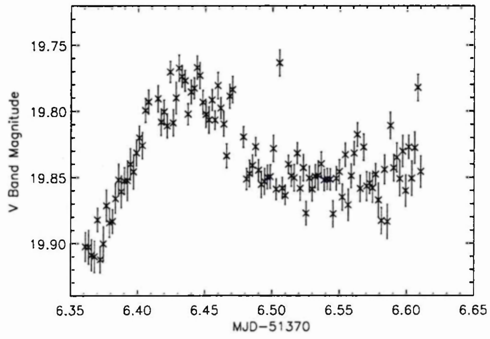

(c) WAVS920239

Figure 4.9: The three WAVS lightcurves showing flaring behaviour.

In these three objects we see the rapid brightening and exponential decay indicative of a flaring event. Figure 4.9(a) and (b) show relatively impulsive events with duration 1000-2000s with increase in V magnitude of approximately 0.85 and 0.25 respectively, whilst Figure 4.9(c) shows a much longer duration event of more than 20,000s with $\Delta$V of the order 0.2. To identify the nature of these flaring objects follow up spectroscopy was performed in 2003 using the WHT, part of the Isaac Newton Group of Telescopes, in service mode. Henceforth the flaring event of WAVS323426 will be known as WAVS_FLARE_1, similarly the WAVS912537 event will be referred to as WAVS_FLARE_2 and the event on

WAVS920239 as WAVS_FLARE_3

### 4.2.1 WHT/ISIS Observations

On the night of the 3rd August 2003 the three flaring objects were observed using the ISIS spectrograph on the *WHT* in service mode. Only the red arm of ISIS was used since the majority of flare stars are very red objects, late-type K and M stars (Pettersen et. al. 1989). Table 4.2.1 shows the exposure times and the WAVS V magnitude of the targets obtained on this run. The wavelength coverage was 4800Å-9100Å, chosen to provide coverage of the following strong features found in M dwarfs: TiO band 5847-6058Å, TiO band 6080-6390Å, Ca I 6162Å, CaH triplet 6346,6382,6389Å, H$\alpha$ 6563Å, TiO band 6651-6852Å, TiO band 7053-7270Å, VO band 7851-7973Å, TiO band 8206-8569Å, and TiO band 8859-8937Å.

The observations were taken in service mode using the MARCONI CCD and the R158R grating. This combination gave a spectral resolution of 1.6Å/pixel.

### 4.2.2 WHT/ISIS Spectra

The data were reduced using standard techniques with IRAF as described in Chapter 3. The spectra were found to be noise dominated below approximately 5000Å and so the range 5000Å-9100Å was used for all analysis. Since multiple spectra for each star were obtained, these were averaged together to reduce the noise. Each spectrum was flux calibrated against the standard HD217086 (O5V) before averaging, to check for variation in the flux between each observation, of which there was none. For each of the three flux calibrated spectra the V magnitude of the star was calculated using the IRAF package CALCPHOT in the SYNPHOT routine listing. CALCPHOT calculates the response over the Johnson V passband for a given flux calibrated spectrum. Table 4.2.2 gives the calculate V magnitude for each star along with the WAVS magnitude.

| Start Time UT | Object | RA | DEC | Exposure Time(s) | V magnitude |
|---|---|---|---|---|---|
| 01:40:03 | WAVS912537 | 20 26 55.9 | +27 41 19.0 | 1800 | 21.25 |
| 02:15:24 | WAVS912537 | 20 26 55.9 | +27 41 19.0 | 1800 | 21.25 |
| 02:55:18 | WAVS323426 | 20 27 26.9 | +27 52 04.1 | 1800 | 21.6 |
| 03:38:58 | WAVS323426 | 20 27 26.9 | +27 52 04.1 | 1800 | 21.6 |
| 04:08:27 | WAVS920239 | 20 27 07.9 | +27 32 58.6 | 600 | 19.9 |
| 04:18:40 | WAVS920239 | 20 27 07.9 | +27 32 58.6 | 600 | 19.9 |
| 04:28:54 | WAVS920239 | 20 27 07.9 | +27 32 58.6 | 600 | 19.9 |
| 04:43:13 | WAVS920239 | 20 27 07.9 | +27 32 58.6 | 600 | 19.9 |
| 05:40:39 | HD217086 | 22 56 47.19 | +62 43 37.6 | 7 | Spectrophotometric Standard (7.7) |

Table 4.7: Log of WHT/ISIS Observations 03/08/2003

| Star | $V_{\text{calcphot}}$ | $V_{\text{WAVS}}$ |
|---|---|---|
| WAVS_FLARE_1 | 20.8 | 21.6±0.02 |
| WAVS_FLARE_2 | 21.1 | 21.09±0.02 |
| WAVS_FLARE_3 | 19.6 | 19.9±0.01 |

Table 4.8: WAVS and calculated V magnitudes from WHT spectra for the three flare star targets.

The calculated magnitude of the three stars was lower i.e. brighter than that of the quoted WAVS magnitude, for WAVS_FLARE_1 and WAVS_FLARE_3. WAVS_FLARE_2 on the other hand was in good agreement with the WAVS magnitude. This is odd as we would expect any difference to be the other way round due to slit losses. Therefore this inconsistency could result from systematic errors in the WAVS calibration. Observations of the photometric standard star were only taken on the first night of the WAVS observations and only one of our flares, WAVS_FLARE_2, was observed on this night. This has the smallest difference in magnitude between CALCPHOT and WAVS supporting the argument for an error in the WAVS calibration for the second night of observation.

Figures 4.10, 4.11, and 4.12 show the averaged flux calibrated spectra of the three stars observed at the WHT. On each plot the features listed in section 4.2.1 are labelled.

Figures 4.11 and 4.12 show that two of the objects (WAVS_FLARE_3 and WAVS_FLARE_1) display typical M-dwarf spectra, a red continuum dominated by molecular absorption bands. The third object (Figure 4.10) was found to be essentially featureless over the entire wavelength range covered.

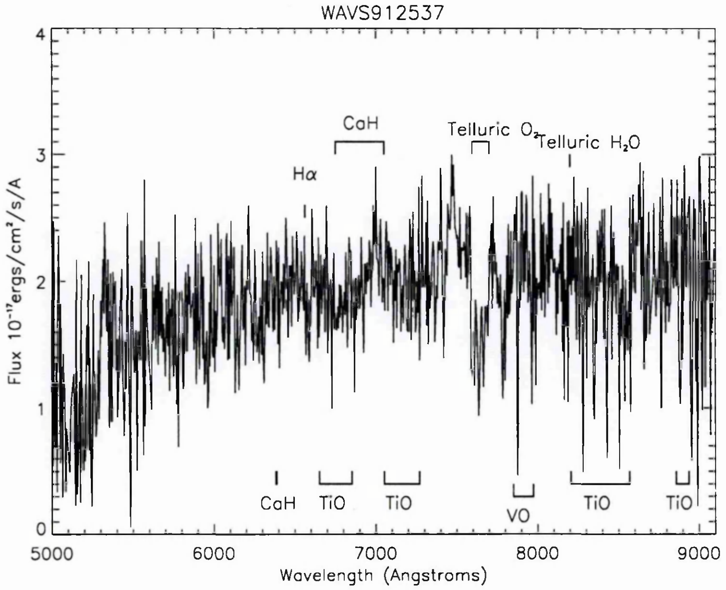

Figure 4.10: Flux calibrated spectrum of WAVS_FLARE_2

### 4.2.3 M Dwarfs

In order to identify the spectral type of the two M-dwarf stars the averaged flux calibrated spectra were compared to the full range of M-star spectral types found in "A Stellar Spec-

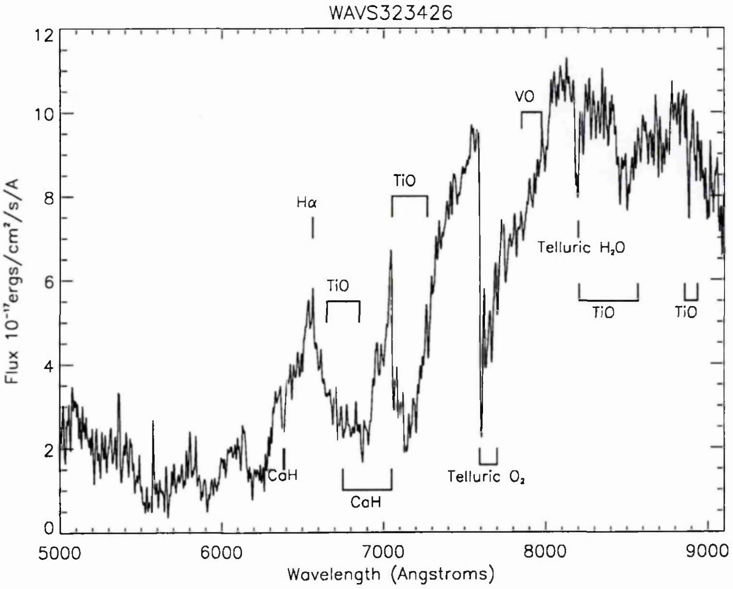

Figure 4.11: Flux calibrated spectrum of WAVS_FLARE_1

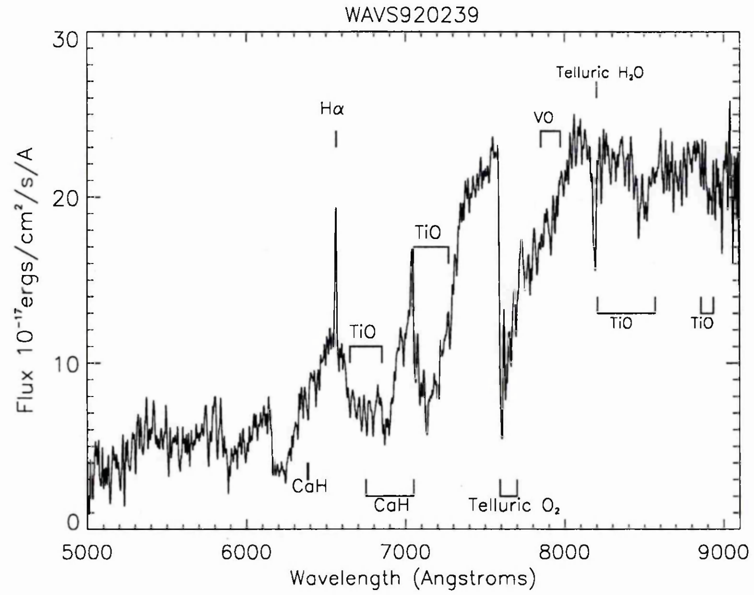

Figure 4.12: Flux calibrated spectrum of WAVS_FLARE_3

tral Flux Library: 1150 - 25000Å " (Pickles 1998) and henceforth known as the Pickles data set. These spectral types were, M0III, M0V, M1III, M1V, M2I, M2III, M2.5V, M2V, M3II, M3III, M3V, M4III, M4V, M5III, M5V, M6III, M6V, M7III, M8III, M9III and M10III. The flux of our targets is normalised to one at 5556Å to match the normalisation of the Pickles data set. The target spectra and Pickles data were compared using residual $\chi^2$ fitting to get a first approximation to the spectral type of the WAVS objects. Since the Pickles data set is based on real data the best fit Pickles spectra and the target spectra do not match exactly, to improve upon this first approximation the spectrum of the Pickles template star was multiplied by a range of constant factors and the resulting template subtracted from the flux calibrated spectrum of our target star. The residuals were then tested against a line of constant value in a $\chi^2$ test, and the minimum $\chi^2$ taken to be the best fitting template. In the case of both WAVS_FLARE_3 and WAVS_FLARE_1 the best fitting template was that of an M4V dwarf multiplied by constants of 0.9 and 0.85 respectively. This suggests the value of the flux at 5556Å is not necessarily representative of the flux over the whole wavelength range and hence some modification to the flux must be made to match the standard spectrum. Figure 4.13 and 4.14 show the flux calibrated spectra of WAVS_FLARE_3 and WAVS_FLARE_1 with the scaled M4V spectrum overplotted in red.

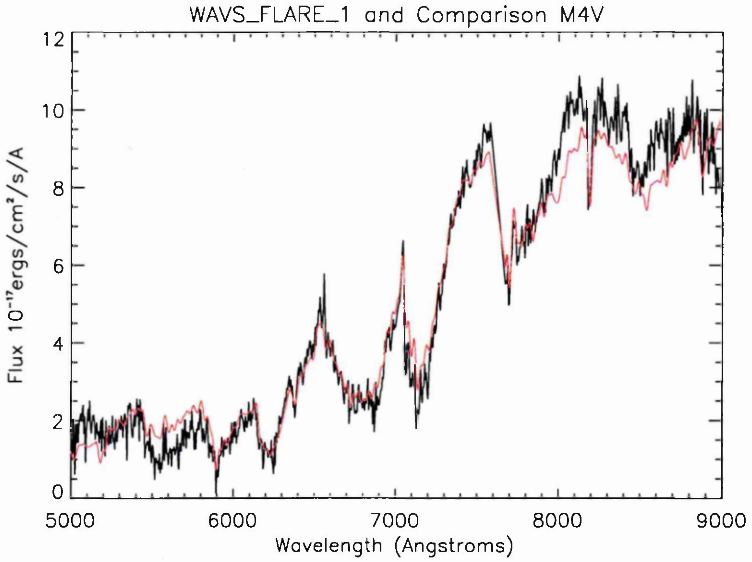

Figure 4.13: Flux calibrated spectrum of WAVS_FLARE_1 with M4V overplotted (red)

As a further check the spectra were also dereddened for a range of E(B-V) values 0-0.9, and again tested against the Pickles data set. It was found that for WAVS_FLARE_1 and WAVS_FLARE_3, the unreddened spectra gave the best fit to the residuals and so the spectra presented in Figures 4.14 and 4.13 remain unreddened.

### 4.2.4 Unclassified Flaring Object

The third target observed exhibited a featureless continuum over the entire wavelength range of the observation, with the exception of the Telluric oxygen band 7600Å-7700Å (Figure 4.10). The flux calibrated spectrum was used in conjunction with CALCPHOT to calculate the V magnitude of the object for these observations, V=21.06 in this case.

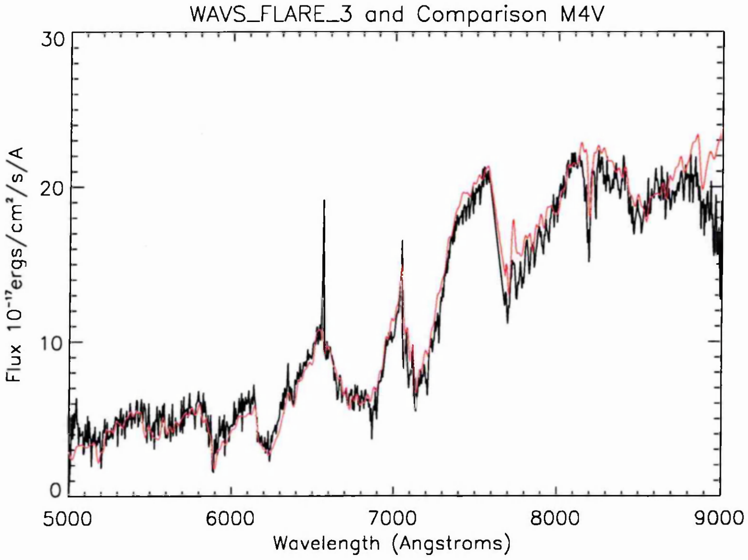

Figure 4.14: Flux spectrum of WAVS_FLARE_3 with M4V overplotted (red)

Figure 4.15 shows the normalised flux calibrated spectrum of WAVS_FLARE_2 with a comparison M4V spectrum overplotted. We see that the continuum of WAVS_FLARE_2 is much bluer than that of an M-dwarf. WAVS_FLARE_2 also exhibits none of the characteristic M-dwarf photospheric features, e.g. TiO and CaH molecular bands. This makes the object something of an enigma. Possible solutions are that this is an early spectral type star exhibiting flaring (c.f. Schmitt 1994), hence its effective temperature is too high for molecular TiO to be present in the photosphere. Another more exciting prospect is that the flare like event seen in the WAVS survey may have been the optical counterpart to a Type I X-ray burst. These bursts occur in Low Mass X-ray Binaries (LMXB) where the matter accreted onto the neutron star undergoes thermonuclear fusion on the neutron star surface, and typically have a duration of 3-1000s (Lamb 2000). Optical counterparts to X-ray bursts have been observed in the past. For example Kong et. al 2000, observed a burst simultaneously in the X-ray (*RXTE*) and in the optical (SAAO). The optical burst was found to follow the general shape and duration of the X-ray burst after an approximately 3 second delay. This burst had a duration of the order 1 minute and its brightness increase by approximately 90% (count $s^{-1}$) in the optical. This does not compare well with the observed brightening and duration of our object , which shows a 30% increase in optical brightness and a duration of the order 3000 seconds. A third and least exciting prospect is that the observation itself is incorrect and this is not the star we had intended to observe at all. The field is shown Figure 4.16.

A further test of the burst hypothesis is as follows. Assuming we have blackbody radiation from a neutron star at a typical temperature, $10^7$K, for these systems, what optical flux would we expect in the range 5000Å to 9000Å and how far would the system have to be away from us to give the observed flux we have?

We know the total observed flux in the 5000Å to 9000Å range is $3\times10^{-14}$ergs$^{-1}$cm$^{-2}$ from our flux calibrated spectrum. Using

$$L_\lambda d\lambda = \frac{2\pi hc^2}{\lambda^5 e^{hc/\lambda kT} - 1} d\lambda \tag{4.8}$$

where $\lambda$ is the wavelength, $h$ is Planck's constant, $c$ is the speed of light in a vacuum, and T is the temperature of the blackbody. Integrating between the limits 5000Å and 9000Å we get a luminosity $L$=1.8 x $10^{27}$erg $s^{-1}$ and using equation 4.6 we get a distance of approximately 22pc. This puts it a lot closer than the majority of neutron stars, most are seen in the bulge of the galaxy at around 15kpc. Additionally if the blackbody spectrum itself is compared to the source spectrum, Figure 4.15, for the same total flux in the range 5000 - 9100Å, it is clearly not an appropriate model for the emission seen. This is may be the final nail in the coffin for our burst hypothesis, as a combination of this distance calculation, examination of the blackbody curve, and the observations of optical counterparts to X-ray bursts already mentioned make it seem very unlikely indeed.

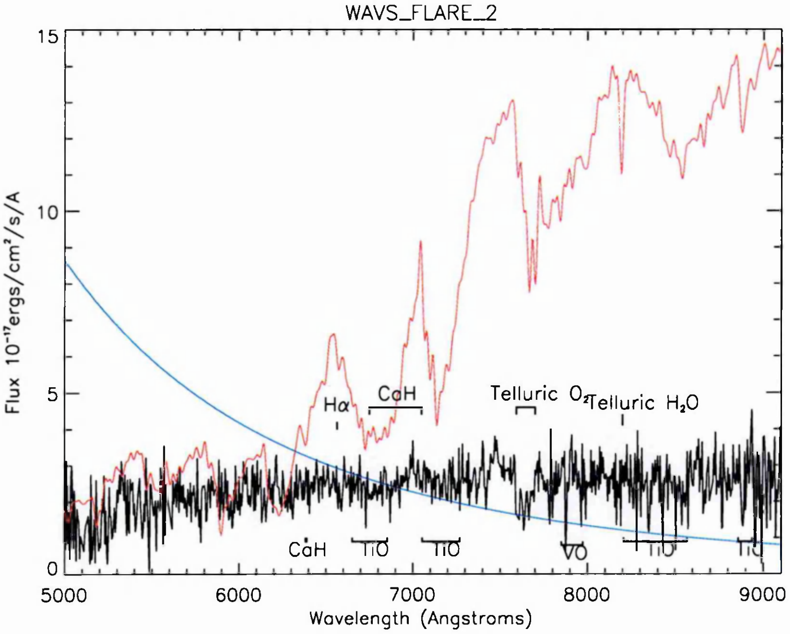

Figure 4.15: Flux calibrated spectrum of WAVS_FLARE_2 with the M4V (Pickles) spectrum, overplotted (red), and a $10^7$K blackbody curve for the same total flux (blue).

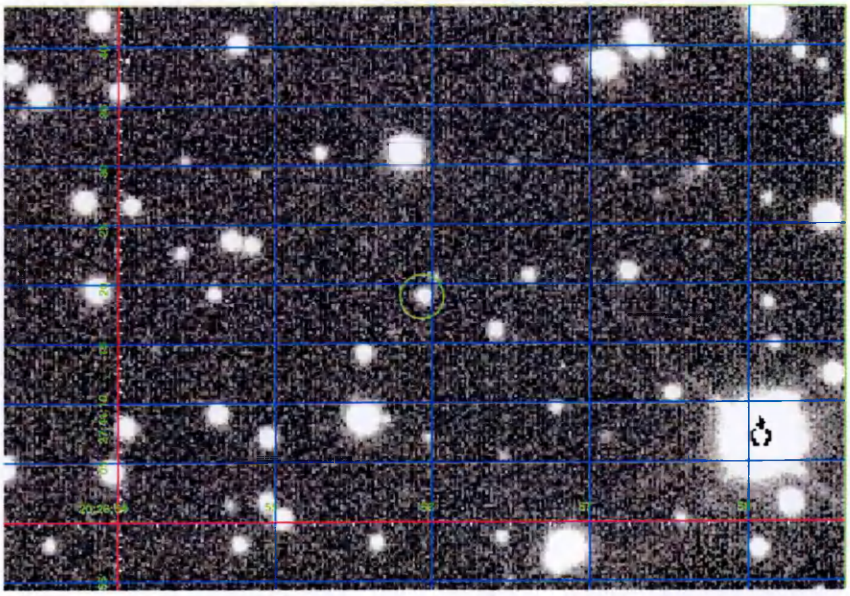

Figure 4.16: Finding Chart for WAVS_FLARE_2 North is vertically up and East is to the right. Target marked with green circle. The image is 49″ × 76″.

*Early Spectral Type Fitting*

As mentioned above, it is possible that the object is of an earlier spectral type in which the broad absorption bands seen in M-dwarfs are not present. Using the extended Pickles data set spectral types F-M (Pickles 1998), the spectra of WAVS_FLARE_2 was tested using the same method as outlined above. On first inspection the best fit, minimum $\chi^2$ on the residuals, was that of K5III spectral type. If this was the case the object would have to be approximately 260kpc away, based on the V-band magnitude from our synthetic photometry. This would put it well outside our Galaxy. This was an unlikely result, so the spectra for WAVS_FLARE_2 was dereddened for the same range of E(B-V) as for the M-dwarfs, and simultaneously fitted to the extended Pickles data set. The resulting minimum $\chi^2$ fit suggests the object is spectral type K4V with a reddening coefficient of E(B-V)=0.25. Figure 4.17 shows the dereddened spectra of WAVS_FLARE_2 with the spectra of the Pickles K4V for comparision.

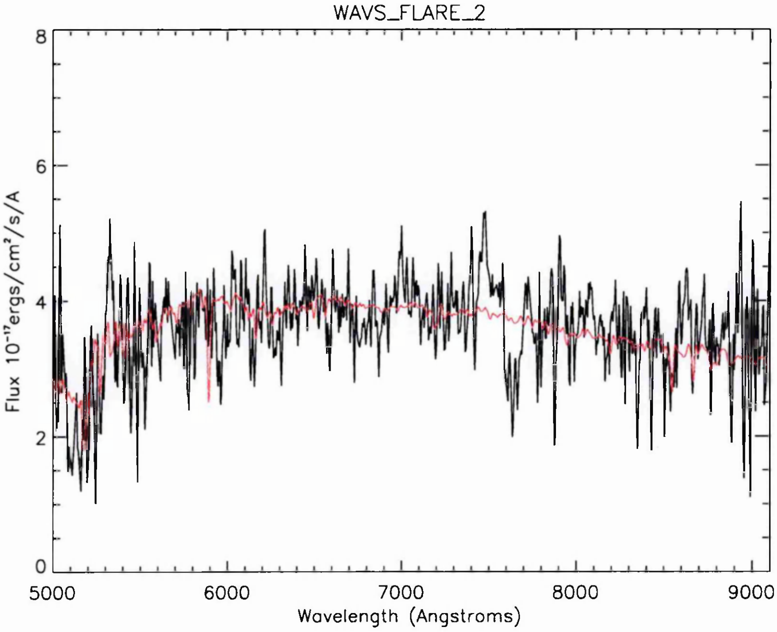

Figure 4.17: Dereddened spectra of WAVS_FLARE_2 and the corresponding Pickles spectra for a K4V for comparision (red).

With spectral type K4V WAVS_FLARE_2 would be approximately 5kpc distant which is a far more resonable value, placing the object in our own Galaxy.

### 4.2.5 Flaring in the WAVS survey: Conclusions

Of the three flaring sources seen in the 1999 WAVS survey, two are typical M-dwarf flare stars, displaying prominent molecular absorption bands and chromospheric emission (H$\alpha$). The third source is apparently something else. One possibility was that this event could have been the optical counterpart of a type I X-ray burst. The profile of this event is consistent with that of these events, but the duration of our event is longer and the increase in brightness is smaller than seen in other examples of the optical counterpart of a Type I X-ray burst. If this had been the case it would have been the first time a system of this nature has been discovered in the optical. The discussion in section 4.2.4 indicates this is a very unlikely candidate for a Type I X-ray burst.

Another more likely, possibility is a flare from a star of earlier spectral type star flaring. Fuhrmeister and Schmitt 2003 have identified 994 flares from 1207 variable objects within the ~30,000 sources in the *ROSAT* All Sky Survey. Of these ~1200 variable objects, 137 were of spectral type M and 163 of types O to G, so there is a strong case for an earlier spectral type flaring in the WAVS survey. Fitting of earlier spectral types to the dereddened spectra of WAVS_FLARE_2 did indeed reveal that the object is most likely a K4V and as such one would expect spectacular flaring events to occur on it. To further verify the nature of the object a second *WHT* proposal to perform spectroscopy at bluer (3100-8300Å) wavelengths was submitted, it has however not been carried out.

# Chapter 5

# 1RXS J 162848.1-415241: The Brightest Known Microquasar?

In the following chapter we shall present observations for what could be the brightest known microquasar. Section 5.2 will present the spectroscopic observations of this object conducted at SAAO and the radial velocity calculations. In Section 5.3 we shall attempt to use spectral synthesis to identify the evolutionary state of the object, and finally in Section 5.4 we will present the findings from photometric monitoring of the object with the ROTSE system and draw our conclusions about this object. We set out looking for a microquasar and found something altogether different.

## 5.1 1RXS J 162848.1-415241

1RXS J 162848.1-415241 was first reported by Tsarevsky et al (ATEL #80) as the most likely candidate out of 40 possible new microquasars. Each of these 40 objects were selected by comparing a sample of bright *ROSAT* sources, taken from the *ROSAT* All Sky Survey (limiting flux $2\times10^{-14}$ergcm$^{-2}$s$^{-1}$ in the 0.1-2 keV band) with hard X-ray spectra, resembling those of known X-ray binaries, to radio sources from the GB6/PMN/NVSS surveys (covering the whole sky north of -87.5 dgrees declination, with limiting flux 18mJy, 20-72mJy and 2.5mJy respectively) (Tsarevsky et. al. 2001). 1RXS J 162848.1-415241 was observed to have a flat radio spectrum, with an unresolved core, but with no conclusive identification of extended radio sources indicative of the presence of jets. The precise radio coordinates led to an optical identification with a relatively bright (V=13.4) source. Low resolution spectroscopy performed by the same group with the AAO 4m telescope showed the source to be a star of spectral type K5, with strong, variable H$\alpha$ emission. Observations with the ATCA revealed variability in the radio emission. The combined X-ray, optical and radio observations were thought to be suggestive of microquasar behaviour, but an isolated active K type star could not be ruled out. A call for further observations was broadcast using VSNET. The driving force behind our observations was to establish the binary nature of 1RXS J 162848.1-415241 through radial velocity measurements made from spectra obtained in South Africa.

## 5.2 Observations at SAAO

1RXS J 162848.1-415241, henceforth referred to as J1628, was observed with the 1.9m Radcliffe telescope at SAAO on the 17th to 24th of June 2003 using the Cassegrain Grating Spectrograph with grating 5 and the 266 x 1798 pixel SITe CCD. The spectra cover a wavelength range approximately 6100Å - 6900Å at a resolution of 1.2Å per pixel. The observations of J1628 are listed in Table 5.1. A range of exposure times was used, 60 to 600 seconds, to look for variablity in the spectral lines on a range of time scales.

The spectra obtained were reduced using standard packages in IRAF as outlined in Chapter 3. The continuum was normalised to one to ease the comparison with the observed template stars. This was achieved by fitting a function to the continuum and dividing by the fit, as described in Section 3.6. In the case of 1RXS J 162848.1-415241 a third order cubic spline fit was sufficient to fit the broad features of the continuum (Figure 5.1).

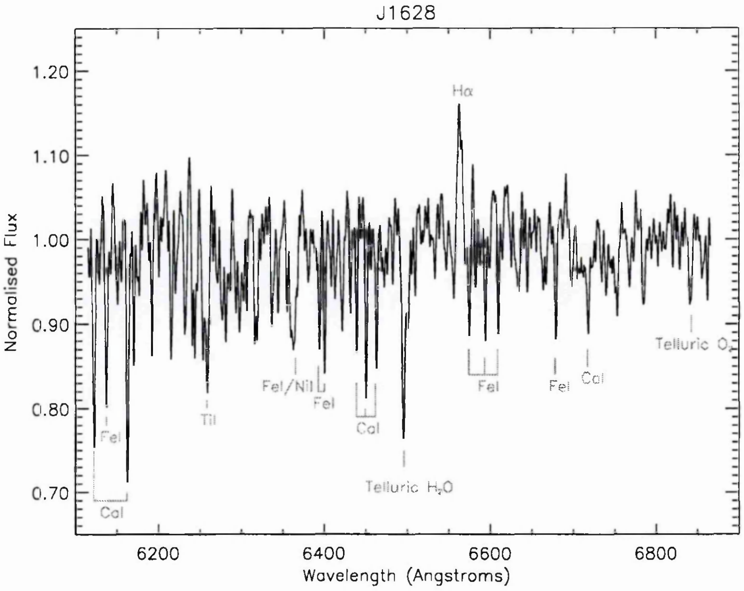

Figure 5.1: Mean normalised spectrum of J1628 observed at SAAO. Prominent features are labelled in red.

Table 5.1: Observation Log for 1RXS J 162848.1-415241 from SAAO.

| Date June 2003 | Time UT | Exposure Time(s) | Number of Exposures |
|---|---|---|---|
| 17th 18th | 1655 | 180 | 1 |
| | 17:00 | 600 | 49 |
| 18th 19th | 1753 | 600 | 10 |
| | 19:44 | 300 | 12 |
| | 20:54 | 180 | 42 |
| | 00:38 | 300 | 8 |
| 19th 20th | 1717 | 120 | 1 |
| | 17:21 | 180 | 60 |
| | 20:57 | 120 | 46 |
| | 00:02 | 180 | 12 |
| | 00:45 | 240 | 15 |
| 20th 21st | 1844 | 240 | 10 |
| | 19:30 | 180 | 44 |
| | 23:01 | 240 | 25 |
| 21st 22nd | 1926 | 300 | 22 |
| | 23:36 | 120 | 1 |
| | 00:01 | 600 | 5 |
| *21st 22nd* | 00:57 | 450 | 1 |
| *continued* | 01:06 | 600 | 1 |
| 22nd 23rd | 1832 | 120 | 2 |
| | 18:37 | 180 | 28 |

Table 5.1: ...continued

| *Date* | *Time* | *Exp. time* | *No. exp.* |
|---|---|---|---|
| | 20:21 | 120 | 75 |
| | 00:50 | 180 | 1 |
| | 00:53 | 120 | 4 |
| 23rd 24th | 1724 | 180 | 18 |
| | 18:31 | 120 | 30 |
| | 20:11 | 60 | 67 |
| | 21:51 | 120 | 50 |
| | 00:07 | 180 | 18 |

For the purpose of radial velocity measurements and identification of the spectral type of J1628 ten K-type stars from K1V to K7V and a K5III star were also observed during the same run, as shown in Table 5.2. The continuum of these spectra was also normalised to one, and the full range of spectral types observed are shown in Figure 5.2.

Table 5.2: Observation Log for K-type stars from SAAO.

| Object (Spectral Type) | Date June 2003 | Time UT | Exposure Time(s) | Number of Exposures |
|---|---|---|---|---|
| Y4924 (K7V) | 18 | 02:57 | 30 | 3 |
| | 19 | 01:44 | 5 | 2 |
| | 19 | 01:46 | 30 | 6 |
| | 20 | 02:07 | 30 | 10 |
| Y5243 (K7V) | 18 | 03:04 | 45 | 3 |
| | 19 | 01:58 | 45 | 8 |
| | 20 | 02:23 | 45 | 10 |
| BS5568 (K4V) | 22 | 23:03 | 5 | 1 |
| | 22 | 23:04 | 10 | 9 |
| HD144500 (K1V) | 22 | 23:13 | 120 | 6 |
| HD144628 (K1/2V) | 22 | 23:33 | 60 | 4 |
| BS6171 (K2V) | 23 | 01:09 | 10 | 10 |
| HD167981 (K3V) | 23 | 01:22 | 30 | 1 |
| | 23 | 01:23 | 60 | 5 |
| HD156026 (K5V) | 23 | 01:33 | 30 | 9 |
| BS7541 (K5III) | 24 | 01:21 | 5 | 1 |
| | 24 | 01:22 | 10 | 16 |
| HD203040 (K5V) | 24 | 01:36 | 30 | 1 |
| | 24 | 01:37 | 60 | 7 |

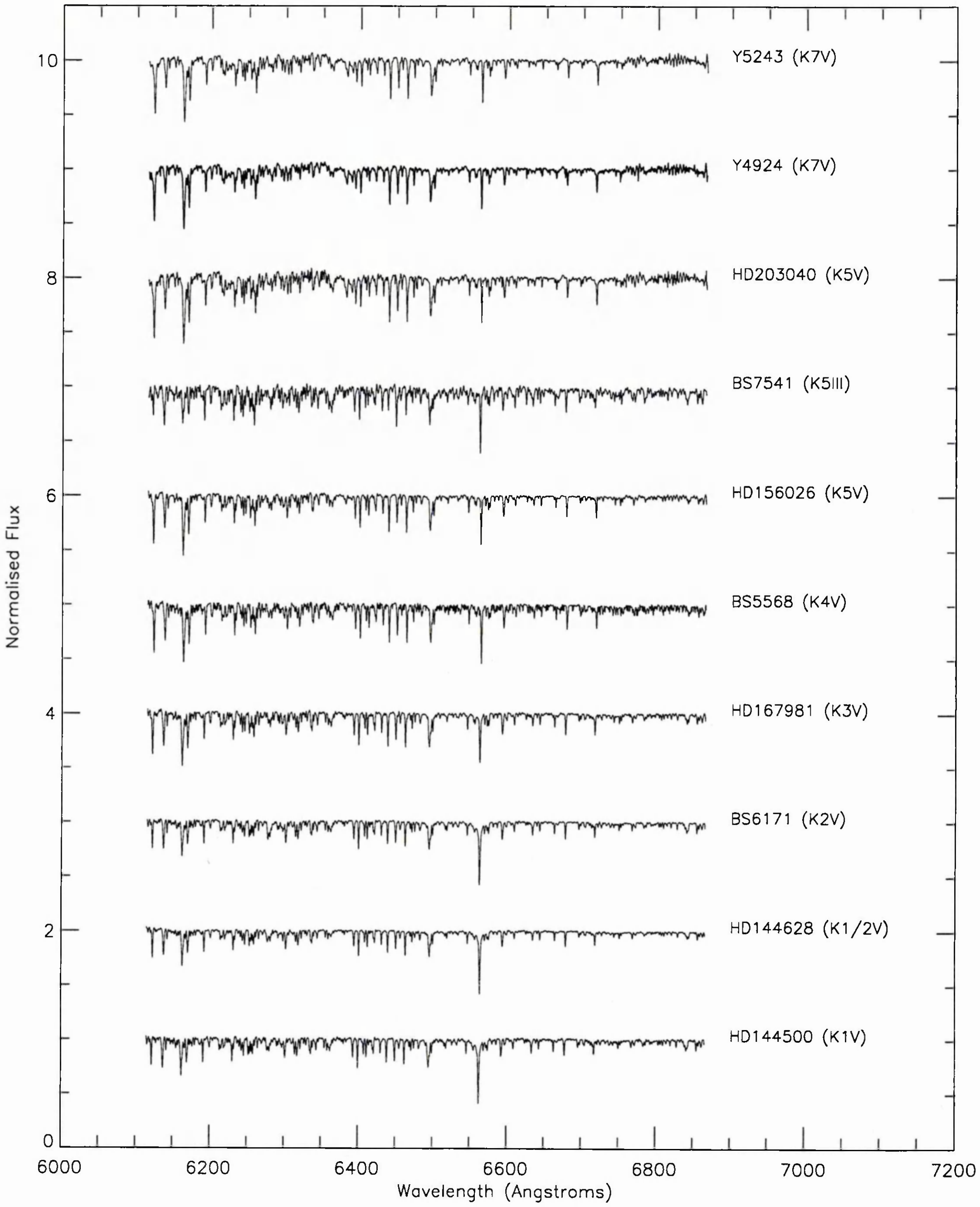

Figure 5.2: Stack of mean, normalised spectra for the observed K-type template stars obtained at SAAO.

### 5.2.1 Radial Velocity Measurements

In order to identify the binary nature of J1628, its spectral features were compared to those of the K-type templates obtained on the run. This was done using the IRAF package FXCOR which performs a Fourier cross-correlation on the features within a specified wavelength range (Tonry and Davis 1979). In the case of J1628 and the templates, the range 6350Å to 6470Å was chosen as it contains several strong absorption features, no telluric features and no emission features in J1628 or the templates. H$\alpha$ is in emission in J1628, but in all K-type spectra H$\alpha$ is in absorption.

The calculated radial velocities were plotted and a clear sinusoidal signature was present, in the case of correlation against each of the ten template stars observed. The radial velocity and the associated errors were then fitted with a sinusoid of the form,

$$v = \gamma + K_2 sin((t - t_0)/P) \tag{5.1}$$

where $v$ is the radial velocity, $K_2$ is the velocity semi-amplitude and $P$ is the period of the system. This was done using the IDL routine CURVEFIT, Figure 5.3 shows the radial velocity data, from comparison with the template HD144628 (K1/2V), and the associated fit. This fitting gave values for the period of J1628 and the orbital velocity, $K_2$, to be $4.869 \pm 0.007$ days, and $33.8 \pm 0.1$ kms$^{-1}$ respectively. The radial velocity curves for the other nine templates are in agreement with these values.

The fit values of the radial velocity curve were used to correct the spectra of J1628 and the other nine template stars to the radial velocity of HD144628 for comparison of their spectral features.

### 5.2.2 Spectral Type Identification

The radial velocity corrected spectra of J1628 were averaged together for each of the seven nights of observation. The same process was applied to the template spectra for each template. Using these high signal to noise spectra each template was subtracted from the nightly averaged spectra of J1628 and the residuals examined for a transition from

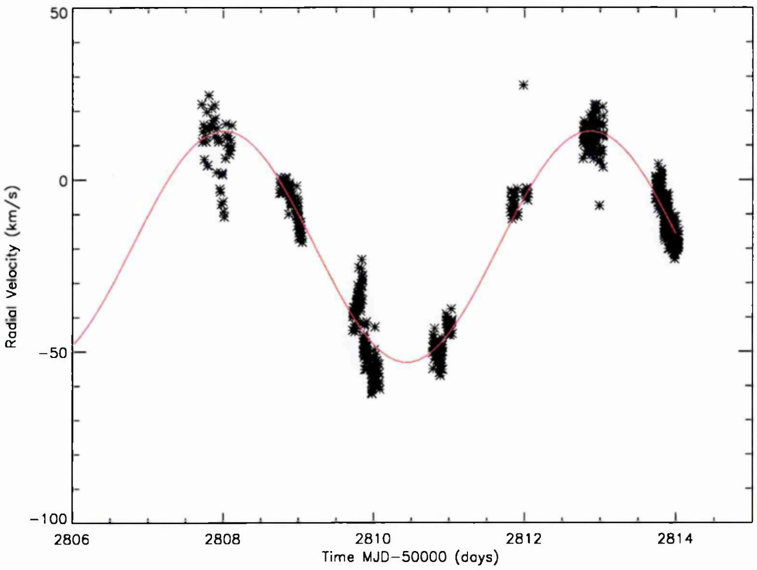

Figure 5.3: Radial velocity of J1628 relative to HD144628 (K1/2V) with fitted curve (red), P=4.869 ± 0.007 days, and $K_2 = 33.8 \pm 0.1$ kms$^{-1}$

emission like features to absorption like and visa versa. Figure 5.4 shows the results for night one of the observations.

The transition seen in Figure 5.4 between K2V and K3V suggests that the spectral type of J1628 lies within this range. It is worth noting that the residuals for BS7541, the K5III star, also appear to have relatively small features, and as such we cannot rule this out at this stage.

### 5.2.3 $\chi^2$ Testing

To test the goodness of fit of the templates, the residuals were compared to a line of constant value in a variance weighted $\chi^2$ test. This should indicate which template star most closely matches the spectrum of J1628 and hence the spectral type of J1628. During the $\chi^2$ test any emission features (H$\alpha$) in J1628 were masked out since in the template spectra all features are in absorption, and emission minus absorption results in a large deviation from

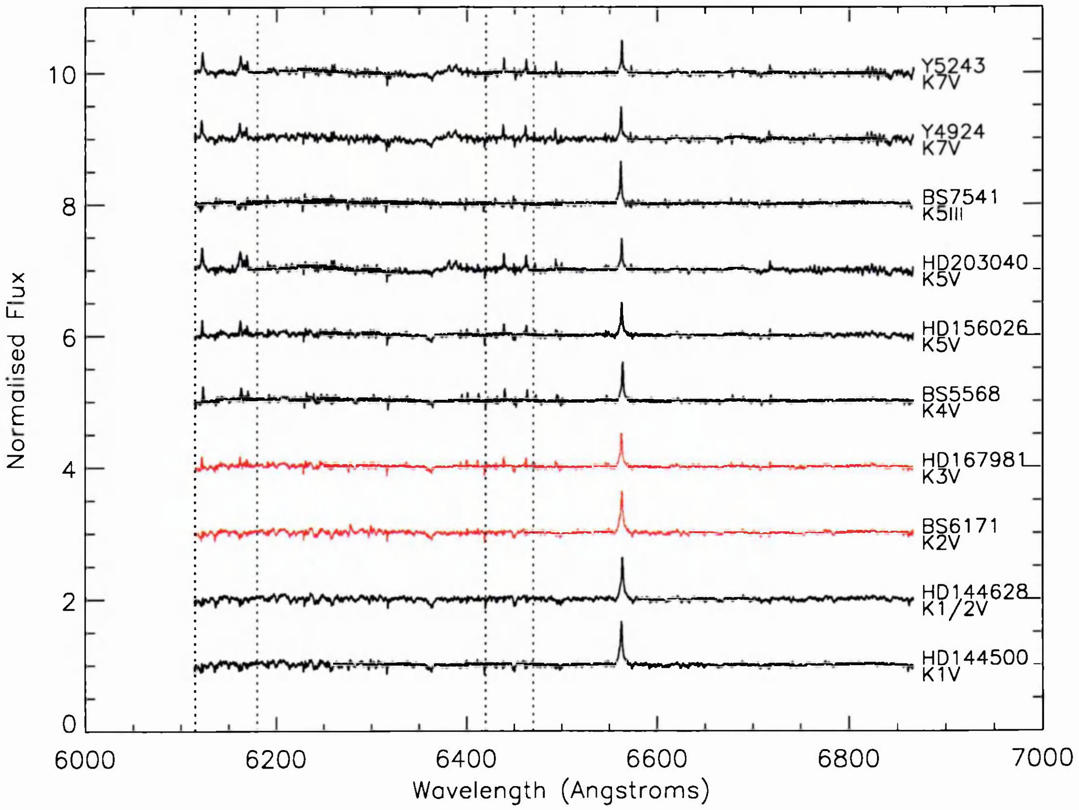

Figure 5.4: First look at the residuals of J1628, from night one of the observations minus K-type templates. The two marked in red demonstrate the point at which the absorption like residuals become emission like, in the wavelength ranges 6115Å to 6180Å and 6420Å to 6470Å (regions between dashed lines).

the line of constant value and hence a large $\chi^2$ value, leading to false identification of the best fitting spectral type from the observations. This $\chi^2$ test identified the K3V spectra as a better fit than the K5III and K2V, but the minimum was found to be for HD144500, K1V. The test in this form, is obviously not suitable to find the best underlying spectrum.

In order to minimise the residuals away from H$\alpha$ the template spectra were simultaneously multiplied by a constant and broadened by convolving with different FWHM Gaussians in an attempt to simulate the underlying spectrum of J1628. Again a $\chi^2$ test was used and the minimum $\chi^2$ for each template, for a range of constants and FWHMs were compared. The result of this are shown in Figure 5.5. The test showed that this method could change the depth of the residual features but cannot remove them entirely. The result of the test showed that the best fit (minimum $\chi^2$)to the spectra of J1628 was that of HD167981 our template K3V, shown in red on the diagram. As we shall see in the next section this can only be taken as an estimate of the spectral type but not of the luminosity class.

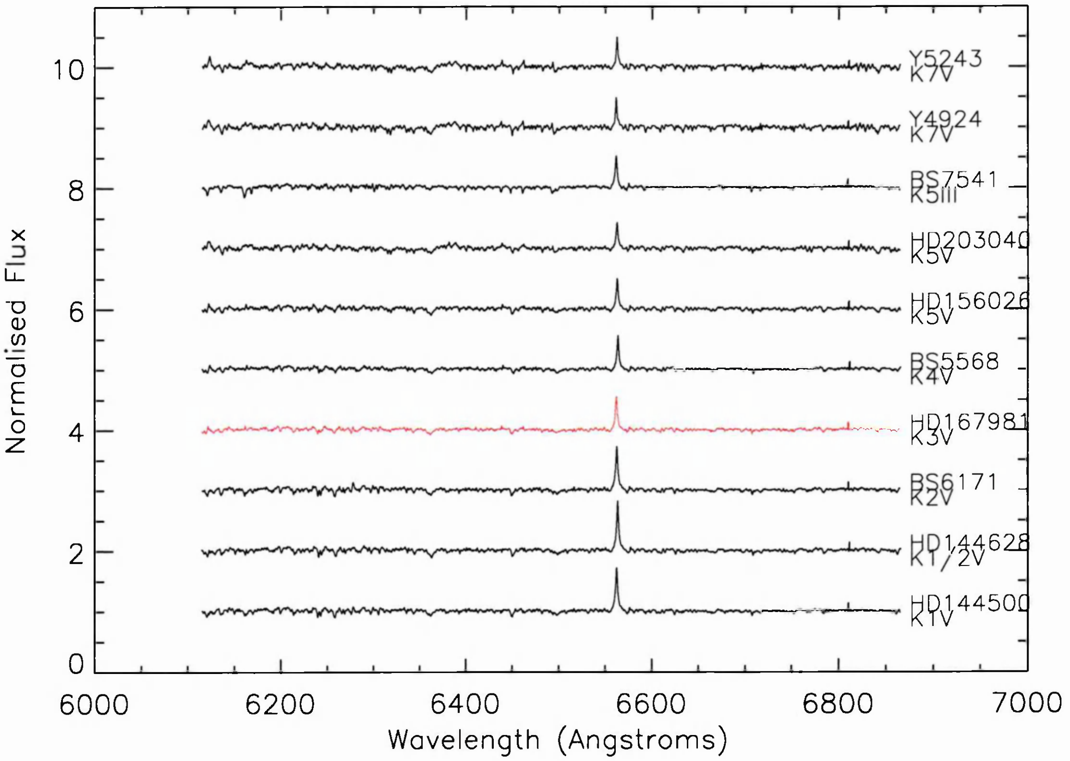

Figure 5.5: Second look at the residuals, the templates have been simultaneously modified with a range of broadening and constant values. The residuals marked in red, for HD167981, show the template which gave the minimum $\chi^2$ in this test, that of a K3V.

### 5.2.4 Giant and Dwarf Comparison

On closer inspection it was found that no giant or dwarf spectrum could be modified, as a whole, to match the spectrum of J1628, since the relative line strengths in the templates were found not to be proportional to the relative line strengths in J1628. The best example of this problem is found in the range 6420Å to 6470Å as shown in Figure 5.6, where three Ca I blends at 6439Å 6449Å and 6462Å cannot be fitted by either dwarf or giant line profiles. It is possible to modify the dwarf or giant spectrum by multiplying by a constant to match the two outer blends or the central blend but not all three blends simultaneously, as demonstrated in Figure 5.7.

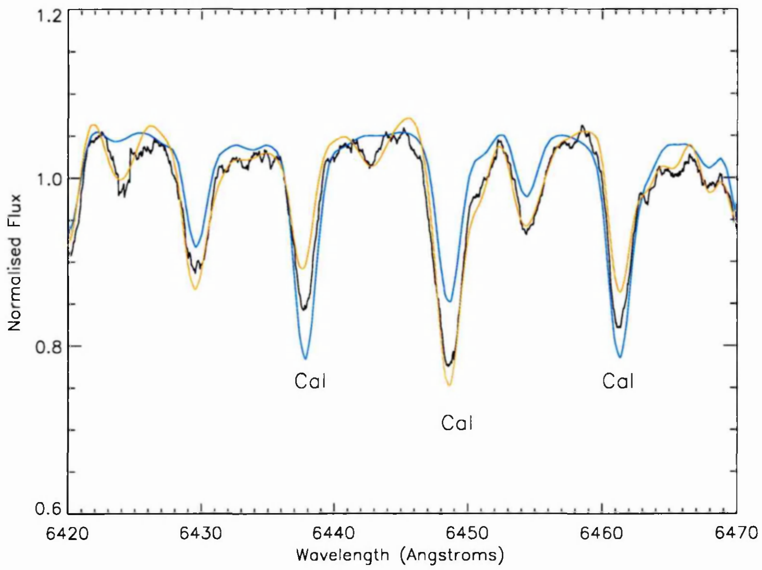

Figure 5.6: J1628 in the range 6420Å to 6470Å (black) with a broadened spectrum of BS7541 (K5III) (orange) and a broadened spectrum of HD156026 (K5V) (blue) overplotted.

Although a K5V star was selected, in the Figures all the dwarfs observed displayed the same relative strength for these three Ca I blends. From this analysis it would appear

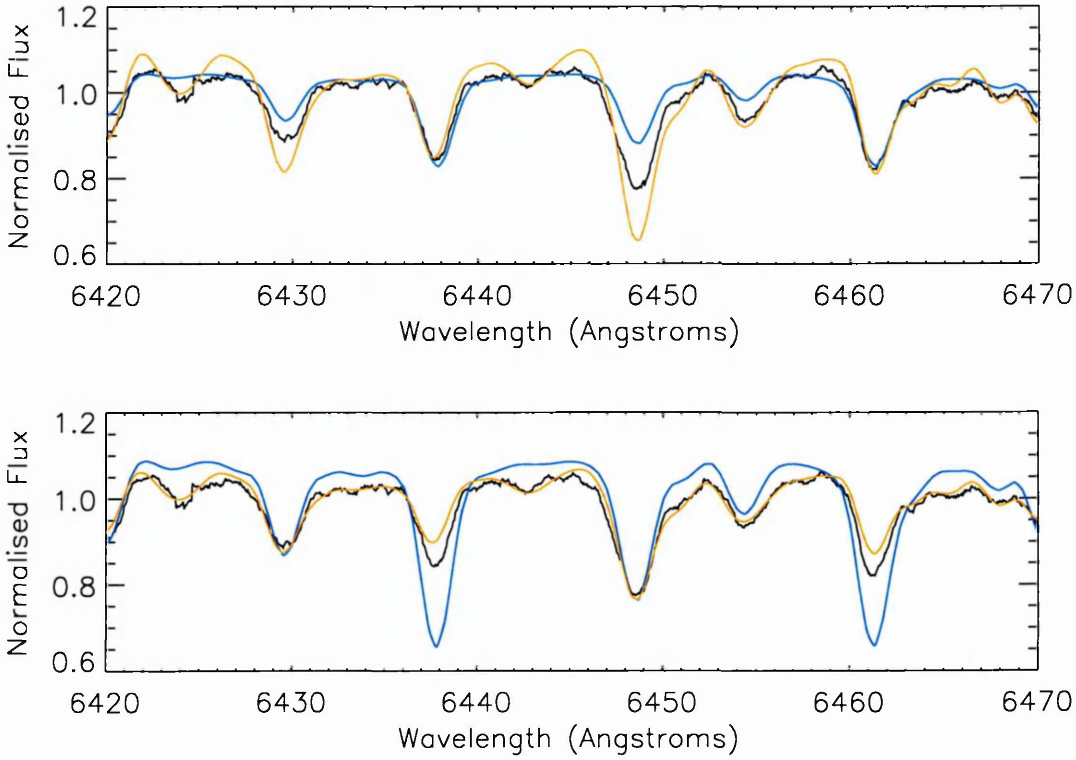

Figure 5.7: J1628 (black) with BS7541 (orange) and HD156026 (blue) overplotted. The top panel shows the fit to the outer two Ca I blends, BS7541 multiplied by a factor of 1.4, HD156026 by a factor of 0.8. The lower panel shows the fit to the central Ca I blend, BS7541 factor=0.2, HD156026 factor=0.95.

that the true luminosity class of J1628 lies somewhere between that of a K-dwarf and a K-giant, therefore J1628 is probably a subgiant K3 star. The subset of spectral type is not obvious from the available data. Another method must be used to identify this parameter, as follows in the next section.

## 5.3 Spectral Synthesis: Identifying 1RXS J 162848.1-415241

Since the spectral features of J1628, primarily the Ca I dominated blends at 6439Å, 6449Å and 6462Å could not be reproduced using our existing template stars, we synthesised K-type spectra for a range of temperatures and surface gravities to first find evidence for an inversion in the Ca I blends as we move from K dwarfs to K giant type stars, and secondly to identify the underlying spectral type and luminosity class of J1628

### 5.3.1 ATLAS: Spectral Synthesis Package

The ATLAS package (Kurucz 1993) calculates the spectrum for a given model atmosphere, generated for the specified effective temperature, surface gravity and metallicity.

The first step to be performed in generating a spectrum for an unknown stellar type is to assemble a linelist for the wavelength range desired and then to edit the gf values for the lines to match the line structure of the known solar spectrum. The gf value for a given line is a dimensionless number which is directly related to the probability of transition between electron levels of an atom or ion. This gives a measure of the absorption or emission strength for a given line. In the case of the solar model atmosphere the parameters are $T_{\rm eff}$ =5770K, surface gravity, $\log(g/{\rm cm\,s^{-2}})$=4.44, and metallicity 0.0 dex since the metallicity scale is defined relative to solar.

The linelist for the range 6100Å to 6900Å was compiled using the gfCAT files from Kurucz and Petremann (1975). These listings are for theoretical gf values and as such the gf values stated are subject to change. We edited the linelist to remove all lines with ionisation potential greater than 5eV, since we are dealing with cool stars. This is an arbitrary value chosen to decrease computing time as any line with value close to or greater than 5eV is thrown out by the ATLAS routine for solar or earlier spectral types.

The theoretical gf values are replaced where possible with measured gf values from the

NIST database (*http : //physics.nist.gov*), but unfortunately the measured values carry large errors in the region of particular interest, 6420Å to 6470Å. This range will be used throughout as it is the site of the three Ca I lines of interest.

With the initial linelist in place, a model solar atmosphere was generated using the grid of model atmospheres from Bell et. al. (1976), and was then used to calculate the synthetic solar spectrum. This synthesised spectrum is then broadened to match observed broadening ( in the case of the comparision solar spectrum this is ~5km/s) and is compared to that observed by Beckers et. al. (1976). Figure 5.8 shows the synthetic solar (red) and the observed solar (black) spectra in the wavelength range of interest (6420Å to 6470Å). We can clearly see that not all the lines in the solar spectrum are reproduced in the synthetic spectrum. This is due to a paucity of line data available in the linelists.

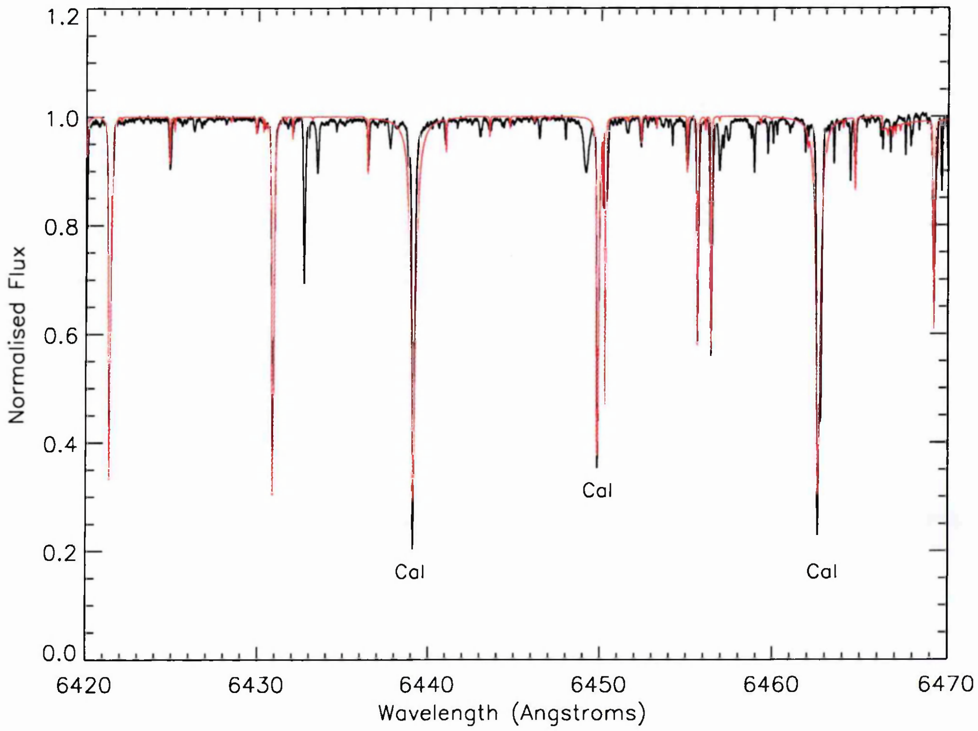

Figure 5.8: Synthesised solar spectrum (red) with Beckers data (black)

The equivalent widths of all lines common to both the observed and synthesised spectrum are measured and the gf values in the linelist modified to recreate the solar equivalent widths as measured from the Beckers spectrum. This is necessary as the ATLAS code arbitrarily broadens the Ca I lines, since this cannot be corrected, the equivalent widths give a direct comparison of the line strengths.

### 5.3.2 Synthesising K-type Spectra

Now that a reasonable fit to the solar spectrum has been achieved, this linelist is used to calculate the spectra of a range of K-type stars. Table 5.3 shows the range of parameters used in this study. The lower end of ranges are the limits of the models available. The upper limits are taken as the model parameters of a K5V star.

Table 5.3: Parameter range for model atmospheres.

| $T_{\rm eff}$ (K) | log (g cms$^{-2}$) | metallicity (dex) |
|---|---|---|
| 3750 - 4557 | 0.0 - 4.65 | -1.8 - 0.0 |

The resulting spectra are broadened to the measured line broadening of J1628 of ~60km/s, this is the FWHM of the gaussian fit to the observed line profiles of J1628. A combination of the instrumental broadening of ~28km/s and the Doppler broadening *v*sini of ~32km/s. Within this parameter space an inversion, by which we mean the central Ca I blend becomes the deepest of the three Ca I blends, is observed for the lower end of the temperature and log g range and for all metallicities in the range. The maximum inversion is seen at the lowest end of the temperature and surface gravity ranges studied, $T_{\rm eff}$=3750, log g=0.0. Figure 5.9 shows the inversions for the full range of metallicities (-1.8 dex to 0.0 dex). Studying the unbroadened spectrum we found that the inversion was due to the presence of Co I and Fe I in the blends. At these low temperature and log g values the Co I dominated blend at approximately 6431Å is far more prominent than at higher values of temperature and log g. The feature at 6449Å is a blend of Ca I , Co I and Fe I and so is greatly enhanced in this low temperature and low log g regime.

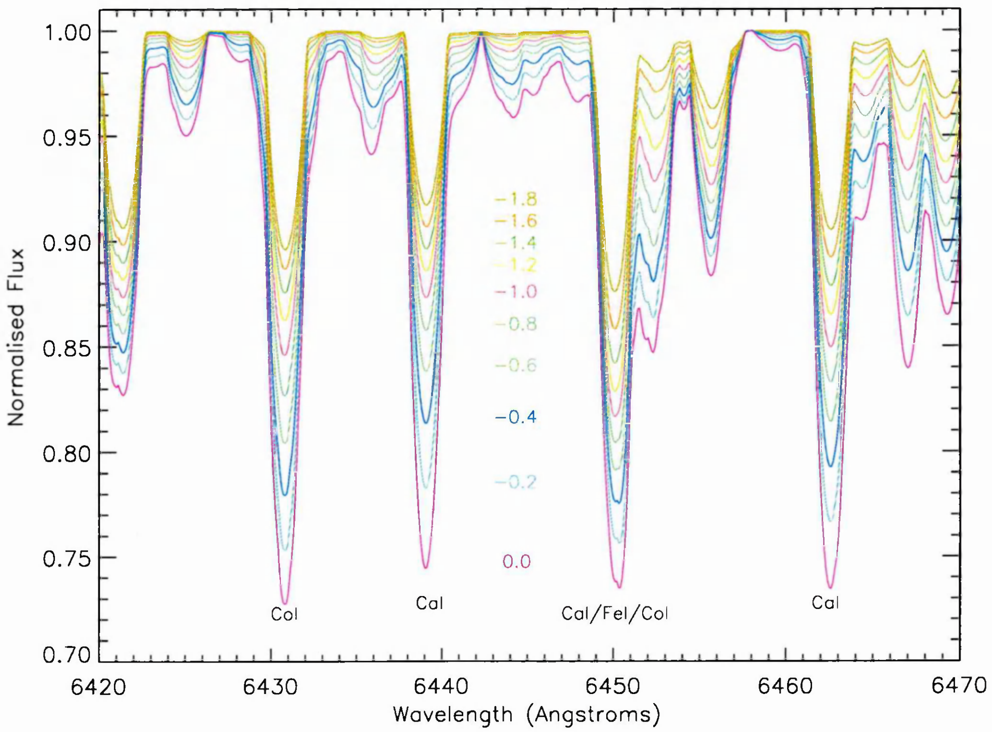

Figure 5.9: Synthetic spectra for $T_{\rm eff}$=3750, log g=0.0 and the full range of metallicities investigated ( in appropriate colour), broadened to match the observed Doppler broadening of J1628, the range 6420Å to 6470Å

Unfortunately, looking at a plot of the synthetic spectra generated with this inversion compared to the spectrum of J1628, Figure 5.10, we find that the inversion in the synthetic data is never as extreme as that seen in the observed spectra. A further consideration is that at the limit of our grid of models we could not recreate the spectrum of a known K5III (BS7541) observed alongside J1628, Figure 5.11, certainly not for the parameters of

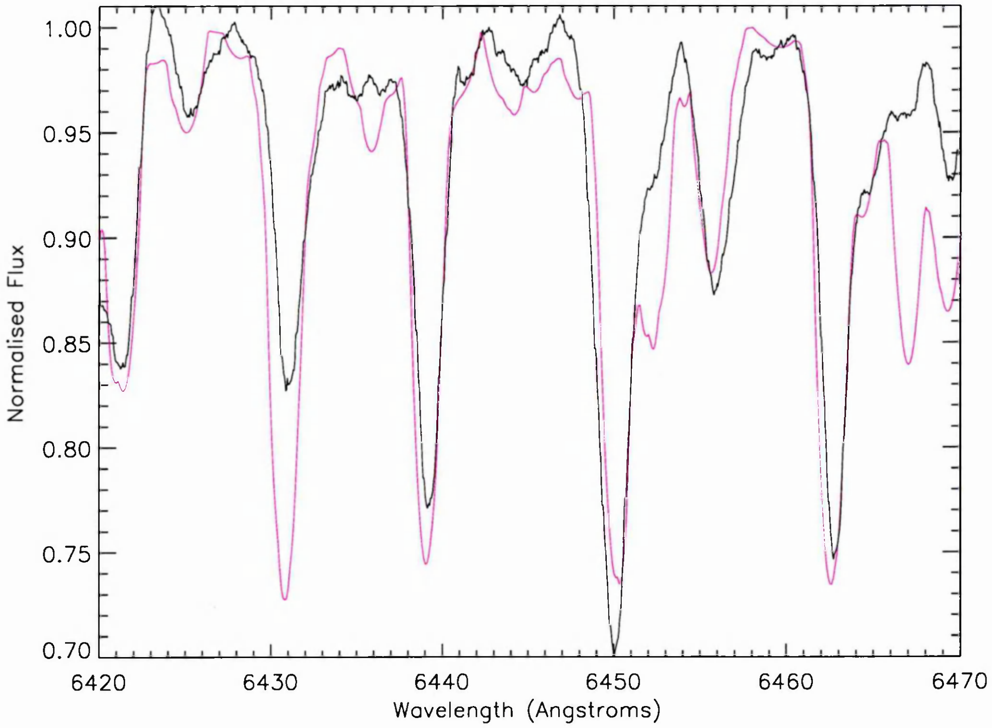

Figure 5.10: Observed J1628 spectrum (black) and synthetic spectrum for $T_{\mathrm{eff}}=3750$, log g=0.0 and a metallicity of 0.0 dex (magenta).

a standard K5III and also not within the low temperature and surface gravity regime.

### 5.3.3 Conclusions from Spectral Synthesis

The only conclusion to be drawn from this process is that as the spectral resolution of our observations is so low, and the extent of the blending of our spectral features is sufficiently high as to give no indication of the actual metal content of our object of study, no abundance analysis could be conducted and hence the metallicity of the object could only be guessed. The grid of parameters available could simulate the inversion of the Ca I blends but could not reproduce the spectrum of our target, or of a standard K5III star. We did find that the inversion is not a property of the Ca I in the blends but resulted from the dominance of the Co I and Fe I on the absorption in the blends at the lower end

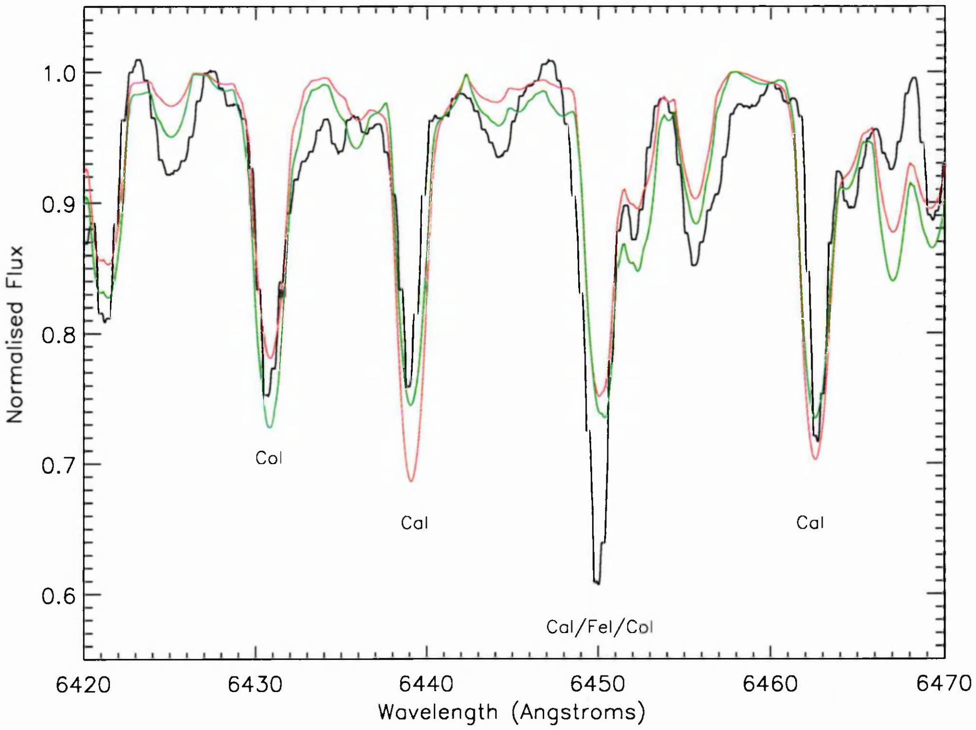

Figure 5.11: BS7541 K5III observed spectrum (black) compared with K5III synthetic spectrum (red) and also $T_{eff}$=3750, log g=0.0 and a metallicity of 0.0 dex spectra (green).

of the parameter ranges. Since the gf values have such high uncertainties associated with them it could be possible to modify these values and so fit the spectrum of J1628 but this would then have no physical relevance as there would be no physical reference point, such as the solar spectrum of Beckers et. al. (1976). The spectral synthesis suggestions that our object may be more evolved than first thought. The lower surface gravity and temperature could indicate an AGB star of K spectral type, though this is not consistent with our measurements of rotation period and velocity. The range of parameters available for this study is a limiting factor. The spectral synthesis does not reveal the luminosity class of J1628. In this case the best estimate would be a direct interpolation between our observed template spectra, Figure 5.6, which gives J1628 a luminosity class between dwarf and giant, a K3 subgiant.

## 5.4 Photometric Observations of 1RXS J 162848.1-415241

Over the period 15th July 2003 to 7th September 2003 photometric observations were made of 1RXS J 162848.1-415241 using the *ROTSE* IIIa robotic telescope sited at Siding Springs Observatory in Australia. The *ROTSE* telescope is a 0.45m robotic, fully automated reflecting telescope, with a field of view of 1.85° × 1.85°, which achieves better than $0.3''$ spatial resolution for most bright (14th magnitude) stars. For the 5 second observations used in this study, the limiting magnitude is 17th, but combined longer exposures can get down as low as 19th magnitude. All observations we used were unfiltered, but the infrastructure is in place to allow filtered observations at a later date (Smith et. al. 2003). The purpose of the photometric observations was to characterise the photometric modulation, if any, of the star 1RXS J 162848.1-415241.

### 5.4.1 Filtering of *ROTSE* data

Although observations were taken on most nights, many frames had to be discarded since the *ROTSE* telescope is automated and took observations even when cloudy, Table 5.4 shows the frames retained and used in the analysis.

Table 5.4: Observation Log of Good Frames from *ROTSE*.

| Date | Number of Exposures | Exposure Time(s) |
|---|---|---|
| 2003 July 15 | 20 | 5 |
| 2003 July 16 | 15 | 5 |
| 2003 July 17 | 20 | 5 |
| 2003 July 19 | 1 | 5 |
| 2003 July 20 | 20 | 5 |
| 2003 July 21 | 5 | 5 |
| 2003 July 22 | 5 | 5 |
| 2003 July 25 | 1 | 5 |
| 2003 July 26 | 15 | 5 |
| 2003 July 27 | 20 | 5 |
| 2003 July 28 | 20 | 5 |
| 2003 July 29 | 15 | 5 |
| 2003 August 1 | 5 | 5 |

Table 5.4: ...continued

| *Date* | *No. exp.* | *Exp. time* |
|---|---|---|
| 2003 August 2 | 5 | 5 |
| 2003 August 3 | 5 | 5 |
| 2003 August 4 | 5 | 5 |
| 2003 August 5 | 15 | 5 |
| 2003 August 17 | 5 | 5 |
| 2003 August 18 | 5 | 5 |
| 2003 August 19 | 5 | 5 |
| 2003 August 26 | 10 | 5 |
| 2003 August 27 | 15 | 5 |
| 2003 August 28 | 10 | 5 |
| 2003 August 29 | 5 | 5 |
| 2003 August 30 | 10 | 5 |
| 2003 August 31 | 10 | 5 |
| 2003 September 5 | 15 | 5 |
| 2003 September 6 | 10 | 5 |
| 2003 September 7 | 15 | 5 |

The data come pre-reduced thanks to the *ROTSE* Data Analysis Pipeline (Smith et. al. 2003.), in that all frames have been flat-field and dark corrected.

### 5.4.2 Analysis of *ROTSE* data set

To improve the signal to noise ratio of the data, the images were combined in sets of five, where they occurred. In IRAF the observation time of the combined images was taken to be that of the third image in each set of five. On two nights only one image was usable and so these images are included individually. Next, two non-variable comparison stars were chosen, with the criteria that they were near the target object on the CCD, to reduce spatial variations across the CCD, and that they were both present in all images. Figure 5.12 shows the target and the two comparison stars.

Since the *ROTSE* observations are unfiltered, magnitude calibration is impossible. The two comparison stars are used to obtain differential magnitudes of 1RXS J 162848.1-415241 relative to each and these data are used to obtain the lightcurve of 1RXS J 162848.1-

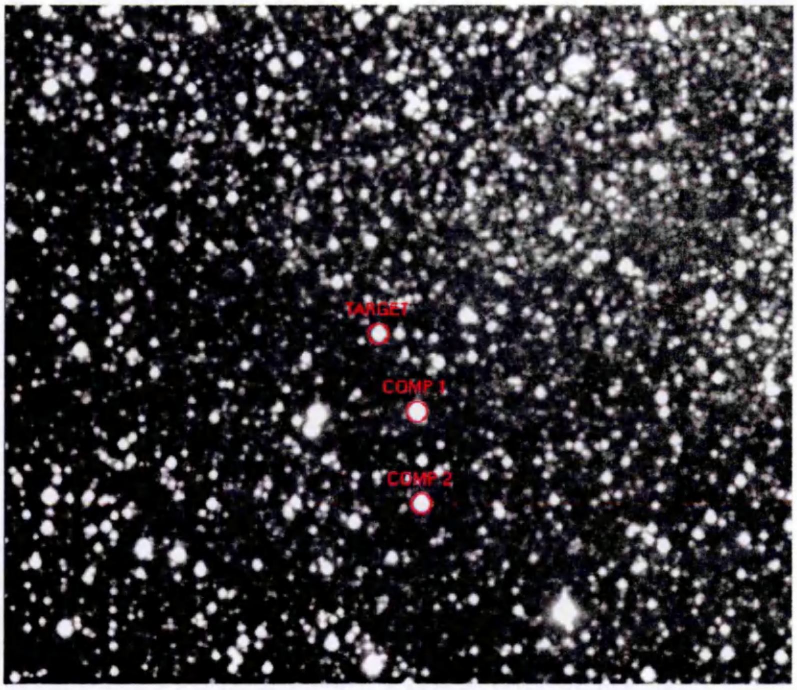

Figure 5.12: *ROTSE* field with 1RXS J 162848.1-415241 and two comparison stars shown. The image is 25″ by 30″ and is orientated North upwards and East to the right.

415241.

### 5.4.3 Photometric Periodicity of 1RXS J 162848.1-415241

The lightcurve of 1RXS J 162848.1-415241 shows a clear periodic variation. To derive the period the STARLINK software PERIOD was used, using a reduced $\chi^2$ against frequency method, the resulting period was found to be 5.0±0.11 days derived from the minimum $\chi^2$ peak in the periodogram. Figure 5.13 shows the reduced $\chi^2$ against frequency distribution and Figure 5.14 shows the fit to the data.

## 5.5 Conclusions

If this object was a microquasar we could expect to see ellipsoidal modulation in the lightcurve, that is two maxima and two minima over one orbital period. This arises from

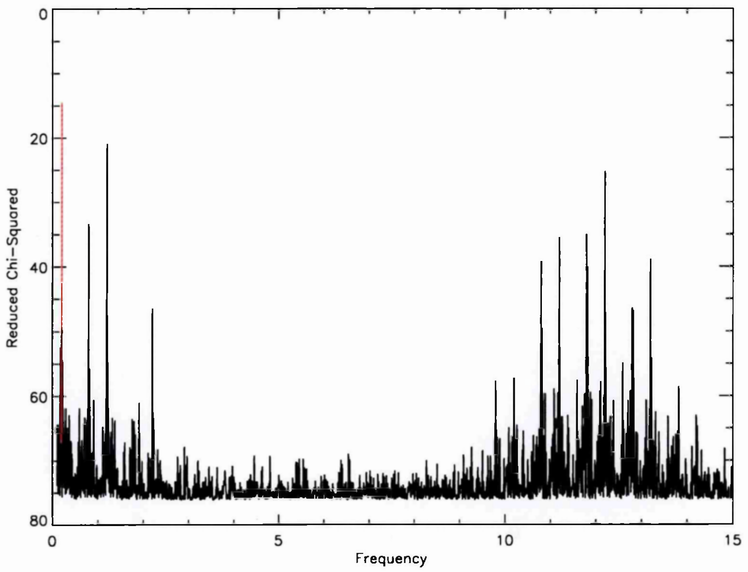

Figure 5.13: Reduced $\chi^2$ against frequency distribution for *ROTSE* photometry, the minimum $\chi^2$ peak is shown in red.

the donor star filling its Roche lobe causing it to become elongated. As the elongated star travels around its orbit the elongated face with its larger cross-section causes a maximum,

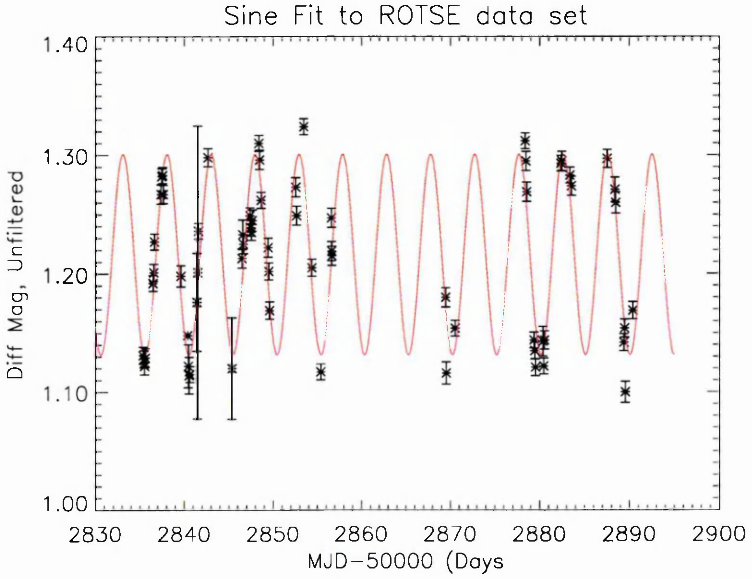

Figure 5.14: Sinusoidal fit to *ROTSE* data set.

then as the truncated face moves through the observers line of sight we see a minimum, the elongated and truncated faces are seen twice (both sides of the star) per orbit and so we get two maxima and two minima. The photometric period, derived in section 5.4.3, of 5.00±0.11 days is directly comparable to the derived orbital period of 4.869±0.007 days from radial velocity measurements, Section 5.2.1. The absence of ellipsoidal variation in the photometric lightcurve suggests this is not a microquasar or other semi-detached binary, but J1628 does appear to be tidally locked since its photometric and orbital periods are the same within the $2\sigma$ errors. This leads to the question, what is causing the photometric modulation? The best answer is that there is a star spot on the surface of J1628. These star spots are caused by emerging magnetic flux suppressing the convective heating of the photosphere in that region, cooling the region and making it appear darker than the surrounding surface. A large spot could be causing the periodic dip in brightness, we observe, as it moves across our line of sight. The consistent photometric period is also an indicator that the star is tidally locked, to get the periodic modulation seen in the lightcurve the dark spot must be in the same place on the star in each orbit meaning that the rotation period of the J1628 is the same as the orbital period.

Physical limits can be placed on the radius of J1628 simply by considering the rotational velocity and period of the star. For any rotating body,

$$v_{rot} = \omega R_2 \tag{5.2}$$

where $v_{rot}$ is the rotational velocity, $\omega$ is the angular velocity and $R_2$ is the radius of our object. The subscript $R_2$ is used to denote that our star is the secondary in the binary. This will become clear later. Additionally,

$$\omega = \frac{2\pi}{P_{rot}} \tag{5.3}$$

where $P_{rot}$ is the period of rotation. Since we do not know at what inclination we are observing the system we do not know $v_{rot}$ exactly. What we do know is $v_{rot}$sini where $i$ is the angle subtended between the axis of rotation and our line-of-sight. Hence $v_{rot}\text{sini} \leqslant \mathrm{v_{rot}}$ Combining equations 5.2 and 5.3 with our inequality we arrive at:

$$R_2 \geqslant \frac{P_{rot} v_{rot} \text{sini}}{2\pi}. \tag{5.4}$$

For our observed values, $v\text{sini} = 32 \pm 21\text{kms}^{-1}$ and $P_{rot} = 5.00 \pm 0.11$ days we obtain a lower limit of $R_2 \geqslant 3.2 \pm 2.2 R_{\odot}$. We can calculate an upper limit to our stellar radius if we assume that J1628 is a subgiant K3 star. From Carroll and Ostlie (1996) and Lanza (2005) we have the mass of these objects lying in the range 1.1-1.3$\mathrm{M}_{\odot}$. Taking an estimate for the mass, $M_2$, for J1628 to be 1.2$\mathrm{M}_{\odot}$ and using the assumption that the material on the surface is just gravitationally bound, such that rotational and gravitational forces are balanced, we can proceed as follows:

$$\omega^2 R_2 \leqslant \frac{G M_2}{R_2^2}. \tag{5.5}$$

Rearranging and substituting equation 5.3 we arrive at,

$$R_2 \leqslant (G M_2)^{\frac{1}{3}} \left( \frac{P_{rot}}{2\pi} \right)^{\frac{2}{3}}, \tag{5.6}$$

and hence $R_2 \leqslant 13.0 \pm 0.3 R_{\odot}$. We now have constraints for the radius of J1628, $3.2 \pm 2.2 R_{\odot} \leqslant R_2 \leqslant 13.0 \pm 0.3 R_{\odot}$. Using the empirical relationship for giants from van Belle et. al. (1999) we calculate that the radius of a K3III is $22.6 R_{\odot}$. The constraints on J1628 place it at a lower radius than this and so we can safely assume that J1628 is not a giant but a subgiant. Most K-type subgiants have radii in the range 3.0-4.0$R_{\odot}$ (Lanza 2005) which is at the lower limit of our inequality but is well within the errors. This suggest sini is fairly close to 1.

With this information we can move on to looking at the system as a whole starting with a limit on the orbital separation of the binary. From Kepler's third law,

$$P_{orb}^2 = \frac{4\pi^2 a^3}{G(M_1 + M_2)} \tag{5.7}$$

where $a$ is the orbital separation of the binary. We can substitute the mass ratio of the binary $q = \frac{M_2}{M_1} = \frac{K_1}{K_2}$ for our unknown mass $M_1$; $K_1$ and $K_2$ are the velocity semi amplitudes of the orbital periods for the primary and J1628 respectively. Rearranging for $a$,

$$a = \left(1 + \frac{1}{q}\right)^{\frac{1}{3}} \left[\frac{P_{orb}^2 G M_2}{4\pi^2}\right]^{\frac{1}{3}} \tag{5.8}$$

putting in the values that we already have, we get:

$$a = (13.2 \pm 0.04)\left(1 + \frac{1}{q}\right)^{\frac{1}{3}} R_{\odot} \tag{5.9}$$

since $q$ must always be positive, the second term in brackets can never be less than one so $a \geqslant (13.2 \pm 0.04)R_{\odot}$. We can constrain $q$ if we assume that $R_2 \leqslant R_{2rl}$ where $R_{2rl}$ is the radius of J1628's Roche lobe i.e. J1628 does not overfill its Roche lobe. For a Roche lobe filling star we can combine the equations from Wade et. al. (1988),

$$v_{rot}\mathrm{sini} = (\mathrm{K}_1 + \mathrm{K}_2)\frac{\mathrm{R}_2}{\mathrm{a}} \tag{5.10}$$

and Eggleton 1983,

$$R_{2rl} = \left[\frac{0.49q^{\frac{2}{3}}}{0.6q^{\frac{2}{3}} + ln(1 + q^{\frac{1}{3}})}\right] \tag{5.11}$$

for an orbital separation of unity, to get,

$$\frac{v_{rot}sini}{K_2} \leqslant (1 + q)\left[\frac{0.49q^{\frac{2}{3}}}{0.6q^{\frac{2}{3}} + ln(1 + q^{\frac{1}{3}})}\right] \tag{5.12}$$

An IDL script was written to evaluate the right hand side of equation 5.12 and for $v\mathrm{sini} = 33 \pm 21\mathrm{kms}^{-1}$ and $K_2 = 33.4 \pm 0.1\mathrm{kms}^{-1}$ we find that the inequality is satisfied for $q \geqslant 1.5 \pm 1.0$. Using the limit of $q \geqslant 2.5$ and equation 5.9 we arrive at an upper limit for $a$ of $14.8R_{\odot}$ Given that $q \geqslant 2.5$ and $M_2 = 1.2M_{\odot}$ the mass of the primary object must be in the range $M_1 \geqslant 0.48M_{\odot}$. We can also use our minimum value for $q$ in equation 5.11 to derive a lower limit on the size of the Roche lobe: $R_{2rl} \geqslant 4.23 \pm 0.01R_{\odot}$. Since no evidence is found for our object filling its Roche lobe we can state that the radius of J1628 is $3.2 \pm 2.2R_{\odot} \leqslant R_2 \leqslant 4.23 \pm 0.01R_{\odot}$, further refining the range of our radius and placing J1628 firmly in the subgiant class. Lanza (2005) gives a range of subgiant luminosities of 4-8$L_{\odot}$. Taking the lower limit of this range and comparing to the data on spectral types in Carroll and Ostlie (1996), with the assumption that the primary has to be fainter than J1628 (since no evidence is seen for it in the data), the most likely candidate for the primary would be a dwarf of spectral type later than F0. Another possibility that cannot be ruled out is that the primary is a compact object either a white dwarf, neutron star, or black hole. Since the binary is detatched, and J1628 is not filling its Roche lobe no mass transfer takes place, so we would see no signature of an accretion disk.

Using the above parameters and arguments we can say the following J1628 is most likely a K3IV chromospherically active star in a detached binary system, with orbital separation $(13.2 \pm 0.04)R_{\odot} \leqslant a \leqslant 14.8R_{\odot}$ and a primary star more massive than an M1V but with spectral type later than F0/1V, or a stellar remnant. Since we have an K3 subgiant star with concurrent orbital and photometric periods and evidence of chromospheric activity with H$\alpha$ emission, the most likely candidate system is an RS CVn star. Hall 1979 defined the RS CVn class of systems as having,

- orbital periods 1-14 days,
- evidence of chromospheric activity, filled cores in Ca II H and K lines, H$\alpha$ in emission,
- distortion of the lightcurve outside of eclipse by 0.1-0.3 magnitudes.

These systems were further characterised by Fekel (1986),

- the more active star must be F, G, or K type, and evolved.

Our system fits very neatly into this classification, even the modulation of the lightcurve is of the order 0.1 magnitudes. If this is the case we can increase the number of known RS CVn stars from 173 (taken from a search of SIMBAD) to 174.

# Chapter 6

# Conclusions

In the preceding chapters we have presented four case studies each with one thing in common. In each case magnetic activity was responsible for the events that drew them to our attention, flaring events on the Sun (2) and flare stars (4.1 and 4.2) and the radio and X-ray behaviour of our RS CVn system and the starspots that revealed its true nature (5). The flaring events studied on the Sun allowed us to probe the acceleration of an initial population of electrons and test our current understanding of the interaction of these electrons with the surrounding medium. We found that the observations did not result in unphysical electron distributions and so our current theories on the nature of the interaction cross sections holds up to new observations and provides a solid basis to launch our further understanding of flare physics.

Serendipitous observations of flare like events on other stars, in both the X-ray and the optical, revealed primarily mid M-type dwarf stars as we would expect from our current understanding of which types of star produce these stellar flares.

A comparison of J004236.5+411350's X-ray flare luminosity to that of some of the largest flares ever observed on the Sun shows that the two flares observed are approximately one hundred times more intense. This is not surprising since stellar flares consistently show larger EMs for a given plasma temperature than for solar flares, Figure 4.5. The discussion in Section 4.1.7, and references therein, shows that the EM is the dominant factor for increased flare luminosity. Since the EM is proportional to the electron density and the volume of the flaring plasma, measurements of the ratios of density sensitive coronal lines on other flare stars can be used to estimate the flaring volume on J004236.5+411350. The values obtained in the literature show that the electron density is higher in flare stars than in solar flares. Using this result we found that for the flares observed on J004236.5+411350 the flaring volume was a factor of $10^4$ larger than for flares on the Sun. This suggests that a large proportion of the stellar surface could be involved in these events, possibly whole star flaring, through a phenomenon known as sympathetic flaring where the triggering of one flare triggers others. This phenomenon could also help to explain the much longer timescales we observe in stellar flaring, as it takes place over a larger area than the very localised solar flares, and the impulsive phase of these flares is longer due to the flare propagating across the surface of the star. The decay phase of the event is also extended as the star returns to quiescence.

The optical flaring we have observed during the WAVS survey also occurs over longer timescales than for a typical solar flare. Two of the objects observed are typical of the flare star population. Both display the classical M-dwarf spectral features of prominent molecular absorption bands, and in one case definite H$\alpha$ in emission, indicative of chromospheric activity. The third object was something of an enigma, the lightcurve profile resembles that of a flare, and there was no evidence of broad absorption bands in the spectra, ruling out an M-dwarf. Two possibilities were put forward. It could be that we were observing the optical counterpart of a type I X-ray burst, the first identified through optical data, or that it was a star of earlier spectral type than M exhibiting flaring. The case put forward for this object being the optical component of a type I X-ray burst, was all but ruled out through a comparison to the literature on optical observations of these events and from the distance calculation performed in Section 4.2.4. Earlier types do show flaring, but it is far harder to observe due to the relative brightness of the underlying stellar photosphere. Fitting the observed spectrum with standard F-K type spectra revealed that the object was a K4V approximately 5kpc distant.

The final case study presented for consideration an object which could generate a great deal of excitement. If a microquasar it would be the brightest known to date and would allow us to probe further into the nature of these powerful objects. The observations presented showed no evidence for a Roche lobe filling star or for an accretion disk. In trying to identify the object, J1628, we found, a K3 star within a binary but no evidence in our observations for the nature of the second object. In trying to identify the exact nature of the K-star we found that it did not match any of our templates to the extent at which we could positively identify it, but it did allow us to propose an evolutionary state from the 'inversion' of the triple Ca I blend of a K3 subgiant star. The identification of this inversion could lead to a new method for quickly classifying the evolutionary states of K-stars in future observations, and if time allowed would be worth pursuing. Only the lack of available data, at a high enough spectral resolution, prevents this from being fully investigated. Although the object was found not to be a microquasar, we could still identify the nature of the system from the data we had collected. All the data point to the system containing an evolved K3IV star with a modulated lightcurve. The explanation for the modulation is that some part of the surface is less bright than the rest, since there is no evidence for eclipsing, this could only be the result of spotting on the stars photosphere, caused by the emergence of magnetic flux on the surface of the star. The orbital period derived from the radial velocity of the star is in direct agreement, within $2\sigma$, with the photometric period derived from the modulation in the lightcurve. Since we detect the starspot(s) at the same phase in the orbital cycle it is not unreasonable to consider this object to be tidally locked within the binary. Using this assumption we were able to constrain system parameters for the binary (see Section 5.5). We found that the K3IV secondary had a radius $3.2 \pm 2.2 R_\odot \leqslant R_2 \leqslant 4.23 \pm 0.01 R_\odot$, the orbital separation of the two components of the binary was $(13.2 \pm 0.04) R_\odot \leqslant a \leqslant 14.8 R_\odot$, the mass ration of the system $q \geqslant 1.5 \pm 1.0$. Using these parameters we found that the mass of the primary object $M_1 \geqslant 0.48 M_\odot$. Adding the constraint that the primary object had to be less luminous than a K3IV, lead to the conclusion that the primary object had to be either a main sequence dwarf star of spectral type F0/1V or later, or the object could be a compact object either a white dwarf, neutron star, or black hole. Since the binary is detached, and J1628 is not filling its Roche lobe no mass transfer takes place and so the primary would not be accreting. We set out looking for a system in which magnetic fields play a prominent role and although of a different class, RS CVn, we found one.

We have seen evidence for magnetically driven events across a range of astronomical systems. In each case they are the driving force behind that system's classification and are usually the trigger for an event or feature on the object that first bring it to our attention, or allows us to identify the object's nature. Magnetic fields drive some of the most energetic, recurring events in our Galaxy. Without the interplay between the astrophysical plasmas and the stellar magnetic field we would live in a far duller universe.

# References

Agrawal, P.C., Rao, A.R., Sreekantan, B.V., 1986, MNRAS, 219, 225-239

Alexander, R.C., and Brown, J.C., 2002, Solar Physics, 210, 407-418

Barnard, R., Osborne, J.P., Kolb, U., and Borozdin, K.N., 2003, A&A, 405, 505-511

Beckers, J.M., Eriksson, R., Gustafsson, B., and Nordlund, Å, 1976, A&AS, 23, 37

Bell, R.A.., Bridges, C.M., and Gilliam, L.B. 1976, *A High Resolution Spectral Atlas of the Solar Irradiance from 380 - 700nm*, Volume 1 Tabular Form (US Air Force Geophysics Lab, Massachusetts)

Bell, R.A., 1983, priv. comm.

Brown, J.C., 1971, Solar Physics, 18, 489

Carroll, B.W., Ostlie, D.A. 1996, An Introduction to Modern Astrophysics

Carrington, R.C., 1859, MNRAS, 20, 13-15, Description of a Singular Appearance seen in the Sun on September 1, 1859

Chaty, S., Haswell, C.A., Malzac, J., Hynes, R.I., Shrader, C.R., and Cui, W., 2003, MNRAS, 346, 689-703

Conway, A. J., 2000, http://hesperia.gsfc.nasa.gov/rhessidatacenter/imaging/memvis.html

Conway, A.J., Brown, J.C., Eves, B.A.C., and Kontar, E., 2003, A&A, 407, 725-734

Conway, A.J., Kontar, E., Schwarz, R,A, 2002, priv. comm.

Cranell, C. J., and Frost, K. J., and Saba, J. L., and Maetzler, C. and Ohki, K., 1978, ApJ, 223, 620C

Dorman, B. and Arnaud, K.A., 2001, ASP Conf. Ser. 238, 415

Durney, B.R., De Young, D.S., Roxburgh, I.W., 1993, Solar Physics, 145, 207-225

Eggleton, P.P., 1983, ApJ, 268, 368

Feldman, U., Laming, J.M., and Doschek, G.A., 1995, ApJL, 451, 79

Fekel, F.C., Moffett, T.J., and Henry, G.W., 1986, ApJS, 60, 551-576

Forbes, T.G., Malherbe, J.M., and Priest, E.R., 1989, Solar Physics, 120, 285-307

Fuhrmeister, B., and Schmitt, J.H.M.M., 2003, A&A, 403, 247-260

García-Alvarez, D., Jevremović, D., Doyle, J.G., and Butler, C.J., 2002, A&A, 383, 548-557

Giampapa, M., 2000, to appear in, Murdin, P., Encyclopedia of Astronomy and Astrophysics, 2005 IOP Publishing LTD

Giampapa, M.S., Rosner, R., Kashyap, V., Fleming, T.A., Schmitt, J.H.M.M., and Bookbinder, J.A., 1996, ApJ, 463, 707

Güdel, M., 2004, A&AR, 12, 71-237

Haiman, Z., Magnier, E., Lewin, W.H.G., Lester, R.R., van Paradijs, J., Hasinger, G., Pietsch, W., Supper, R., Truemper, J., 1994, A&A, 286, 725-732

Hall, D.S., 1976, ASSL Vol. 60: IAU Colloq. 29: Multiple Periodic Variable Stars, 287

Haswell, C.A. and Tajima, T., 1987, BAAA, 19, 1034

Horne, K., 1986, PASP, 98, 609-617

Hurford, G.J., Schmahl, E.J., Schwartz, R.A., Conway, A.J., Aschwanden, M.J., Csillaghy, A., Dennis, B.R., Johns-Krull, C., Krucker, S., Lin, R.P., McTiernan, J., Metcalf, T.R., Sato, J., Smith, D.M., 2002, Solar Physics, 210, 61-86

Hynes, R.I., Haswell, C.A., Cui, W., Shrader, C.R., O'Brien, K., Chaty, S., Skillman, D.R., Patterson, J., and Horne, K., 2003, MNRAS, 345, 292-310

James, D.J., Jardine, M.M., Jeffries, R.D., Randich, S., Collier Cameron, A., and Ferreira, M., 2000, MNRAS, 318, 1217-1226

Johnson, H.L., 1966, ARA&A, 4, 193-206

Kane, S.R., and Anderson, K.A., 1970, ApJ, 162, 1003

Kong, A.K.H., Garcia, M.R., Primini, F.A., Murray, S.S.,Di Stefano, R., McClintock, J.E.

2002, ApJ, 577, 738-756

Kong, A.K.H., Homer, L., Kuulkers, E., Charles, P.A., and Smale, A.P., 2000, MNRAS, 311, 405-413

Kontar, E.P., Brown, J.C., Emslie, A.G., Schwartz, R.A., Smith, D.M., and Alexander, R.C., 2003, ApJ, 595, L123-L126

Kurucz, R.L., 1993, CD-ROM 13, *ATLAS9 Stellar Atmospheres Programs and 2km/s grid*

Kurucz, R.L., Peytremann, E., 1976, SAO Special Report 362 (Smithsonian Institution, Cambridge)

Lamb, D.Q., 2000, ApJS, 127, 395-408

Lanza, A.F., 2005, MNRAS, 364, 238-246

Lin, R.P. and Schwartz, R.A., 1987,ApJ, 312, 462-474

Lin, R.P., Dennis, B.R., Hurford, G.J., Smith, D.M., and 62 co-authors, 2002, Solar Physics, 210, 3-32

Lott, D.A., Haswell, C.A., Abbott, T.M.C., and Ringwald, F., 2002, ASP Conf. Ser. 261: The Physics of Cataclysmic Variables and Related Objects, 289

Lott, D.A., 2004, Thesis

Magnier E.A., Battinelli P., Lewin W.H.G., Haiman Z., Van Paradijs J., Hasinger G., Pietsch W., Supper R., Trumper J., 1993, A&A, 278, 36-42

Massone, A.M., Piana, M., Conway, A., Eves, B., 2003, A&A, 405, 325-330

Masuda, S., Kosugi, T., Hara, H., Tsuneta, S., and Ogawara, Y., 1994, Nature, 371, 495

Maxwell, D., 2001, Thesis

McClure, R., Racine, R., 1969, ApJ, 74, 1000-1007

Morrison, R. and McCammon, D., 1983, ApJ, 270, 119-122

Ness, J.-U., Audard, M., Schmitt, J.H.M.M., and Güdel, M., 2003, Advances in Space Research, 32, 937-943

Petschek, H.E., 1964, The Physics of Solar Flares, PSF Conf. Proceedings, 425

Pettersen, B.R., 1989, Solar Physics, 121, 299-312

Pickles, A.J., 1998, A Stellar Spectral Flux Library: 1150 - 25000 Å, VizieR Online Data Catalog, 611, 863

Predehl, P., Schmitt, J.H.M.M., 1995, A&A, 293, 889-905

Raassen, A.J.J., Mewe, R., Audard, M., Güdel, M., 2003, A&A, 411, 509-515

Robrade, J. and Schmitt, J.H.M.M., 2005, A&A, 435, 1073-1085

Saint-Hilaire, P. and Benz, A.O., 2005, A&A, 435, 743-752

Schmitt, J.H.M.M., 1994, ApJS, 90, 735-742

Schnopper, H.W., Thompson, R.I., and Watt, S., 1968, Space Science Reviews, 8, 534

Silverman, J.D.,Eriksen, K.A., Green, P.J., and Saar, S.H., 2001, MNRAS, 323,577-583

Smith, D., Akerlof, C., Ashley, M.C.B., Casperson, D., Gisler, G., Kehoe, R., Marshall, S., McGowan, K., McKay, T., Phillips, M.A., Rykoff, E., Vestrand, W.T., Wozniak, P., Wren, J., 2003, AIP Conf. Proc. 662: Gamma-Ray Burst and Afterglow Astronomy 2001: A Workshop Celebrating the First Year of the HETE Mission, 514-516

Supper, R., Hasinger, G., Pietsch, W., Trümper, J., Jain, A., Magnier, E.A., Lewin, W.H.G., van Paradijs, J., 1997, A&A, 317, 328-349

Supper, R., Hasinger, G., Lewin, W.H.G., Magnier, E.A., van Paradijs, J., Pietsch, W., Read, A.M., Trümper, J., 2001 A&A, 373, 63-99

Tonry, J., and Davis, M., 1979, AJ, 84, 1511-1525

Tsarevsky, G.S., Kardashev, N.S., Stathakis, R.A., Slee, O.B., and Ojha, R., 2001, ATEL #80

Tsarevsky, G.S., Pavlenko, E.P., Stathakis, R.A., Kardashev, N.S., and Slee, O.B., 2002, ASP Conf. Ser. 261: The Physics of Cataclysmic Variables and Related Objects, 301

Tsikoudi, V., Kellett, B.J., Schmitt, J.H.M.M., 2000, MNRAS, 319, 1136-1146 van Belle, G.T., Lane, B.F., Thompson, R.R., Boden, A.F., Colavita, M.M., Dumont, P.J., Mobley, D.W., Palmer, D., Shao, M., Vasisht, G.X., Wallace, J.K., Creech-Eakman, M.J., Koresko, C.D., Kulkarni, S.R., Pan, X.P., Gubler, J., 1999, AJ, 117, 521-533

van den Besselaar, E.J.M., Raassen, A.J.J., Mewe, R., van der Meer, R.L.J., Güdel, M., Audard, M., 2003, A&A, 411, 587-593

Wade, R.A. and Horne, K., 1988, ApJ, 324, 411-430

Wegner, W., 1994, MNRAS, 270, 229-234

Wu, K., Stevens, J.A., and Hannikainen, D.C., 2002, PASA, 19, 91-99